Modeling Hydrodynamic Instabilities, Shocks, and Radiation Waves in High Energy Density Experiments

by

Shane Coffing

A dissertation submitted in partial fulfillment
of the requirements for the degree of
Doctor of Philosophy
(Applied Physics)
in the University of Michigan
2023

Doctoral Committee:

Associate Professor Carolyn Kuranz, Co-Chair
Dr. Chris L. Fryer, Los Alamos National Laboratory, Co-Chair
Professor Emeritus R. Paul Drake
Assistant Professor Eric Johnsen

Shane X. Coffing

shanex@umich.edu

ORCID iD: 0000-0002-7083-3038

ACKNOWLEDGMENTS

First, I thank my family: my mother, who along with birthing me and thereby making this research possible has been a source of unending love; my father, who simultaneously drove me academically to prioritize my degree but also taught me the importance of play; and my Aunt Tracy, Uncle Jimmy, and all my stubborn cousins, who kept my head from going too far into the clouds.

Second, I thank my friends for providing a significant majority of the seemingly small life part of my work-life balance. I kinda owe you a lot.

Third, I thank my mentors Carolyn Kuranz, Paul Drake, and Chris Fryer, for truly outstanding mentorship, belief in my ability, and a real chance when, as likely many graduate students feel, it was so difficult to feel as though I deserved it.

Finally, I thank my committee, who not only provided the education I needed to complete this thesis, but actually, presumably read it.

TABLE OF CONTENTS

LIST OF FIGURES

LIST OF TABLES

LIST OF ABBREVIATIONS

HEDP high-energy density physics

LANL Los Alamos National Laboratory

KHI Kelvin-Helmholtz instability

HEDLA high-energy density laboratory astrophysics

ICF inertial confinement fusion

LTE local thermodynamic equillibrium

UQ uncertainty quantification

EOS equation of state

PDEs partial differential equations

CFL Courant-Friedrichs-Lewy

RTI Rayleigh-Taylor instability

RTE radiative transfer equation

CCD coupled-charge device

AGN active galactic nuclei

CGM hot circumgalactic medium

SPH Smooth-Particle-Hydrodynamics

MFP mean free path

NIF National Ignition Facility

LEH laser entrance hole

REH rear exit hole

IMC implicit Monte Carlo

3T three temperature

nLTE non-local thermal equillibrium

LRM linear response method

MCP micro-channel plate

ABSTRACT

This thesis presents the computational design, modeling, and analysis of three experiments in high-energy density physics (HEDP), all of them concerning fundamental radiation flows. The first experiment is a laboratory astrophysics experiment to investigate the role of the Kelvin-Helmholtz instability (KHI) in the process of galactic filaments supplying gas to galactic halos. The achieved goal was to provide a first study in which the role of the instability is maximal and predict behavior in future iterations of an experiment accessing a more radiative regime where the role of the instability is stifled. This experiment would help answer how certain galaxies are able to grow so rapidly and produce many stars as the KHI limits this process.

The second experiment, COAX, is a radiation flow experiment with a novel spectroscopy diagnostic configuration, designed to spatially measure the temperature of a radiation wave as it travels down a doped foam. A key result of this work was the development of a synthetic spectroscopy application and application of modern spectroscopy comparison techniques to provide our first temperature reconstructions from the experimental data. This experimental platform serves as the launching ground for a number of new experiments that vary the basic premise and thus is foundational to our ongoing research.

The final experiment is a full integration of modeling, design, and theoretical development for the Radishock experiment. This experimental platform studies the head-on collision of a radiation wave with a counter-propagating shock, and like COAX, uses spectroscopy to diagnose and detect the interaction. My research analyzes the successful shots,

indicating aspects of successful detections and suggests improvements to future iterations of the design.

CHAPTER 1

Introduction

1.1 What is high-energy density physics?

High-energy density physics (HEDP) is a relatively modern field of physics lying at the intersection of plasma physics, fluid dynamics, quantum mechanics, nuclear physics, and astrophysics. Researchers of HEDP study systems having material and radiation pressures greater than one million atmospheres ($1\,\mathrm{Mbar}$) [1]. They can be found in rare, impeccably precision-engineered places on Earth, such as massive laser facilities that can deliver megajoules of energy to lasers that irradiate and drive the waves needed to compress, shock, or heat material to millions of degrees in unique studies; they can also be found in nature, for example in the hot, plasma interiors of countless stars and other energetic astrophysical phenomenon such as the shock-heated gases of a supernova blastwave [1]. But before more precisely addressing the regimes of how we or nature can make HEDP conditions, we must consider what one million atmospheres means. We note that other useful expressions of $1\,\mathrm{Mbar}$ are $1 \times 10^{11}\,\mathrm{J\,m^3}$ or $1 \times 10^{12}\,\mathrm{erg\,cm^{-3}}$.

Most of the world experiences nearly $1\,\mathrm{bar}$ daily, the atmospheric pressure at sea level. Save for the heavily reinforced hulls of research submersibles that can house them, no human has even come close to experiencig the pressures at the bottom of the ocean, roughly $1000\,\mathrm{bar}$. (In fact humans likely cannot survive more than $100\,\mathrm{bar}$!). Yet HEDP regimes access pressures *1000 times greater this*. To get to this pressure, consider the energy required to separate the only bound electron from the orbit of the hydrogen atom: $13.6\,\mathrm{eV}$ or approximately $2.2 \times 10^{12}\,\mathrm{J}$. To nearest units, this implies that the internal energy of a hydrogen atom is on order of $1\,\mathrm{Mbar}$ to $10\,\mathrm{Mbar}$. The immediate implication from this is that to achieve high energy density conditions, we must confine enough energy to ionize hydrogen. Put another way, as the units of pressure are equivalent to an energy per unit volume (for example $\mathrm{erg\,cm^{-3}}$), to achieve high-energy density conditions we must apply

enough pressure that can compress and heat the molecules of a material to a degree that ionizes and frees its electrons. Such an ionized media is indeed a plasma, but often conditions in HEDP are still too dense to use much of traditional plasma theory. In fact, HEDP systems can exist in a wide range of densities and temperatures – for example we may have low-density, hot plasmas that are still collisional or those that are barely collisional; in some cases they can approach dense, strongly-coupled plasmas. Figure 1.1 illustrates the large parameter space accessing HEDP regimes, including some notable phenomenon such as the temperature and density space of stars like the sun [1].

The universe is host to endless astrophysical objects and phenomenon spanning many regimes of HEDP: planetary interiors, the interiors of stars, supernovae, astrophysical bow shocks, protostellar jets, black hole accretion disks, and many other highly-energetic processes [6, 7, 8, 9, 10, 11, 12]. It only makes sense that HEDP researchers can use and develop modern facilities to access and study these regimes. This is precisely what scientists do in the field of high-energy density laboratory astrophysics (HEDLA), scaling experiments having unfamothable spatiotemporal differences to their astrophysical counterparts [13, 14, 15].

It also makes sense to push this research to its frontier: bringing processes found only in stellar interiors to the laboratory and harnessing the power of nuclear fusion. Incredible investements and efforts are ongoing to create conditions for fusion to occur, arguably the most notable being the inertial confinement fusion (ICF) campaign. While there are a number of approaches being investigated, the typical ideas revolve around compressing shells of material to such a high degree of energy density that fusion can occur in a deterium and tritium fuel [16]. Recent results indicate that scientists are getting closer to ignition goals using this very idea [17]. Regardless of the precise method, the goal of fusion is perhaps the largest endeavor in HEDP science and its fruition would mark a truly monumental technological achievement in human history.

1.1.1 Using HEDP platforms to enable HEDLA

It may still be a wonder that we are able to study astrophysical processes in the laboratory. Despite being able to reach astrophysical temperatures, densities, and pressures here on Earth, laboratory experiments are routinely many orders of magnitude different than the astrophysical processes they attempt to emulate. Furthermore, the length and time scales

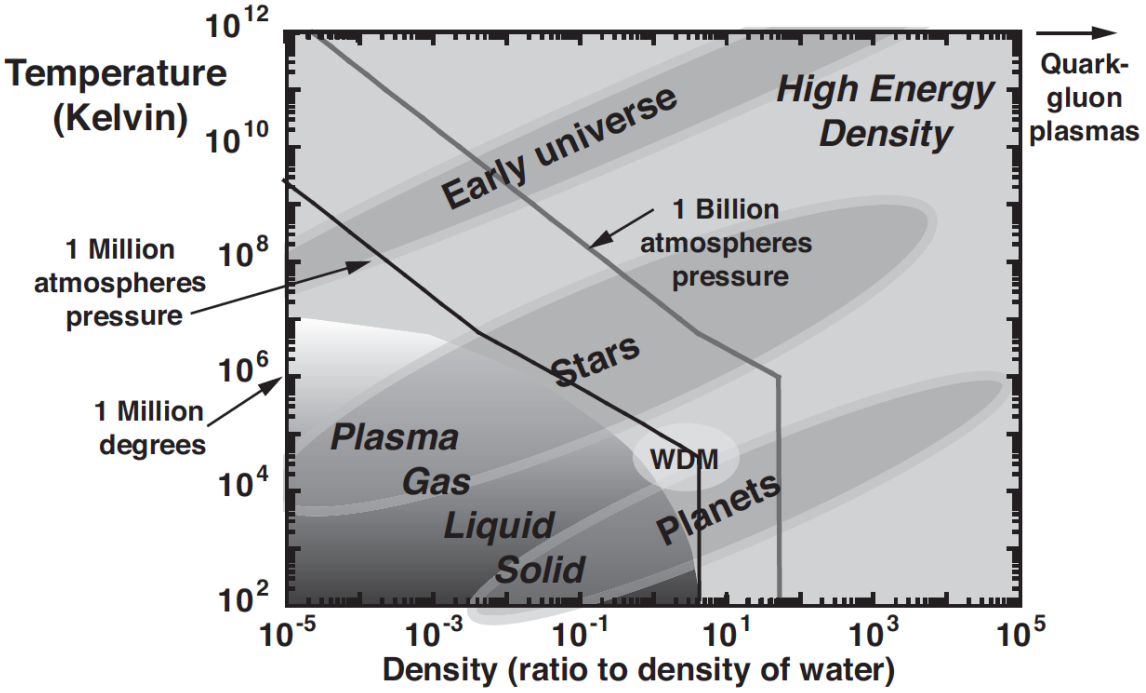

Figure 1.1: From *High-Energy Density Physics: Foundations of Inertial Fusion and Experimental Astrophysics* [1]. Regimes of high-energy density physics in connection to some astrophysical phenomenon as a function of density and temperature.

are often vastly longer as well; for example, a process in supernova shock breakout may be said to hydrodynamically evolve on order of 500 seconds, whereas a lab study may evolve on order of 5 nanoseconds, as was found in the pioneering analysis by Dmitiri Ryutov [18]. To enable a study of the dynamics in supernova remnants [19], or even a cosmology study such as the one discussed here [20], this time scale grows from years to millions of years. This enormous time scale often limits our abilitiy to capture the dynamics, restraining our knowledge of these systems to theoretical models and computer simulation. Laboratory astrophysics seeks to meaningfully contribute to astrophysical understanding by emulating the dynamics on a more human time scale. Thus the question emerges when comparing two seemingly disparate hydrodynamic systems: are the physics describing one capable of explaining the other via a simple set of transformations? Scaling analysis can be employed to help answer this question [18].

We must first determine that the same equations apply to each system. For purely hydrodynamic systems, this means that the Euler equations apply (which will be discussed in Section 2.1). Furthermore, each term in the equation set needs to apply in the same way. Both of these straightforward criterion establish physical consistency between the experi-

ment and astrophysics. Additionally, in the phenomenon where magnetic fields do no more increase a plasmas collisionality and others where radiation may be a prominent feature, it may be that the astrophysical or laboratory system behaves hydrodynamically.

This preparation must be confined by characteristic time scales τ and length scales L of each system, necessary for determining the roles of viscous dissipation via the Reynolds number, energy loss due to radiative cooling, and other quantities. For Eulerian systems, next comes the Ryutov scaling, or establishing that the Ryutov number of each system $u^*\sqrt{\rho^*/p^*}$, are roughly equivalent. Here velocity u^*, density ρ^*, and pressure p^* are characteristic state variables of the system.

Finally, the need for specific scaling arises. Establishing that a pair of systems has Ryutov scaling is direct and can often be done in a straightforward manner. However, ideal Ryutov scaling would require that the initial conditions in each system have the same profile, which is seemingly impossible in practice. Because boundary conditions cannot be perfectly matched between systems, it is essential to determine a set of dimensionless parameters that characterize the dynamics. These must have similar values between systems. Refining the regime of applicability relies on constraining these parameters and herein is the challenge of designing a well-scaled experiment.

As a final note, scaling and similarity analysis is not limited to purely hydrodynamic systems, or even those that can be approximated as such, as may be the case for radiative systems that entrain the photons and thus allowing a fluid treatment. For example, for some studies regarding magnetic jets or radiation hydrodynamics, scaling analysis may be extendable via radiation Ryutov number or other relevant work [21].

HEDLA yields a number of incredible findings truly relevant to astrophysical processes and exact astrophysical objects. Using this basic framework of scaling, facilities that can produces astropnomical temperatures and pressures, and building successively on experiments in the community. Historically this is a young field, only beginning roughly 30 years ago (see [22, 23, 24] for some early examples). Since then, scientists have helped explain the opacity problem in Cepheid variable stars by performing spectroscopy measurements on a laser experiment [25]; successfully executed scaled experiments explaining the formation of jets in the young star HH110 and the plumes in the Crab nebula [26, 27]; modeled the role of Rayleigh-Taylor in supernova shock breakout with significant circumstellar media, with direct application to SN1993J [28]; and designed a large number of others.

Some of these experiments can be more phenomenological in nature, for example demonstrating how small, seed magnetic fields can amplify in turbulent magnetic dynamos, such as those found in black hole accretion disks [29]. A number of other experiments can break apart complex processes to study more highly specific pieces of relevant astrophysics. One such example is the measurement of iron-opacities to help understand equation of state physics found in the solar interior [30]; another measures the x-ray diffraction of ice that fills missing data in the phase diagrams of water at planetary interior conditions [31] – remarkably, such experiments do not need scaling as they are conducted at actual astrophysical state values.

1.1.2 The role of radiation flows in HEDP

Significant radiation effects are a natural consequence of many high-energy-density systems – below the energies of nuclear radiation (such as decay) all matter gives off radiation purely from thermal motion. Ionized plasmas in HEDP have a lot of energy (recall, energy densities are in excess of megabars) and typically radiation can become important to the evolution of hydrodynamic flows as electrons and radiation can undergo strong interactions. Most energetic astrophysical processes too must account for this in one way or another, via simplifications to or assumptions in the equation of state, modification of the equations of hydrodynamics via terms that couple radiation to matter, or even full solution to the equations of radiation transport. Several resources derive in detail the physics of radiation hydrodynamics, radiative transfer in astrophysics, and more tailored, HEDP relevant radiation hydrodynamics [1, 32, 33].

Because of this importance, radiation flow experiments have been among the forefront of high-precision experiments, driving many research efforts to create quality validating data sets for various stages in the evolution and in a wide phase-space of basic radiation flows. They are also among the simplest of designs. Typically called radiation or shock tube experiments, they generally use a basic foam cylinder doped with a metal oxide attached to an ablator or a *hohlraum*, although some scenarios may use both. When a laser irradiates an ablator, the heated ablator material ejects from the irradiated surface and typically drives a shock wave in the direction opposite to the ejection, producing a flow-structure not too dissimilar from rocket mass ejection. When a laser irradiates the inside of the metal can of a hohlraum, the heated plasma can efficiently produce X-ray fluxes that can flow into the

target. These fluxes then drive a radiation wave down the foam target whose dopant enables various kinds of diagnostics. An example diagram illustrating a radiation tube experiment is shown in Fig. 1.2.

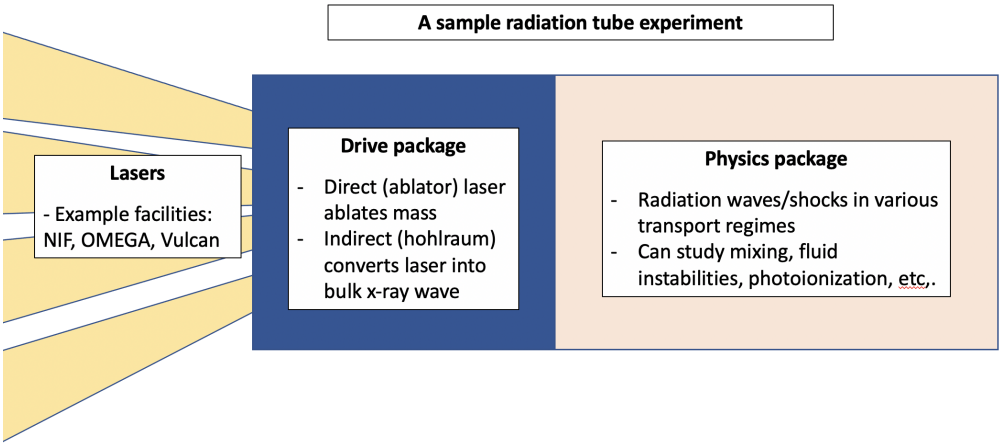

Figure 1.2: A typical radiation or shock tube design has lasers irradiating a drive package which can drive a shock or a radiation wave into a foam-based physics package. The physics package itself can be modified to study a number of physical processes such as supersonic radiation waves, fluid and plasma instabilities, and transport through inhomogenous media.

In 1958, Marshak was the first to derive the theory of radiation waves, often called Marshak waves, and provide an analytical model for their evolution under local thermodynamic equillibrium (LTE) conditions [34]; he also identified two phases of flow: supersonic Marshak waves in which the wave travels faster than the speed of sound of the material, and subsonic waves which travel slower. The latter are considerably more complex and may strongly deviate from a simpler radiation diffusion based solution (discussed in Subsection 2.2.4).

It took over 30 years to begin development of consistent, well-tested experiments of radiation waves. The first experiment used a leaded-styrene foam and X-ray streaked cameras to measure the time it took a supersonic radiation wave to exit the target. [35]. Since then there have been a large number of similar experiments from several groups, predominantly studying supersonic radiation waves [36, 37, 38, 39, 40, 41, 42, 43, 44, 45, 46]. Only until recently have experiments attempted to directly diagnose the supersonic-to-subsonic transition [5, 47]. These experiments are still under intense development, as modelers realize large insufficiencies in equation-of-state, opacity, laser-matter interactions and hohlraum

modeling, analytical and numerical models, and general uncertainty quantification efforts (see [48] for a useful investigation of supersonic Marshak waves, unifying the various experiments; [45, 46, 47] also serve as good resources for the discussion of modeling difficulties).

Also important are radiation-dominated shocks, where radiation cannot effectively diffuse out and thus becomes entrained in the shock, and radiative or diffusive shocks, where the radiation can leak from the shock front and thereby significantly affect the shock dynamics [33]. Thus there are a number of scenarios that alter the behavior of radiation and shocks in both the laboratory and in astrophysics, and shocks may transition between the types of radiation-trapped or free-streaming scenarios [49]. Nonetheless, these shocks are common in many HEDP systems, and they often serve as platforms for studying more advanced physics such as supernova shock breakout (e.g. [8]) or seeding other interesting phenomenon such as hydrodynamic instabilities (e.g [50]).

1.1.3 How do we study HEDP?

In general, a modern researcher of HEDP has several tools at their disposal, typically beginning with pen, paper, and computational resources. There is the role of the theorist, who may investigate and integrate a wide variety of fields relevant to HEDP; employ mathematical modeling and techniques to develop new physical relationships, approximations, and analytical solutions; and provide foundational theory which we can put to the test. The experimentalist is likely to implement a design and drive its successful execution, in addition to the developing new experimental techniques and diagnostics, as well as processing of the diagnostic data. The comparison between theory and experiment is critical to improving our physical understanding of any system and this process is called validation.

The computational researcher may have a number of roles such as designer, someone who designs and numerically models experimental platforms and diagnostics, typically using and developing highly-advanced and state-of-the-art research codes at universities or national laboratories. A computational researcher may even model a more specific aspect of HEDP such as laser-matter interactions, to help implement and enable new algorithms for modeling how lasers drive experiments, or they may more directly design an experiment, say to study supernova shock breakout. The role of the computational researcher is typically a more blended one between experiment and theory, however, it seems common that a researcher in HEDP may take on any number of the roles simultaneously or in vary-

ing stages throughout their career.

Phenomenon in HEDP are inherently complex, non-linear, multi-physics problems and often we require advanced simulations using state-of-the-art research codes. Examples of such codes are The University of Michigan's CRASH code [51], the University of Rochester FLASH code [52], and the Los Alamos National Laboratory code Cassio [53]. Each of those codes have fundamental differences in physics: how the radiation and laser drives are modeled, what equation of states and microphysics options are included, and which extra multi-physics capabilities are available, such as solvers for gravitational potential. They have different approaches to the purposes, algorithms, and solvers, as well as schemes to integrate all the different physics together. However, every year each of these codes are used to model HEDP experiments, problems relevant to ICF, astrophysics, and more.

In the laboratory, a number of facilities worldwide are available to create HEDP conditions. Aformentioned laser facilities can provide the power that power strong shock waves and radiation waves. In the United States, the Omega Laser Facility at the Laboratory for Laser Energetics can provide either few, long, powerful pulses to drive many HEDP studies (Omega EP) or a short-pulse laser platform that can concentrate many high intensity lasers on targets (Omega 60). The National Ignition Facility is the world's largest and highest energy laser facility, capable of producing drives needed for state-of-the-art ICF studies. Both facilities are accessible by HEDP researchers at national laboratories and universities worldwide. Pulsed power facilities such as the Z-Machine at Sandia National Laboratory can create and confine plasmas to study a variety of unique HEDP aspects such as ablation, compact dynamical formation of plasmas, and magnetohydrodynamics.

1.1.4 Validation, verification, and uncertainty quantification of HEDP experiments

Code verification is a process of ensuring that our research codes do what we design them to do. This means developing highly-accurate numerical solutions and analytical solutions that the code must produce. One such famous test that any quality hydrodynamics code should reproduce is the Sedov verification problem [54] (briefly discussed in Subsection 2.1.3). Ideally (but not often practically) each piece and coupling of physics in the multi-physics problem will have some analytical solution, for example, compressible hydrodynamics by itself under the assumption of an ideal gas can use the aforementioned Sedov

solution as one possible test.

Validation is the process of ensuring that the codes actually model the real world. This means the design and development of high-precision, theory tested, well-designed experiments that can be compared against the numerical models of the codes. For simple experiments studying fundamental physics (often even in simple cases), this is one of the most important and difficult challenges of high-energy density physics.

Finally, uncertainty quantification (UQ) is the process of quantitatively describing how our numerical solutions and their comparisons to other solutions or experimental data may fail. This is done by deducing and propagating errors in every step of modeling down to the solution. In experiments this may mean understanding the uncertainties in target densities, laser pulse energies and durations, diagnostics, and processing of diagnostic data to yield the desired comparable data, e.g. [46]. In simulations this may mean understanding numerical errors, the limits and deviations from analytical solutions or ideal cases, and simplifications that do not accurately represent a diagnostic process. Unfortunately, both of these lists are hardly exhaustive and the UQ process can be a truly arduous, daunting task.

1.2 How this thesis is organized

This thesis considers the computational design, modeling, and analysis of three experiments in HEDP, all of which explore and deal with radiation flows. The first experiment is a HEDLA platform to study the Kelvin-Helmholtz instability relevant to galactic formation; the experiment itself is in the adiabatic approximation (meaning radiation transport has little effect on the overall dynamics) but designs the problem considering how the adiabatiic limit is invalid when radiative fluxes become important. The second experiment is a radiation flow experiment called COAX that models and diagnoses the transition of a supersonic Marshak wave to a subsonic wave. This novel experiment highlights the process of validation and uncertainty quantification. The third is an experiment called Radishock that studies the head-on collision of counterpropagating supersonic radiation waves and shocks.

This first chapter outlines the key areas of contribution and the topics requiring further exploration to help contextualize these contributions. It provides useful history and research that this work is built upon. In Chapter 2, I develop the theoretical basis essential to understanding my research, first discussing fundamentals of hydrodynamics and

radiation hydrodynamics, and then the important pieces of physics needed to model the experiments and diagnostics. Chapters 3 through 5 are self-contained accounts of directed research into each of the described experiments – Ch. 3 and 4 are reproduced from published manuscripts and Ch. 5 from work under current scientific investigation. Chapter 6 closes the thesis, summarizing the work, proposing future work, and providing closing remarks.

1.3 Contributions

The work presented here contributes directly to HEDP in the following ways. First, by design of the galactic filament experiment, researchers have access to a platform that can systematically diagnose the evolution of the Kelvin-Helmholtz instability. Chapter 3 directly demonstrates the Ryutov scaling and design process to study the Kelvin-Helmholtz instability of an astrophysical plasma; early results therein demonstate the successful execution of the design. Chapter 4 builds upon an uncertainty quantification framework outlined by [46] to improve validation efforts of the COAX experiment in addition to successfully inferring the temperature profile of the transitioning supersonic-to-subsonic Marshak wave; currently, the ray-trace and synthetic spectra modeling softwares I developed serve as an useful tools to the Los Alamos National Laboratory (LANL) radiation flow modeling team. Finally, Chapter 5 integrates experimental design, analytical theory, and uncertainty quantification techniques to model a difficult and novel experimental platform. The overall contributions of both Chapter 4 and 5 are progress and continual improvement of an important radiation flow compaign effort at LANL: development of the absoprtion spectroscopy platform and assessment of the codes' capabilties to accurately model radiation flows in the real-world. A significant goal is to use these platform for high-precision validation and develop more complex instability and radiation flow experiments, such as those relevant to HEDLA or radiation transport algorithm development, and this research thereby advances that goal.

CHAPTER 2

Relevant Theory

As demonstrated in the previous chapter, to understand the behavior of fluids and radiation flows and thereby model experiments in high-energy density physics, we must understand the theory of these flows. In the most basic forms of high energy density experiments we need to understand some core concepts such as plasmas as ionized fluids, wave phenomenon such as shock waves, and fluid instabilities. As I have developed and designed experiments that probe radiation phenomenon, we must also understand the process of radiative transfer, atomic physics and how radiation and matter interact, the equations of radiation hydrodynamics, and fundamental radiation flow processes such as diffusion waves and radiation shocks. Finally, once we have our models and our data, we need to know how to use analytical solutions to verify our models and use real world data from experiments and their diagnostics to validate our models.

This chapter will provide some useful quantitative descriptions of the outlined processes, providing the basic equations needed to understand them and focusing on the broader theory that is relevant to the experiments explored in this work. The chapter begins with the descriptions of fluids and formulates the fundamental equations of hydrodynamics, then continues with some key shock relations and derivations of the Kelvin-Helmholtz instability (KHI). Then I discuss an introductory theory of radiation hydrodynamics and radiation flows. In the final subsection, methods needed for producing synthetic diagnostics and how to perform basic uncertainty quantification are presented. In all sections where applicable, I make note for the interested HEDP modeler on some current numerical implementation methods and ideas.

2.1 Hydrodynamics

2.1.1 Plasmas as fluids

Conventional plasma theory describes the motion and behavior of charged particles in self-consistent electromagnetic fields – such theory is needed for much work in HEDP, such as in the study of laser-matter interaction. But often in HEDP, the timescales are long enough (here on order of nanoseconds) and the plasma is collisional enough, that we can treat the plasma as a fluid of one (single fluid approximaton) or multiple fluids (e.g. ions and electrons) so that they may be described by the equations of hydrodynamics. Long timescales can mean that microscopic behavior does not affect bulk motion or that certain instabilities can be damped and neglected. Collisionality is a result of the particles in the plasma having a shorter mean-free path than some observational length scale ($\lambda_{mfp} \ll L$). Collisionally-dominated plasmas exhibit thermal behavior, rapid local diffusion of velocity and temperature, and generation of collective pressures. All of the experiments and work listed here assume that the plasmas can be accurately treated as fluids.

One way to arrive at the fluid equations is by assuming that the plasma is not made of discrete particles but is a continuum, deriving the Vlasov equation, and taking moments of velocity of the equation. We will not do so here, but briefly motivate the concept as the idea of taking moments is intrinsic to fluid dynamics. In such a continuum configuration, the plasma is described by a distribution function $f(\mathbf{x}, \mathbf{v}, t)$, which is the number of particles per unit volume having position $\mathbf{x}$ and velocity (momentum) $\mathbf{v}$ at some time t. It may be straightforward to infer that taking velocity moments of this distribution, that is, integrals of f and products of velocity $\mathbf{v}$, can give us functions of position and time. In fact the zeroth-moment ($\int f d\mathbf{v}$) gives our first fundamental hydrodynamic quantity, density. The higher order moments will give us more fundamental quantities and with little careful assembly, ultimately form the Euler equations (an introductory resource describing such a derivation is [55]).

2.1.2 The Euler equations and equation of state

The Euler equations of hydrodynamics provide bulk (macroscopic) descriptions of fluid flow. For example, how fluids fill a space, compress and expand; how they heat and transport energy; how they exhibit wave behaviors and develop shocks; and how they can lead to highly unpredictable behavior in turbulent and unstable flows. The bulk description is just the *dynamical evolution of the global state* of the fluids, or how quanitites like the

density ρ, velocity v, temperature T, and pressure P change through space and time in the entire fluid system – and at their core, the equations follow mathematically deep and elegant symmetries known as continuity equations:

$$\frac{\partial Q}{\partial t} + \boldsymbol{\nabla} \cdot \mathbf{F}_Q = S_Q \tag{2.1}$$

These equations are conservation laws that express how the rate of change of some quantity Q flowing through a control volume is solely determined by how much the flux of that flow, F_Q, can spatially diverge (think compress or expand, slow down or speed up) and the net quantity per unity time added (sources) or removed (drains) in that volume, S_Q. In a more precise language for fluid flow, these quantities are those so ubiquitous in physics: mass ($Q = \rho$), momentum ($Q = \rho v$), and energy ($Q = \rho v^2$). Thus the Euler equations of hydrodynamics aptly describe the transport of these quantities in space and time *volumetrically*. One way to express the Euler equations is

$$\frac{\partial \rho}{\partial t} + \boldsymbol{\nabla} \cdot \rho \cdot \mathbf{u} = 0 \tag{2.2}$$

$$\rho \left(\frac{\partial \mathbf{u}}{\partial t} + \mathbf{u} \cdot \boldsymbol{\nabla} \mathbf{u} \right) = -\boldsymbol{\nabla} p \tag{2.3}$$

$$\frac{\partial p}{\partial t} + \mathbf{u} \cdot \boldsymbol{\nabla} p = -\gamma p \boldsymbol{\nabla} \cdot \mathbf{u} \tag{2.4}$$

In deriving the equations of hydrodynamics, each introduces a new unknown quantity. For example, in the first equation of Eq. 2.4, called the continuity equation, there are two unknowns, density ρ and velocity $\mathbf{u}$. The next equation, sometimes called the momentum or force equation, introduces pressure in the $\boldsymbol{\nabla} p$ term as another unknown. Thus there is always one more unknown than there are equations. To solve this full, general system we need one more equation, called an equation of state (EOS), that provides a relation between the state variables. Typically they are pressure equations in functional forms $p(\rho, T)$ or $p(\rho, \epsilon)$, where ϵ is the specific internal energy. The ideal gas law is arguably the most famous example of a hydrodynamic EOS. In numerical codes modeling the Euler equations, we may often choose some other calculated form of the EOS, for example via a tabulated EOS such as SESAME [56], or even other theoretical EOS forms to close the system of equations.

To get the closed form of the Eq. (2.4) we have assumed that the fluid follows a polytropic process, where $pV^n = \text{const}$. Here n is called the polytropic index and can take special values depending on the particular thermodynamic process. Also observing the in-

verse relation between volume and density we can infer $p \propto \rho^n$. A useful EOS form, often referred to as a *gamma-law gas EOS*, reads

$$p = \rho\epsilon(\gamma - 1) \tag{2.5}$$

This equation is derived directly from the ideal-gas law, which has more generally seen forms

$$p = \rho RT, \text{ or } \rho\epsilon = \frac{n}{2}RT. \tag{2.6}$$

for a system of particles having n degrees of freedom, where R is the so-called gas constant. As an aside, a commonly used relation in HEDP for the specific internal energy ϵ comes from the thermodynamic relation for the specific heat at constant volume:

$$c_V = \left(\frac{\partial\epsilon}{\partial T}\right)_P = \frac{n}{2}R \quad \longrightarrow \quad \epsilon = c_V T \tag{2.7}$$

We refer the reader to [1] for more relevant discussion on the ideal gas EOS. Due to its simplicity and wide applicability, the equation of state of 2.5 is often a useful starting point. Furthermore, in certain limits this equation allows an effective set of hydrodynamic equations and provides elegant relations for hydrodynamic quantities (e.g. in wave behavior or strong shock analysis as seen in the following subsection). In most real-world cases, the true EOS of a particular material may be unknown or incomplete due to lack of experimental verification or theoretical development.

How we arrived at this system of partial differential equations (PDEs) is also readily motivated phenomenologically (instead of the Vlasov approach for example). From the description of Eq. (2.1), we can identify that the quantity of interest is density (mass per unity volume), $Q = \rho$, and that the flux is the product of density and the velocity vector $\mathbf{F} = \rho\mathbf{u}$. We can then choose the common assumption that there are no sources or sinks of mass $S_Q = 0$. Now consider a volume element, a fixed region in space having dimensions dx, dy, and dz such as the one shown in Figure 2.1.

A fluid of arbitrary density ρ may flow through any of the faces of the volume at an arbitrary velocity, in or out of the volume. Just considering the flow in the $\hat{x}$ direction, the areal mass per unit time that enters the volume is $\rho(x,t)u(x,t)dydz$ at the left face $|_x$ and exiting the volume is $\rho(x+dx,t)u(x+dx,t)dydz$ at the $|_{x+dx}$ face. We indicate that the density and velocity are allowed to spatially vary as functions of position and time. The

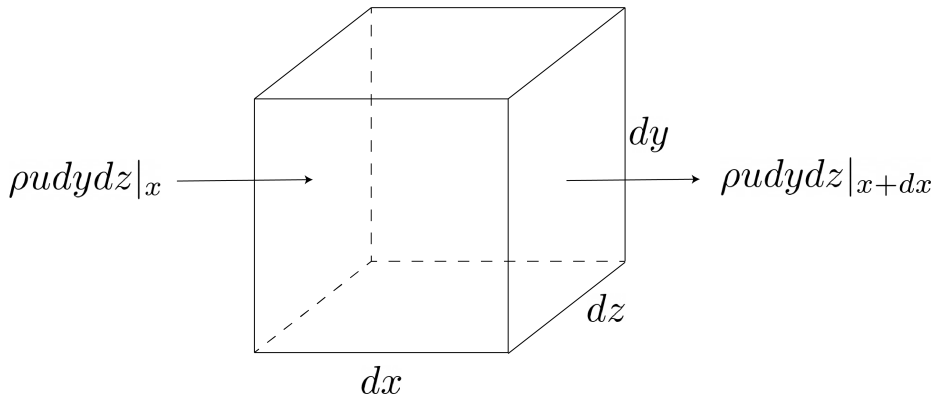

Figure 2.1: We consider an imaginary control volume in a fluid with density ρ and flow velocity u in the $\hat{x}$ direction. The volume has dimensions dx, dy and dz.

change in the mass is then

$$\frac{\partial \rho}{\partial t} dx dy dz = (\rho u|_x - \rho u|_{x+dx}) dy dz \tag{2.8}$$

Diving by the volume $dxdydz$ and taking the limit as dx approaches zero, we can arrive at

$$\frac{\partial \rho}{\partial t} = \frac{(\rho u|_x - \rho u|_{x+dx})}{dx} = -\frac{\partial (\rho u)}{\partial x} \tag{2.9}$$

By continuing this process for the other faces, we arrive at the full gradient operator $\nabla \rightarrow \frac{\partial}{\partial x} + \frac{\partial}{\partial y} + \frac{\partial}{\partial z}$ and therefore the continuity equation expressed in Eq. 2.4. And in a straightforward manner we see that we are deriving mass continutity for a fixed volume (therefore density is a sensible quantity to track here). Alternative formulations of the equations of hydrodynamics do exist, such as the Lagrangian formulation which chooses a fixed mass element with a variable control volume (or even mixed formulations like arbitrary Lagrangian-Eulerian or the alternative approach of smooth particle hydrodynamics). The difference can be thought of as fixed probes in a flow field (measuring a volume in a fixed grid) in the Eulerian case vs probes that flow with the fluid (staying with a mass element) in the Lagrangian. I stick to the Eulerian version, as they comprise nearly all the results described here.

Solving the equations of 2.4 is not often an easy task. Limited analytical models may exist for a particular problem and one almost always relies on implementing numerical methods or using a developed hydrodynamics code. HEDP and astrophysical phenomenon are certainly rarely as simple as Eqs. 2.4, and these phenomenon almost always require even more physics. First, Equations 2.4 assume the plasma is a single fluid, when in reality

there may be multiple fluids, or even multiple species (e.g. ions) that require more special care. This especially true when reactions between ions must be considered – FLASH is a modern code that tackles this, for example [52]. At the very least, many modern simulation codes may model the problem as a two fluid system, one for electrons and one for all ions present. Excluded from this model are how fluids with different properties such as equation of state may mix.

As HEDP phenomenon are routinely multi-physics, we may need electromagnetism, gravity, radiation transport, turbulence, viscosity, and other models. A more general version [1] of the momentum equation, attempting to broadly incorporate such effects may look like

$$\rho\left(\frac{\partial \mathbf{u}}{\partial t}+\mathbf{u}\cdot\boldsymbol{\nabla}\mathbf{u}\right)=-\boldsymbol{\nabla}p+\mathbf{F}_{EM}+\boldsymbol{\nabla}\cdot\sigma_{\nu}+\mathbf{F}_{\text{other}}. \tag{2.10}$$

In this equation, $\mathbf{F}_{EM}$ is a flux term accounting for electromagnetism, $\boldsymbol{\nabla}\cdot\sigma_{\nu}$ is a term for viscous effects, and $\mathbf{F}_{\text{other}}$ can represent additional flux sources. Multi-physics hydrodynamics are not limited to such a form, but this equation illustrates how complex the problem can quickly become with more physics. A multi-physics energy equation becomes almost intractable and we refer to [1] for an example.

How these multi-physics problems are solved numerically is a massive field of active research, but we briefly discuss some concepts in computational fluid dynamics. One common approach to solving the Euler equations is to use operator splitting. In this approach, each of the physics pieces is separated into operators on a well-defined state vector (for example the variables $\mathbf{X}=(\rho,\rho u,E)$), so that $\mathbf{F}=\mathbf{F}(\mathbf{X})$ is a flux operator term specific to say hydrodynamics, gravity, or electrodynamics. The whole problem, even Eqs. 2.4, can then be cast in a so-called strong conservation form [57]

$$\frac{\mathrm{d}\mathbf{X}}{\mathrm{d}t}=\mathbf{F}(\mathbf{X})+\mathbf{G}(\mathbf{X})+\ldots \tag{2.11}$$

Each of the operators $\mathbf{F},\mathbf{G},\ldots$ can then be solved independently, so that the new state $\mathbf{X}^{n+1}$ can be updated by whatever time-stepping scheme (i.e. explicit for forward-time marching or explicit for backward-time marching) [58].

The numerical solution is then performed on discretized grid, where the continuous space and time variables are gridded into steps of size Δt and Δx_i for each x_i dimension being modeled. Choice in grid resolution and time step size are critical considerations. First, certain resolutions are required for numerical stability of the solver. For basic advec-

tion in fluid flows, in order for a solver to be stable the time step Δt must be below the time required for information to propagate at a speed u across a grid of size Δx

$$C = u\frac{\Delta t}{\Delta x} \leq 1 \tag{2.12}$$

This value C is called the Courant-Friedrichs-Lewy (CFL) number, with the inequality called the CFL condition. Second, high resolution is essential to ensure that a solution is convergent, that is approach a limiting state as resolution increases, and accurate, whose errors decrease with increasing resolution. For example, in choosing a CFL we may choose time steps so that $C = 0.5$ for a given grid size Δx, if we wish to resolve finer evolution of a flow.

However, this may not be the limiting factor in our simulation, as often in problems of interest we may be interested in things other than bulk flow, such as chemical reactions, turbulence, instabilities, or other physics that require high spatiotemporal resolution. We may wish to only prioritize the global flow, having some system length L, or some instability evolution, having a length scale l, or we may even be interested in the fine-scale structure of say mixing of fluids on the unstable interface at a scale λ. For most real-world applications, assuming the CFL and other necessary stabiltiy conditions are satisfied for some timestep Δt, we may wish to choose a grid size so that $\lambda < \Delta x \leq l < L$.

Another important consideration in modeling is diffusive error. For example, a 2D rectangular Eulerian grid may be tiled neatly in a xy rectangular grid, advecting flow neatly to the left and right of each cell in x, and up and down in y. This works wonders for flows perfectly in $\hat{x}$ or $\hat{y}$. But a flow diagonal to this element cannot be advected neatly in a diagonal direction, so some portion of the flow must be advected to the left, right, top, and bottom cells. One can imagine this exacerbating the more and more cells this flow traverses. The end result is a smearing of the flow, called numerical diffusion, which is an erroneous spreading of the fluid state across cells. (Note that this is separate from artificial viscosity, which is sometimes used to make solutions more stable, e.g. modeling shock fronts). In summary, a modeler that may need accurate flows should estimate kinematic viscosity and diffusion rates and improve resolution so as to not be dominated by numerical diffusion – although sometimes this can be an impossibility.

These are only a few introductory considerations. A computational modeler may need to implement hydrodynamics solvers, develop new methods, or include new physics to existing solvers of the basic Euler equations. A computational modeler should at least un-

derstand the basic schema for solving these equations numerically. For more information, I refer the reader to the resource by Zingale [59].

2.1.3 Waves and Shocks

Waves are small-amplitude disturbances that propogate through a medium. While there are non-linear waves (e.q. weakly non-linear waves in the Burgers' equation or Boussinesq equation) in most cases they can be treated as a fundamentally linear phenomenon. To see this simply, we consider a static (motionless) fluid with density ρ_0 and we introduce a very-small, density perturbation ρ_1 at some point in the fluid, $\rho \to \rho_0 + \rho_1$. We will assume that this in turn causes the initially static fluid to move and displace the perturbation, so that $\mathbf{u} \to u_1$. In the fluid equations (2.4), we can assume that products of the perturbed quantities are zero (very, very small) and that of course derivatives of the constant quantities are zero. This process is called linearization and is a powerful tool that can be used to find linear behaviors in complex, non-linear equations. This produces

$$\frac{\partial \rho_1}{\partial t} + \rho_1 \boldsymbol{\nabla} \cdot u_1 = 0 \tag{2.13}$$

$$\rho_0 \frac{\partial u_1}{\partial t} + \frac{\partial p}{\partial \rho} \boldsymbol{\nabla} \rho_1 = 0 \tag{2.14}$$

Through some manipulation of these equations we can arrive at

$$\frac{\partial^2 \rho_1}{\partial t^2} - c_s^2 \boldsymbol{\nabla} \cdot \rho_1 = 0, \tag{2.15}$$

where $c_s^2 = \partial p / \partial \rho$ is the square of material sound speed; for our polytropic EOS this can be expressed as $\gamma p/\rho$ or equivalently $(\gamma - 1) c_V T$. This second order linear equation is a wave equation that can be solved using the method of characteristics. The resulting solution dictates that our disturbances are actually waves, traveling at the sound speed $\pm c_s$. A logical following question is can disturbances travel faster than c_s? The answer is *yes* and those disturbances are called shocks. We may describe such flows as supersonic, conveniently expressed by the unitless Mach number $M = u/c_s > 1$, where u is the speed of the flow. Flows with a Mach number, $M < 1$ are subsonic.

Supersonic flows ($M > 1$) exhibit special behavior, including that they can rapidly thermalize matter that they pass through. While a wave is a continuous disturbance, the shock is a sharp discontinuity. In one dimension, for a shock travelling through some constant density, we can think of left of the discontinuity as the shocked region and right

of the shock as unshocked material. In the stationary shock frame, the material is seen as moving through the shock from right to left (hence upstream is ahead of the shock and downstream is before the shock). We consider some of the more important relations of a shock, which are essential to any HEDP specialist's toolkit – these are the Rankine-Hugongeiot relations:

$$\rho_1 u_1 = \rho_2 u_2 \tag{2.16}$$

$$\rho_1 u_1 + p_1 = \rho_2 u_2 + p_2 \tag{2.17}$$

$$\rho_1 u_1 \left(\epsilon_1 + \frac{u_1^2}{2}\right) + p_1 = \rho_2 u_2 \left(\epsilon_2 + \frac{u_2^2}{2}\right) + p_2 \tag{2.18}$$

In this result we have again used the polytropic assumption. The Rankine-Hugoneiot relations in a more general form are particularly useful for making EOS measurements in high-energy density conditions, but with this assumption are very useful for calibrating codes. Furthermore, they have special simplificitations for when the Mach is sufficiently large ($M \gg 1$). Such shocks traveling sufficiently fast are called *strong shocks*. These are often so important, that they serve as useful benchmarking tools in many scenarios with shocks, and two particularly useful relations for these are

$$\rho_2 = \left(\frac{\gamma+1}{\gamma-1}\right)\rho_1 \tag{2.19}$$

$$T_2 = \frac{4(\gamma-1)}{(\gamma+1)^2}\left(\frac{1}{2}\frac{\mu m_p}{k_B}\right)u_1^2 \tag{2.20}$$

Here we have introduced the mean molecular mass, $\mu = \bar{m}/m_p$, where $\bar{m}$ is the average mass of the ions and m_p is the mass of the proton. Note that we can readily convert between density and mean molecular mass via the relation, $\mu = \rho/(nm_P)$. The first of these two results, dictates that there is an ideal fixed limit to the shocked density, meaning that a shock may not compress more mass per unit volume than this. For $\gamma = 5/3$, as in the case of a monatomic ideal gas having three degrees of freedom partitioned by only kinetic energy, the density limit is 4 ($\rho_2 = 4\rho_1$). For radiation-dominated gases with $\gamma = 4/3$, as we will later explore, the density limit is 7. The second result provides an expection of how hot a shocked gas should get and is only a function of the shock speed. Thus in many scenarios we can directly turn a velocity into a temperature to understand better the state of our shock system. This relation can be evaluated early in studies where shocks are present to determine the importance of radiation in a system.

While shocks arise mathemtically from the fact that there are non-linear terms such as

$\mathbf{u} \cdot \nabla \mathbf{u}$ in the Euler equations, they are indeed real and important phenomenon, ubiquitous in HEDP, astrophysics, ballistics, aircraft, and elsewhere in the real-world. Thus accounting for them in hydrodynamics solvers is required for any HEDP capable code. Solving for the state variables as the shock discontinuity evolves is called the Riemann problem, and remarkably, gives an exact solution to shock behavior [57]. Riemann solvers enable the numerical solution steepening waves, shocks, and other discontinuities in hydrodynamics codes and a number of approaches tackle this difficult numerical problem [60, 61, 62].

Since we require codes to model HEDP experiments, it is worth re-mentioning the Sedov problem [63], which both serves as a useful shock verification test as it provides an analytical solution to compare codes against, and for reference when developing physics intuition and a basis for more advanced studies of shock flows. This is demonstrated in a co-authored work studying shock breakout [64]. The Sedov problem describes a point source explosion occuring in an initially uniform density (an energy E_{ex} is rapidly deposited into a very small, finite region). The resulting shock flow is described by a self-similar solution, derivable in any 1D geometry, and is easily compared to code solutions [54].

2.1.4 Hydrodynamic Instabilities

In the previous sections we saw how the phenomenon of waves results from small disturbances or perturbations to a fluid flow. This is easy to see in nature by throwing a stone in a pond and observing the rippling waves flowing outward. But in this case the resulting disturbances (waves) actually never grow in amplitude, aside from the limits of the non-linear shock (i.e. the wave is never higher than the initial perturbation). What happens when the amplitude grows? Such a phenomenon is called a *fluid instability*: a fluid disturbance that creates flows that will grow in amplitude. Arguably two of the most common fluid instabilities are the Rayleigh-Taylor instability (RTI) and the Kelvin-Helmholtz instability (KHI), and examples of these instabilities are seen often in nature. Briefly discussing the first (RTI) is useful to develop an intuition for the second (KHI) which is one of the focuses of research in this thesis.

The RTI occurs at the interface of two fluids of different density, in which one fluid is accelerated into another. The RTI causes interpentration of the two fluids, each forming plume-like structures in one another as they attempt to mix. In the simplest case, the fluids may be inviscid (negligible viscosity), immiscible (negligible mixing of fluids), and the acceleration can be caused by gravity, with the heavier, denser fluid on top of the other.

How these plumes grow into one another requires some detailed stabilitiy analysis on the linearized Euler equations. This linearization process was briefly demonstrated for wave behavior in Subsection 2.1.3, but the stability analysis begins by assuming that the amplitude of the instability a can oscillate in space and time it evolves. If we assume there is some sinusoidal perturbation with wavelength λ, or alternatively having wavenumber spatial wavenumber $k = 2\pi/\lambda$, and that the perturbation will grow at some rate γ, then the amplitude will behave as $a(\mathbf{x}, t) \propto \exp(-i\mathbf{k} \cdot \mathbf{x} + \gamma t)$. For the basic, inviscid, immiscible, linear case, there is one key takeaway when the math is done: the growth occurs only temporally as $a \propto \exp(\gamma t)$, where $\gamma = \sqrt{Agk}$ is the growth rate dependent on the wavenumber k, the gravitational constant g, and the Atwood number $A = (\rho_2 + \rho_1)/(\rho_2 - \rho_1)$, a useful parameter appearing in several other instabilities as it concisely packages the two fluid densities.

The Kelvin-Helmholtz instability (KHI) is another interface stability, occuring when two fluids flow past one one another and a narrow transition region between the fluids creates a velocity shear. This shear flow leads to growth of perturbations into iconic roll-up (vortex) formations (Figure 2.2) when the forces are stronger than the damping forces of viscocity and surface tension, causing vortical evolution of the interface [65].

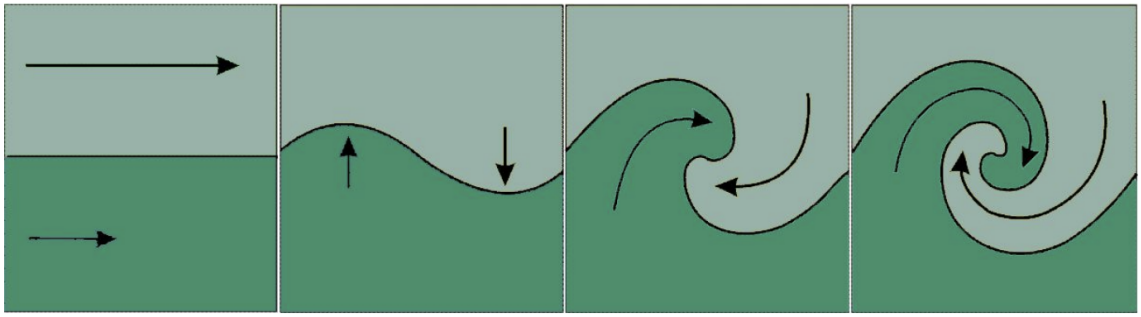

Figure 2.2: From *Kinetic projection and stability in lattice-boltzmann schemes* [2]. Where a velocity differential exists between two fluids, shear fluid flow may lead to a perturbed surface that swells, growing into iconic Kelvin-Helmholtz roll-up formations.

In a similar manner as RTI, we can derive the growth behavior of a single KHI vortex using stabilitiy analysis and linearization – Kundu and Cohen provide a detailed derivation [66]. There are few stabilizing conditions, such as viscosity and acceleration of one fluid into another, but in the research of this thesis we consider them negligible and again consider only the most basic, inviscid, immiscible, adiabatic cases. The incompressible growth

rate is [65]

$$\gamma_{ic} = \frac{k\Delta u}{2}\sqrt{1 - A^2} \tag{2.21}$$

As this growth occurs exponentially, the linear portion of the growth rate ends in a few growth cycles, when the ratio of the amplitude to the wavelength approaches 0.1, $h/\lambda \sim 0.1$. Working with this limit is essential for a well-designed experiment, as done for example in [67, 50, 20].

If dealing with incompressible fluids, which is the case for nearly any HEDP study, then we require the incompressible KHI growth rate:

$$\gamma = -i\gamma_{ic}\frac{\sqrt{-1 - M_c^2 + \sqrt{1 + 4M_c^2}}}{M_c} \tag{2.22}$$

This form uses the convective Mach number defined as $M_c = \Delta u/(c_1 + c_2)$, where c_1 and c_2 are the sound speeds of the two fluids. Readily seen from this equation is that as $M_c \to 0$, the incompressible growth rate is recovered. Furthermore, this equation is imaginary, suggesting that a higher shear velocity difference reduces the instability growth rate. Above a convective Mach number of $M_c > \sqrt{2}$, the root term becomes imaginary, theoretically eliminating the instability. However this is not the case practically, as higher-order terms neglected in this derivation become important [67]. This equation forms the basis of a key focus in the presented research [20].

2.1.5 Ryutov scaling for HEDLA experiments

While this topic is introduced in Section 1.1.1 and is thoroughly explained in [18], there is one important topic of discussion to ensure coverage for the presented research, which conveniently introduces the need for the following Section. With waves, shocks, and instabilities we can handle many situations in nature, surprisingly, even several in astrophysics. In other scenarios involving electromagnetic fields, radiation, gravity, or other special phenomenon we have to include those terms in the Euler equations as well. However, as the first step in modeling and conducting an experiment that can study these astrophysics, we have to either choose the same equations to model both, and/or, make sure that the assumptions have direct analogs (to wit: we cannot make an approrpiate gravity in the laboratory, but we can potentially create similar acceleration conditions).When the physical consistency is achieved between astrophysics, computational model, and laboratory experiment, we have to ensure that the physics between one system scales to another, with Ryutov scal-

ing [18].

One critical complication is radiation, and in many cases is a dominant physical mechanism. For example, the radiation-dominated shock in some supernova settings can be described solely with Euler equations using a gamma-law gas EOS with $\gamma = 4/3$. Since the Euler equations apply in both physical and model cases, Ryutov scaling is appropriate. In the original research presented here on studying the KHI on galactic filaments, we had to consider the role of radiative cooling on the evolution described by Eq. 2.22 . Despite radiative cooling of the unstable plasmas being an important process ,we must ensure that the overall evolution of the KHI is either unaffected by this cooling or, that the cooling occurs on a timescale that allows Eq. 2.22 be used or modified in an adiabatic, but consistent manner.

In more complicated settings requiring detailed radiation transport, however, we likely need to include the equations of radiation hydrodynamics. The reader is also referred to radiation scaling laws, which do exist for some appropriate scenarios [21].

2.2 Radiation Hydrodynamics

2.2.1 Radiative Transfer

As seen in the preceeding discussions on hydrodynamics, a natural concept in physics where energy can move in, through, or out of a system is energy flux: some amount of energy dE moves through some surface with area dA for some time dt. The flux then should be proportional to the energy per unit time per unit second, $F \propto dE/(dAdt)$ and is dependent on the orientation of the area element relative to the direction of the energy flow. Radiative transfer describes this process for radiation, where the movement of energy occurs by the propogation of radiation through a media. In this section we develop a basic framework for fundamental radiative transfer, motivated by the ray approach commonly found in resources such as those by Rybicki and Lightman [32], Chandrasekhar [68], and NASA [69], and using the example of observing a radiating star.

A ray of radiation is a simplifying construct that refers to a localized group of photons traveling in the same direction. Let us define the intensity for the ray via the following relation:

$$dE = I_\nu \, \mathbf{n} \cdot d\mathbf{A} \, dt \, d\Omega \, d\nu. \tag{2.23}$$

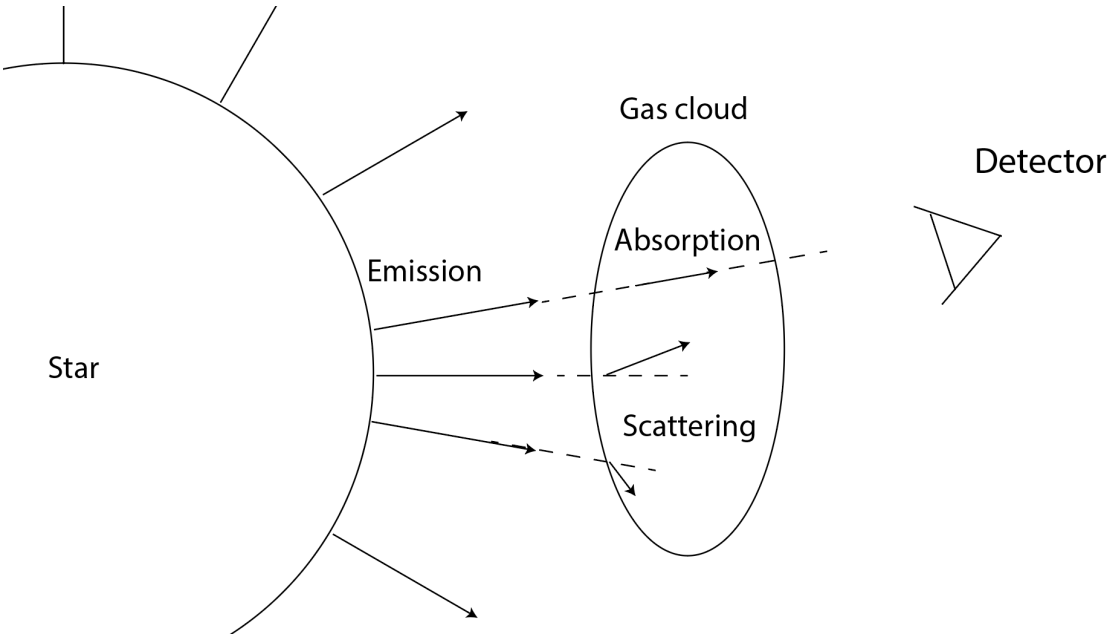

Figure 2.3: An example of stellar radiation and common radiation energy transfer processes. Rays from a star irradiating a gas cloud may lose intensity due to absorption or scattering, and other rays may even scatter into the view of a detector.

Here the ray having intensity I_ν in some frequency range $d\nu$ will experience a change in energy dE after crossing some area element with area $d\mathbf{A}$ in some time dt; the element $d\Omega$ bins the ray over solid angle. We note first that the quantity $d\mathbf{A}$ describes the normal to the crossing surface with area magnitude dA. Second, the ray has some direction of propagation $\mathbf{n}$ within a solid angle element $d\Omega$ of the ray. An example of this geometry is shown in Figure 2.4. Thus it is readily apparent that $\mathbf{n} \cdot d\mathbf{A}$ will be important for determining some radiation flux quantities. As a ray may cross through an area element, this treatment is consistent with the approach that a ray *emanates* from an area element. Furthermore, if we consider all rays that can emanate from this surface area element, it is clear that the ray can emanate at any angle, covering the space of a sphere with total solid angle $\int d\Omega = 4\pi$.

Consider an ordinary star, spherically symmetric and uniform in temperature so that it emits rays uniformly from its surface and whose net direction is radially outward. The light rays traveling from the star through space to our telescope may encounter a large region of hot gas or dust. If we consider such a system as shown in Fig. 2.3, where energy from the stellar rays may be absorbed by the dust and lost (absorption), where the hot gas may also emit its own rays and add energy to the initial stellar ray (e.g. emission), and the photons in the stellar rays may be scattered out of our line of sight (scattering). Our goal in formulating an equation for radiative transfer is then to adequately bookkeep the energy loss and

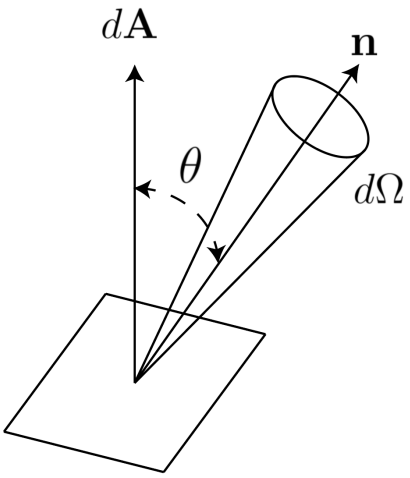

Figure 2.4: Ray geometry showing an area element with surface normal $d\mathbf{A}$, a ray traveling in direction $\mathbf{n}$ at an angle θ from the surface normal, and in a solid angle element of $d\Omega$.

gain mechanisms for the rays in our system. Consider a small element of this dust as a column with length ds and cross-section dA. A monochromatic ray with frequency ν travels in the $\mathbf{n}$ direction confined to the $d\Omega$ solid angle, passing through the length ds of the medium.

The ray traveling at speed c can either gain or lose some energy along the path ds it travels in some time $dt = ds/c$. Per unit area, solid angle, time, and frequency, this change in energy is

$$[I_\nu(s + ds, t + ds/c, \Omega) - I_\nu(s, t, \Omega)] = \frac{1}{c}\frac{\partial I_\nu}{\partial t} + \frac{\partial I_\nu}{\partial s} \tag{2.24}$$

This loss or gain is intrinsically directional and this last result is just an expression of the material derivative used in the Eulerian approach, i.e. $\frac{D}{Ds} = \frac{1}{c}\frac{D}{Dt} = \frac{1}{c}\frac{\partial}{\partial t} + \mathbf{n} \cdot \nabla$. To express the last term we must recognize that the second term in the total derivative is just the definition of the directional derivative in the $\hat{\mathbf{s}}$ direction, $\mathbf{n} \cdot \nabla \rightarrow \frac{\partial}{\partial s}$. Many references may simplify this to just the partial derivative, or assert $\mathbf{n} \cdot d\mathbf{A} = \cos\theta dA$ as in the case of a Lambertian surface.

Instead of fully developing expressions for emission, absorption, and scattering processes, here we motivate the phenomenological processes behind each in basic forms. For a simple emission model, let us assume that the medium is an isotropic emitter (equally emitting in all directions) and the energy lost by the medium is volumetric, having energy per unit volume, solid angle, frequency, and time. This distinction is important as we will

see in the discussion of blackbodies, where the emission is surface emission. We can denote this as the monochromatic emission coefficient j_ν and we represent the intensity added to the beam in the $\mathbf{n}$ direction from emission as

$$\frac{\partial I_\nu}{\partial s} = j_\nu \tag{2.25}$$

With emission only, the solution for the intensity is straightforward: the resultant intensity is the added intensity from integrating over the emission coefficient along the path the rays have traveled, $I(s+ds) = I(s) + \int_s^{s+ds} j_\nu ds'$.

For absorption, we consider a medium containing absorbers that can only remove energy from the ray via absorption along the ray path of travel. Thus we can simply assume a phenomenological law: the intensity lost dI along a a path ds is proportional to the initial intensity going into that ray

$$\frac{\partial I_\nu}{\partial s} = -\alpha_{a,\nu} I_\nu \tag{2.26}$$

Here we define the proportionality as the absorption coefficient, $\alpha_{a,\nu}$ having units of inverse unit length and unit frequency. This equation is simply the ordinary differential equation governing exponential decay (sometimes called an extinction model). Thus for processes modeling absorption only, $I(s+ds) = I(s)\exp\Big(-\int_s^{s+ds} \alpha_{a,\nu} ds'\Big)$ is the solution. In future sections, we will see how this and the emission models can be combined to form a powerful basis for understanding many astrophysical or experimental diagnostic systems.

Scattering is a more challenging problem and needs to be broken into two processes: scattering out of the ray into the volume (energy lost by the ray) and scattering into the direction of the ray (energy added to the ray). In the first process, scattering looks like an identical process to absorption with uniform scatterers:

$$\frac{\partial I_\nu}{\partial s} = -\sigma_{s,\nu} I_\nu. \tag{2.27}$$

The quanity $\sigma_{s,\nu}$ is the scattering coefficient, having units of inverse length, representing the amount of radiation scattered by the medium coming in from any direction to *any direction* – it is entirely possible that radiation can still be scattered into the field of view. But in order to understand how much scatters out of the solid angle, we must introduce a probability distribution $P_\nu(\Omega, \Omega')$ describing how much (what percentage) of the intensity of a ray I_ν will scatter from angle $d\Omega$ about direction $\mathbf{n}$ onto angle $d\Omega'$ about direction $\mathbf{n}'$

(the reader is referred to [68] for a thorough discussion).

This phase function can be rather complicated for certain geometries, but it is worthwhile to point out that it normalizes over the full 4π angle space, $(1/4\pi)\int_\Omega P_\nu d\Omega = 1$, which simply says that scattered energy must go *somewhere*. Regardless of the particular geometry, we can assume that the only parameter that matters is the scattering angle, which is the relative angle between $d\Omega$ and $d\Omega'$ (as in classic optics). Thus $P_\nu(\Omega, \Omega') = P(\cos\theta)$. Now we have a clear path to the energy change per unit volume of the media, per unit frequency, per unit time:

$$(\sigma_\nu I_\nu d\Omega') \left(\frac{1}{4\pi} P_\nu(\Omega, \Omega') d\Omega \right). \tag{2.28}$$

Finally, we integrate over solid angle to get the bulk volumetric description,

$$\text{gain due to scattering} = \frac{1}{4\pi}\sigma_\nu \int_\Omega P(\cos\theta) I_\nu d\Omega. \tag{2.29}$$

These scattering processes have features worth reiterating. Rays traveling in the Ω direction will lose energy consistent with the phenomenological laws of (2.26) and (2.27), and Equation (2.29) tells us how much intensity is added onto the ray in the $\mathbf{n}$ direction *scattered from elsewhere in the medium*, from any $d\Omega$ direction.

The only remaining task is to assemble the full, general radiative transfer equation (RTE) by combining the loss and gain terms. Starting from Eq. (2.24), we now have

$$\frac{1}{c}\frac{\partial I_\nu}{\partial t} + \frac{\partial I_\nu}{\partial s} = j_\nu - \alpha_{a,\nu} I_\nu - \sigma_{s,\nu} I_\nu + \frac{1}{4\pi}\sigma_\nu \int_\Omega P(\cos\theta) I_\nu d\Omega. \tag{2.30}$$

This is a very versatile, general, well-approximating equation. But in many applications, it contains perhaps too much information and may not be easily solvable. Often we may be in a situation where scattering losses dominate, others where emission and absorption are dominant transfer mechanisms. In the following subsections, we will refer back to Eq. (2.30) and motivate such scenarios, developing simpler, more applicable forms. When we assemble the equations of radiation hydrodynamics in Section 2.2.3 we will look at moments of the intensity, the RTE, and how these yield valuable relations.

2.2.2 Opacity and local thermal equilibrium

Many practical applications use instead the specific opacity, κ_ν, which is related to the mass density of the transport medium by the relation

$$\alpha_\nu = \rho\kappa_\nu \tag{2.31}$$

These opacities are tabulated by groups such as LANL's SESAME [56], calculated alongside an EOS, or by LANL's TOPS code [70] and are typically accessed by state variables such as the temperatures and densities of the plasma, i.e $\kappa(\rho, T)$.

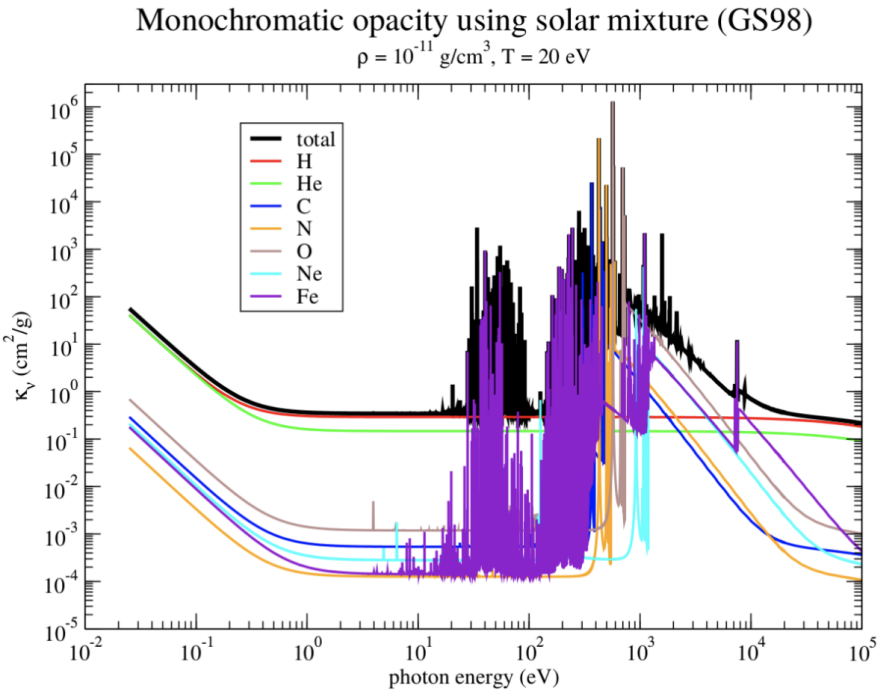

Figure 2.5: An example of solar opacities for the 10 most abundant elements in the solar mixture.

An example of the specific opacity for a solar mixture [71] with $\rho = 1 \times 10^{-11}\,\mathrm{g\,cm^{-3}}$ and material temperature of $T = 20$ eV is shown in Figure 2.5. At this condition the hydrogen can be treated as fully ionized but the other elements in the mixture are partially ionized. Shown are the top 10 most abundant elements in the mixture. Clearly visible are the cold absoprtion opacities at low temperatures, then the strong lines in the 10-100 eV range, with bremsstrahlung dominating the higher energy spectrum. As a final note on solar opacity relevant to the cosmological KHI research presented in this work, we will

encounter a cooling rate Λ, which describes how power is radiated away from an optically thin plasma and it is related to the absoprtion opacity of the plasma via $\kappa = n_e n_i \Lambda/(2\sigma T^4)$, where n_e and n_i are the electron and ion number densities, respectively. Finally, in typical HEDP settings, opacity is insensitive to change in density but strongly dependent on temperature, and consequently the ionization state of the material. For further information on the sources of opacity, I refer the reader to [72].

Many practical studies in HEDP physics where radiation is involved relies on the assumption of local thermal equillibrium. Often an ill-defined term when used in literature, here it refers specifically to a condition where the the energy level distributions of the electrons are Maxwellian (following a Maxwell-Boltzmann distribution) or alternatively the ionization states are described by Saha-Boltzmann statistics; local because we assume this is true on an appropriate local scale length relevant to the problem [1, 73]. However, it is still common in HEDP studies where we may encounter highly non-thermal conditions (e.g. laser-plasma interaction in a hohlraum) and those that are highly collisional and plasmas are rapidly thermalized (e.g. shock heating). We can solve the system with both assumptions, generally due to the locality of the these conditions.

First, under the assumption of LTE, the emission of a plasma is blackbody emission described by Planck's Law. Sometimes called the spectral thermal radiation intensity, Planck's law is a measure of the amount of radiation power per frequency emitted by a blackbody through its surface, measured at a given angle to that surface. This law is often expressed as

$$B_\nu(T) = \frac{2h\nu^3}{c^3} \frac{1}{\exp\left(\frac{h\nu}{kT}\right) - 1} \tag{2.32}$$

A classic result from thermodynamics is integrating Plancks' law over frequency. The result yields the energy density of a blackbody

$$E_R = \frac{4}{c}\sigma T^4 = aT^4, \tag{2.33}$$

where a is called the radiation constant, approximately equal to $137\,\mathrm{erg\,cm^{-3}\,eV^{-4}}$.

Second, by the laws of thermodynamics, a Planckian surface in contact with another Planckian surface at the same temperature implies that it cannot raise the temperature of the second material. Referring back to Equations 2.25 and 2.26, the materials must absorb (gain energy) via αB_v and emit (lose energy) j_v at the same rate according to Kirchoff's

law:

$$j_\nu = \alpha_\nu B_\nu. \tag{2.34}$$

These assumptions are practical for many HEDP systems and in the treatment of opacities. We refer to conditions significantly deviating from LTE, as non-LTE or nLTE, and discuss them briefly in the research portions of the thesis. However, for the remainder of the theory it can be assumed that LTE is also assumed.

2.2.3 Coupling radiation to matter with radiation hydrodynamics

While there are many scenarios in which we need only to solve the radiative transfer equation of Eq. 2.30, these solutions are still only relevant in systems where the interplay of radiation and matter is negligible. Thus our primary task in assembling a set of equations for radiation hydrodynamics is to simplify the radiative transfer equation to make it more easily integrated into the Euler equations. In this section, we motivate only the most basic forms, and briefly discuss more advanced alternatives, as this is a highly detailed and intricate topic using [1] as the primary reference. First, we define a few key relations and look at some relevant moments of the spectral intensity.

The spectral radiation energy density is the energy per unit volume, per unit frequency of the photons and is found by integrating the spectral intensity and dividing by group velocity of the photons, appropriately assumed to be the speed of light.

$$E_\nu = \frac{1}{c}\int_{4\pi} I_\nu d\Omega \tag{2.35}$$

We note that this is almost a direct reworking of Eq. 2.23 but some authors provide a more insightful derivation, e.g [68]. The spectral radiation flux, is the first moment in solid angle of the specific intensity, in the direction of propagation $\mathbf{n}$:

$$\mathbf{F}_\nu = \int_{4\pi} I_\nu \mathbf{n} d\Omega \tag{2.36}$$

The final moment needed is the spectral radiation pressure tensor, which is the second moment in solid angle in the direction $\mathbf{n}$:

$$\mathbf{P}_\nu = \frac{1}{c}\int_{4\pi} I_\nu \mathbf{n}\mathbf{n} d\Omega \tag{2.37}$$

Exactly solving these equations for a system depend on the geometries and orientations

of the rays. For example, spherical geometry has the familiar $d\Omega = \sin\theta d\theta d\phi$ but the direction of ray travel $\mathbf{n}$ may have much more complicated dependence. The higher moments in radiation fluxes and pressures can be further simplified by assuming a number of symmetries. One common assumption is that we can orient our view along the $\hat{z}$ axis, so that the area element is about the polar angle, and therefore $\mathbf{n} \cdot d\mathbf{A} = \cos\theta dA = \mu dA$. We will use this to derive Eddington's approximation for a scalar radiation pressure, greatly simplifying our cause. Under these approximations the spectral radiation flux reduces as

$$F_\nu = \int_{4\pi} I_\nu \mathbf{n} d\Omega = 2\pi \int_{-1}^{1} I_\nu \mu d\mu. \tag{2.38}$$

While it is a bit more complicated to see, for an isotropic radiation field, the pressure tensor is diagonal (consider a unit volume; if pressure is exerting equally in all directions, only the pressure against the faces are unique as there is no internal stress). Since the pressure is equal everwhere, there is only one pressure term to consider and it is a third of the total pressure (three diagonals). Thus we can derive the scalar radiation pressure as

$$p_\nu = \frac{2\pi}{c} \int_{-1}^{1} I_\nu \mu d\mu = \frac{E_\nu}{3} \tag{2.39}$$

This result can be generalized further to $p_\nu = f_\nu E\nu$, where f_ν is called the Eddington factor [1]. We can now begin to assemble the radiation hydrodynamics equations with each of the contributions of radiation pressure, flux (as a new energy source), and radiation energy density. We assume that the system is non-relativistic. In a straightforward manner, the pressures simply add in a radiation-coupled system so that $p_T = p + p_R$, where p_R is the radiation pressure, and similarly the energy densities add, $\rho\epsilon_T = \rho\epsilon + E_R$. For now we use the subscript R to denote radiation, as at the moment not necessary to indicate specific flux (integrated over all angles) or radiant flux (integrated over all frequencies).

The continuity equation does not change (sensibly; no new contributions to density or mass flux), but the remaining Euler equations are modified by substitution of these new pressures and energy densities, as well as the introduction of the new source of energy flux $-\boldsymbol{\nabla} \cdot F_R$. Explicitly these equations become [1]

$$\rho \left(\frac{\partial \mathbf{u}}{\partial t} + \mathbf{u} \cdot \boldsymbol{\nabla} \cdot \mathbf{u} \right) = -\boldsymbol{\nabla} \left(p + p_R \right) \tag{2.40}$$

$$\frac{\partial}{\partial t} \left(\rho\epsilon + \rho u^2 + E_r \right) + \boldsymbol{\nabla} \cdot \left[\rho \mathbf{u} \left(\epsilon + \frac{u^2}{2} \right) + (E_r + p + p_r)\mathbf{u} \right] = -\boldsymbol{\nabla} \cdot F_R \tag{2.41}$$

Along with the unmodified continuity equation, these equations are the cornerstone to many applications modeling radiation hydrodynamics.

A few final comments. First, the remaining consideration is how to handing the new flux term in the energy equation $-\boldsymbol{\nabla} \cdot \mathbf{F}_R$. Generally, there are three approaches, whether the system is optically thin, optically thick (diffusion approximation), or where a radiation flow may exist across thin and thick (transport regime). These terms, optically thin and thick, refer to the number of mean free paths a photon can take λ_ν over some characteristic length scale L, and is represented by the optical depth:

$$\tau_\nu = \frac{L}{\lambda_\nu} = \rho \kappa_\nu L \tag{2.42}$$

A system is optically thin if $\tau \ll 1$ (very high mean free path, photons unlikely to interact) and optically thick if $\tau \gg 1$ (photons interact readily during traversal, many times across the system). Typically to get a sense of what the appropriate optical depth for a system is, we must define L so that the physical process under consideration (i.e. instability growth, shock heating rate, etc) is well-defined, and we use a mean opacity $\bar{\kappa}$ such as the Rosseland mean opacity, at a representative density ρ (and typically temperature T). When integrating ray paths for solution of the radiative transfer equation, for example, we step the ray according to $d\tau_\nu = \rho \kappa_\nu ds$. This allows the RTE to be completely recast in terms of optical depth increments $d\tau_\nu$ instead of ray path increments ds.

Since HEDP systems deal with systems ranging from very thin to very thick, it is important to use the correct flux scheme. To briefly motivate the flux term in the diffusion approximation, which is a foundational result for many HEDP and astrophysical systems, we consider Eq. 2.30. Assuming scattering is negligible and a scalar radiation pressure as before, the first moment of the transport equation is

$$\frac{1}{c^2}\frac{\partial \mathbf{F}_v}{\partial t} + \boldsymbol{\nabla} p_\nu = \frac{1}{c}\int_{4\pi} (j_v - \alpha_{a,\nu} I_\nu)\mathbf{n} d\Omega. \tag{2.43}$$

The first term immediately vanishes due to the $1/c^2$ reduction (these fluxes are only relevant in relativistic situations). Additionally, assuming an isotropic emission causes the integration over all angles to become zero. We can then write

$$\boldsymbol{\nabla} p_\nu = -\frac{\alpha_{a,\nu}}{c}\int_{4\pi} I_\nu \mathbf{n} d\Omega = -\frac{\alpha_{a,\nu}}{c}\,\mathbf{F}_\nu. \tag{2.44}$$

Since we are working in LTE conditions, we can assume that the specific radiation

energy density approaches that of a blackbody $E_\nu = \frac{4\pi}{c} B_\nu$. (Note that this is only valid if scattering is much smaller than absorption [1]!) Thus for our scalar pressure, $p_\nu = E_\nu/3 = \frac{4\pi}{3c} B_\nu$. This means that the gradient of the scalar pressure, $\boldsymbol{\nabla} p_\nu = \frac{4\pi}{3c} \frac{\partial B_\nu}{\partial T} \boldsymbol{\nabla} T$ and thus

$$\mathbf{F}_\nu = -\frac{4\pi}{3\alpha_{a,\nu}} \frac{\partial B_\nu}{\partial T} \boldsymbol{\nabla} T \rightarrow -\kappa_{rad} \boldsymbol{\nabla} T \tag{2.45}$$

Further assumptions can be made that enable the succinct diffusion like-rate κ_{rad} in the final expression of this equation. This result clearly suggests that our radiation flux is described by a diffusion law, as in Fick's law, $F = D\boldsymbol{\nabla}\phi$. This is as far as we will go here, but I close with the statement that in many HEDP systems with high-Z material, the diffusion approximation is an excellent resource [1]. Equations like 2.45 are also the starting point for many valuable and difficult analytical solutions in radiation hydrodynamics. It has a failure point at low opacities, however, flux-limited diffusion schemes such as the highly successful Levermore-Pomraining model are available [74]. The reader is referred to [33] for a more detailed discussion of these topics as well as the the other flux formulations.

There are two ways to handle the fact that there are seemingly infinite range of photon energies for each radiation term – the equations of 2.41 were left generic. Easiest is to use the "gray" approximation, in which the radiation terms are integrated over all frequencies and use a single characteristic or averaged opacity via a Planck opacity in the transport regime or a Rosseland mean opacity in the diffusion regime. Both have their uses. The second is the so-called multi-group approximation, which is a more general approach that is consistent with a variety of numerical solvers of radiation hydrodynamics. In the multi-group approximation, opacities must still be averaged as in the aforementioned manners and radiation pressures are calculated in large spanning groups of photon energy ranges. Please refer to [51] for a detailed, practical example of how this has been handled in the modern radiation hydrodynamics code, CRASH.

Finally, we note that some codes may treat absorption, emission, and scattering in special manners and that there are a number of ways to solve the transfer equation as well as the desired radiation hydrodynamics formulation. Modern approaches include radiation diffusion models, discrete ordinates, the method of spherical harmonics, and Monte Carlo methods. Chapter 11 of the reference [58] provides an excellent introduction to these approaches.

2.2.4 Radiation waves and shocks

We now look at the evolution of radiation waves and shocks, which serve as primary physical phenomenon to two of the major works in this research. Identified in the Introduction, Marshak was the first to identify a self-similar solution describing the structure of radiation waves, using the assumption that the radiation fluxes $F_r = \sigma T^4$ greatly exceed the material fluxes $F_{mat} = \rho\epsilon c_s$, so that material motion may be deemed negligible [34, 44]. Radiation pressures and energies are then insignificant contributions to the evolving state. In the original problem, a sharp boundary emitter provides a constant-temperature source into an initially cold material. The relevant, remaining equation is the reduced energy equation:

$$\rho\frac{\partial\epsilon}{\partial t} = -\boldsymbol{\nabla}\cdot\mathbf{F}_R. \tag{2.46}$$

To arrive at a more tangible expression, we use the relation for specific internal energy, Eq. 2.7, and assume that the specific heat c_V is constant. Next we can assume that the flux is of the form $F_\nu = T^n\boldsymbol{\nabla}T$, which is not dissimilar from the form derived at in Eq. 2.45. But in fact in the original work, Marshak explicitly assumed $p_\nu = aT^4/3$ and a power-law opacity, like that of Kramer's law, $\kappa \propto \rho^m T^{-n}$. The result ultimately works out to be the same as they are wholly consistent approaches, identifying a diffusion-like behavior of the radiation flow:

$$\rho c_V\frac{\partial T}{\partial t} = -\boldsymbol{\nabla}\cdot\frac{4\sigma}{3\rho\kappa}\boldsymbol{\nabla}T^4 \tag{2.47}$$

This can then be parameterized to obtain a self-similar solution, chiefly [34, 44]:

$$x_r(t) \propto \sqrt{\frac{\sigma T^4 t}{\rho^2\kappa_R\epsilon}} \tag{2.48}$$

Here κ_R is the Rosseland mean opacity, t is the time, and x_r is the position of the heat front. The fact that it evolves self-similarly means that the profile at any point in time is a scaled version of itself. In HEDP experiment, rarely can we generate a pure Marshak wave where 2.48 is directly applicable. For example, laser-irradiation processes generate much more complicated flows, in non-equilibrium conditions; waves lose energy due to wall-loss boundaries in the target; and radiation waves can be strongly-ionizing, deviating from ideal flow. Furthermore, this result is only applicable when the wave is supersonic: the speed of the radiation wave, here $\dot{x_R}$, is greater than the sound speed c_s. When the wave becomes subsonic, material fluxes are important again and shocks can readily form. The supersonic-subsonic transition is of relatively new research focus, for example, be-

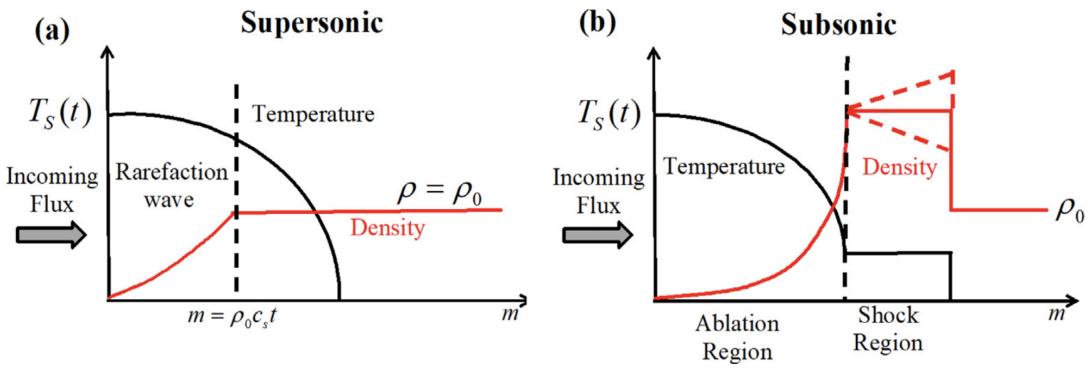

Figure 2.6: Reproduced from *Supersonic–subsonic transition region in radiative heat flow via self-similar solutions* [3]. Supersonic radiation waves (left) produce a steady, diffusing wave with a rarefaction wave evolving at a critical interface. Subsonic radiation waves (right) occur when material fluxes become important and material piles at the front of the wave, eventually forming a shock.

ing a central component of the COAX experiment as discussed later in this thesis [5, 47]. The examples of supersonic and subsonic flow, with temperatures and density profiles are shown in Figure 2.6 [3].

While this result is the first analytical solution available for testing radiation hydrodynamic codes against, the problem has since undergone intense development to account for real-world study of radiation waves. The review of such a topic is provided in [75], but some examples of modern development are the inclusion of radiative losses due to wall heating [76], a full-description of the subsonic radiation flow, including the rarefaction wave [77], and recently a solution capturing the supersonic-to-subsonic transition [3].

Radiative shocks can exist in a variety of conditions [49], chiefly dependent on the optical depth of the medium. I briefly focus on radiation-dominated shocks (optically thick shocks in an optically thick medium) and radiatively-driven shocks (thick-thin transitioning shocks). First, radiation-dominated shocks can be treated as a polytropic fluid with $\gamma = 4/3$. This means that the conventional Euler equations and strong-shock relations of Eq. 2.20 are appropriate for modeling their evolution and interaction with matter. For initially thick shocks approaching an optically thin material, the radiation can quickly become decoupled from the shock and leak forward [64]. The radiation leading the shock can heat the material ahead, completely altering the flow. In such a case, the strong-shock limit is too simplified. A fraction f_s of the initial energy injected into the shock ($\sim aT^4$) can be comparable to the kinetic energy of the shock so that the pressure of the shock may be

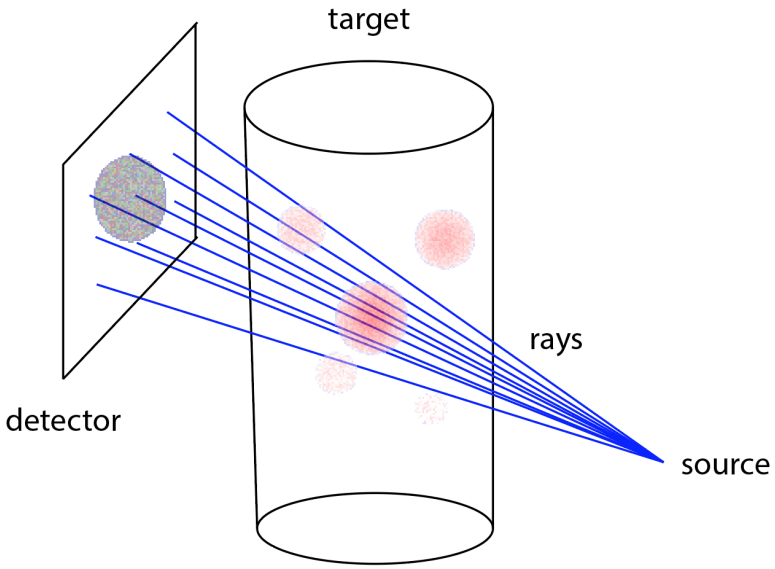

Figure 2.7: A simplified diagram showing an intense source generating rays (such as a pinhole backlighter) that traverse through and interact with a target, finally to be tallied on a detector plane (such as a CCD or an imaging film). Radiography and spectroscopy operate on this basic idea.

described more suitably by

$$p_{\text{shock}} = \frac{\gamma + 1}{2}\rho v^2 + f_s a T_{in}^4 \tag{2.49}$$

This is the case for supernova shocks experiencing shock-breakout [64], but is also relevant in thick-thin transitioning, sufficiently hot, radiation driven shocks.

2.2.5 Modeling radiative transfer for synthetic diagnostics

Finally, we discuss using the radiative transfer equation to model synthetic diagnostics in experiments, namely radiography, spectroscopy, and hohlraum flux measurments. Each of these diagnostics operates on a similar principle. In radiography and spectroscopy, we use a backlighter to illuminate a target with radiation of particular frequencies and distributions. An imager, such as a coupled-charge device (CCD) or photosensitive film, then detects the signal after it has passed through the target. The hohlraum flux measurment needs no backlighter, as it just temporally detects the radiation flux (exitance) leaving the hohlraum during the experiment. Figure 2.7 shows a generic setup for these types of diagnostics, which is fundamentally how they are modeled with synthetic diagnostics as well.

To model radiography and spectroscopy, we consider how the radiation may be interacting with the target. We begin with radiative transfer equation defined in terms of optical depth τ and the source function S_ν

$$\frac{\mathrm{d}I_\nu}{\mathrm{d}\tau_\nu} = -I_\nu + S_\nu \tag{2.50}$$

The formal solution to this form of transfer equation is [32]

$$I_\nu = I_{\nu,0}e^{-\tau_\nu} + \int_0^{\tau_\nu} e^{-\tau_\nu - \tau'_\nu} S_\nu(\tau'_\nu) d\tau'_\nu \tag{2.51}$$

However, in the event of a constant source can be reduced to

$$I_\nu = I_{\nu,0}e^{-\tau_\nu} + S_\nu(1 - e^{-\tau_\nu}) \tag{2.52}$$

By itself, the first term in the right-hand side of 2.52 is sufficient in producing conventional radiography and absoprtion spectroscopy. It states simply that the absorption is the only energy mechanism and that it depends only on the total integrated optical depth. This is by design, as we want to limit the transform of the signal as much as possible. This means we need only to trace rays through the computational grid, tallying cells of density ρ, absorption opacity $\kappa_a(\rho, T)$, and end-to-end ray path length through the cell ds. This does not account for the numerous sources of error, which include tilt, non-uniform backlighter sources, continuum removal, and a host of other uncertainties which must be integrated into the solver. Such a discussion is provided in the thesis research, e.g. [47].

The situation becomes more challenging for spectroscopy when scattering and self-emission are important contributors to changes in the measurable intensity. This is often the case of astrophysics as we showed in [64] in research on supernova shock-breakout in inhomogenous winds as exploratory work related to this thesis. In the HEDP experiments of this thesis, self-emission is typically negligible and we can assume scattering contributions are minimal, with scattered radiation ultimately lost into the target. We briefly motivate the case for which self-emission is important (typically in low-density, hot plasmas). If we assume Kirchhoff's Law of detailed balance then we can then recast the transfer equation as

$$\frac{\mathrm{d}I_\nu}{\mathrm{d}\tau_\nu} = -I_\nu + B_\nu. \tag{2.53}$$

For sufficiently large optical depth, $\tau \to \infty$, the solution for a constant thermal source

becomes

$$I_\nu = B_\nu. \tag{2.54}$$

However, for sufficiently optically thin media, $\tau \to 0$, the Taylor-expansion to first order yields

$$I_\nu = I_{\nu,0}(1-\tau) + B_\nu \tau_\nu \tag{2.55}$$

With this result, we have a new template for a discretized solution to spectroscopy with absorption and self-emission contributions. This is essentially the basis for studying certain types of supernova light-curves [78]. A second byproduct of this exploration is that indeed in the limit of high optical depth, a true blackbody exhibits only surface emission, while for thin bodies, emission is volumetric.

Finally, to model hohlraum fluxes, we typically need a full radiative transfer equation with nLTE opacities for the most accurate calculations. Most advanced codes already modeling laser drives are capable of providing this information. However, a useful estimate of the flux is to simply assume that the exitance is determined by the bulk radiation temperature inside the hohlraum, T_r, having a blackbody flux

$$\frac{F}{A_{\text{detector}}} = \sigma T_r^4 \cos\theta_{\text{detector}} \tag{2.56}$$

where A_{detector} and θ_{detector} are the area and orientation angle of the detector, respectively. Note this assumes that the angular distribution of the radiation intensity follows Lambert's Law, where $I_\nu \propto \cos\theta$. Thus such an approximation assumes a hohlraum flux surface (hohlraum exit hole) that is Lambertian and necessarily Planckian; neither are generally appropriate, but Eq. 2.56 suffices for a basic estimate.

CHAPTER 3

An Experiment Modeling the Role of the Kelvin-Helmholtz Instability on Galactic Filaments Feeding Galactic Halos

3.1 Introduction

The star formation rate in galaxies, that sets their mass and color, is regulated by the availability of gas within the galaxy. The amount of gas within the galaxy depends on the accretion rate for gas from the halos that surround them. Therefore, the hydrodynamic and thermodynamic conditions in the halos, and the rate at which gas is channelled into galaxies, is key to understanding galaxy formation and evolution. The idealized picture of galaxy formation is that gas and dark matter spherically condense due to their own self gravity, and eventually establish a dark matter halo and a gaseous halo. For the gas, an accretion shock thermalizes the infalling gas. Behind the shock, the gas is almost hydrostatic, having converted its gravitational energy into kinetic, and finally into thermal energy at the shock. According to the virial theorem, the thermal component should roughly equal (up to a minus sign) half of the gravitational potential energy [79, 80, 81]. For halos comparable to the Milky-way's halo ($M_v \sim 10^{12} M_\odot$) the corresponding virial temperature is $T_v \sim 10^6$ K. This picture holds as long as the radiative cooling is inefficient. Then, a virial shock quickly extends to the edge (the "virial radius") of the halo. This condition is satisfied as long as the compression rate of the gas below the virial shock is faster than the cooling rate, which requires that the halo mass be larger than a critical mass of $M_{shock} \sim 10^{12} M_\odot$ [82]. Gas infalling into halos below the critical mass is not expected to shock until it reaches the central galaxy. At low redshifts ($z \lesssim 1.5$, corresponding to around 9 Gyrs ago) the transition around this critical mass is abrupt. This theoretical prediction is key to explain observed trends in low redshifts galaxies, particularly the bi-modality and sharp transition between smaller, blue (ie star-forming) galaxies, and larger red (non-star

forming) galaxies [83, 84]. When a hot halo forms, additional feedback processes, particularly active galactic nuclei (AGN) from the supermassive black holes at the centers of galaxies, can further halt gas accretion onto galaxies.

However, theory of the cosmic web [85] and large, N-body cosmological simulations [86, 87, 88] imply that at higher redshifts ($z \gtrsim 1.5$), the infall onto halos around the critical mass scale is increasingly non-spherical, with the majority of the gas fed through narrow filaments that form the cosmic web. Some recent observations argue that such cold streams have been observed [89, 90]. Since the cooling rate scales as the density squared, a mixed state, for which gas in the filaments free-falls inwards while the gas in-between filaments shocks and stops at the virial radius, occurs [91]. This corresponds to cold filaments, infalling supersonically through hot, hydrostatic and diffuse medium. For masses just above the critical mass, these cold, dense streams are able to penetrate the hot circumgalactic medium (CGM) and deliver cold gas deep inside the halo, where it can be used to fuel galactic growth and form stars [91, 88]. At redshift $z \gtrsim 2$ these filaments are on order of $1 - 10\%$ of the virial radius $R_v \sim 100$ kpc in width, and are several orders of magnitude colder and denser than the CGM, reaching a temperature of $T_s \gtrsim 10^4$ K and density $\rho_s \sim 10 - 100\rho_b$, where subscripts s and b denote the filament/stream and background, respectively. These filaments are potentially able to resist the formation of a virial shock inside the filament due to much faster cooling rates [92]. Without such a shock they may stay cold and collimated, providing substantial mass flow rates necessary for high star formation rates [88].

Simulations resolving cold streams are only able to capture the large-scale structures and properties of the halo and filaments, such as radii, mean densities, and flow velocities. At finite resolutions of 100 pc, such as those of [93], these simulations are unable to capture any small-scale features including the hydrodynamics at the boundary of the filament, the precise nature of a galactic boundary, and may not preclude the coexistence of a shock somewhere near or inside the virial radius. Particularly unclear is the nature of a possible late shock emerging around $z \gtrsim 2$ in halos transitioning to above the critical mass. Some grid based codes observe fragmentation of the stream around $\sim 0.3R_v$ [94, 95, 96]. Springel et al. 2010 and Vogelsberger et al. 2012 found that filaments heat to roughly the virial temperature around $\sim 0.25 - 0.5R_v$. Additionally, modern Smooth-Particle-Hydrodynamics (SPH) codes that produce the bulk of galaxy formation studies tend to smooth out such accretion related shocks. [97] argued that SPH codes showing that streams remain cold and coherent were largely caused by numerical error inherent to SPH.

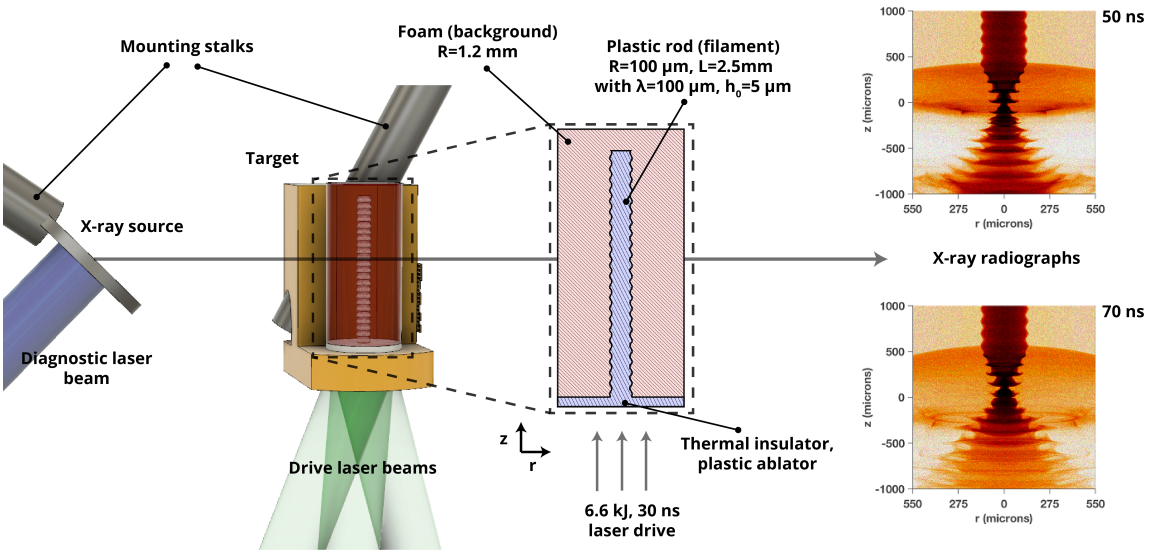

Figure 3.1: Current experimental design and sample simulated radiographs. From left to right in the figure, first the target is shown in Omega EP pointing geometry. Three laser beams deliver 6.6 kJ in 30 ns to the dense plastic of the cylindrical target, with a fourth beam driving a backlighter for x-ray radiography. The expanded view shows a cross-section of the part of the target in which the dynamics of interest occurs. On the far right are shown some sample radiographs at 50 and 70 ns into the experiment.

Some simulations show these streams maintain constant velocity from well outside the virial radius to deep within the halo, despite gravitational free-fall [88]. This suggests there is a dissipative process to shed off energy through the gain in gravitation potential. Despite possible means of emission that reveal loss of gravitational energy, the exact process is unclear, but may be in part due to hydrodynamic instability forming from large shear velocities at the filament edge. With the context of a cold, dense column of gas flowing through a hot, diffuse background, this shear flow may be subject to the Kelvin-Helmholtz instability (KHI), in which the velocity gradient across the interface of two fluids develops into vortical structures that greatly enhance mixing between the fluids.

Until recently [98, 99, 100] the hydrodynamics of this cosmological process had not been considered in depth. In the study presented by [99], the KHI on the filament edge was considered in a simple numerical and analytical analysis, assuming no virial shock, and that the stream and background are in pressure equilibrium. They showed, that under relevant conditions, KHI might grow fast enough so the filament shape is dominantly controlled by its growth. However, if the background pressure exceeds the material pressure inside the filament, a shock will be driven into the stream [101]. This shock has the potential to

drastically alter the evolution of KHI, diminish the filament mass areal flux, and shut off cold matter deposition into the galaxy, potentially marking a possible transition between a cold stream embedded in hot media to purely hot mode accretion dominated by virial shock heating. The lack in simulation capabilities to resolve the small scale physics of these filamentary processes motivates our pursuit of a well scaled experiment, that might shed light on the matter. Furthermore, this platform experimentally provides an upper, idealized limit to the effect of the KHI, which can be scaled to the astrophysical case. We note that the while asymmetry in the galaxy formation, filament orientation and shape, and virial shock are expected, we assume that the net structure of the shock is spherical and the filaments are columnar and oriented radially. Where the filament is expected to meet the shock at the virial radius, the shock is locally approximately planar and tangential to the infall direction of the filament. This provides a potential best-case scenario for KH growth. Finally, we note that small scale mixing on the filament edge, supposedly created due to energy transfer to small scales was not analyzed.

In this chapter we present a preliminary design (shown in Fig. 3.1) of a high energy density laboratory experiment to emulate and study the cosmological process of a cold stream penetrating a shocked region within the galactic halo, collapse of the filament, and subsequent KHI evolution on the deflected interface of the shocked filament. Our design builds upon previous work by [102], which presented a way to study planar KHI in the compressible regime – the target presented here is essentially a cylindrical version of their Omega EP target utilizing a more powerful driven shock. The design of [102] was motivated by earlier experiments to study shear flow under HED conditions using X-ray radiography [103, 104]. The Omega laser facility has been successfully used to study the KH instability for a variety of configurations [105, 104, 106, 107, 108], however this is the first that is capable of informing supersonic KHI on a cylindrical platform and is directly applicable to the study of cold streams. Section 2 discusses this platform along with the primary physics involved. We follow the work of [98, 99, 100] to establish the parameter space for halos of $M \sim 10^{12} M_{\odot}$ around $z \sim 2$. We develop the physical description of the flow and present hydrodynamic simulations of the experiment using the CRASH radiation hydrocode [51]. The scaling analysis necessary to determine a regime of applicability to the astrophysical process then follows. We identify an astrophysical regime in which KH significantly alters the length where the filament converges about axis, thereby shock heating the cold filamentary material before it can reach the disk. This is highlighted in Section 3. We finally address the implications and limitations of our model, with discussion on the radiative regime and future work in Section 4.

3.2 Experimental design and the physics of filament collapse

The primary assumption in our experimental design is that a columnar gaseous filament flows through the hot, shock-heated CGM and terminates in the galactic disk. High background pressures in the CGM are expected to exceed material pressure in the filament and thus drive a shock into the filament. We mimic this idealized process, using a cylindrical target designed for the Omega EP laser, wherein a laser driven shock causes a cylindrical plastic 'filament' (rod) to flow through a shock-heated foam 'background'. The main diagnostic to be used in the experiment is X-ray radiography, which is capable of capturing an instance of this process, allowing a proper analysis of the rod edge. Fig. 3.1 shows the current experimental design and setup, in addition to sample simulated radiographs of the experiment.

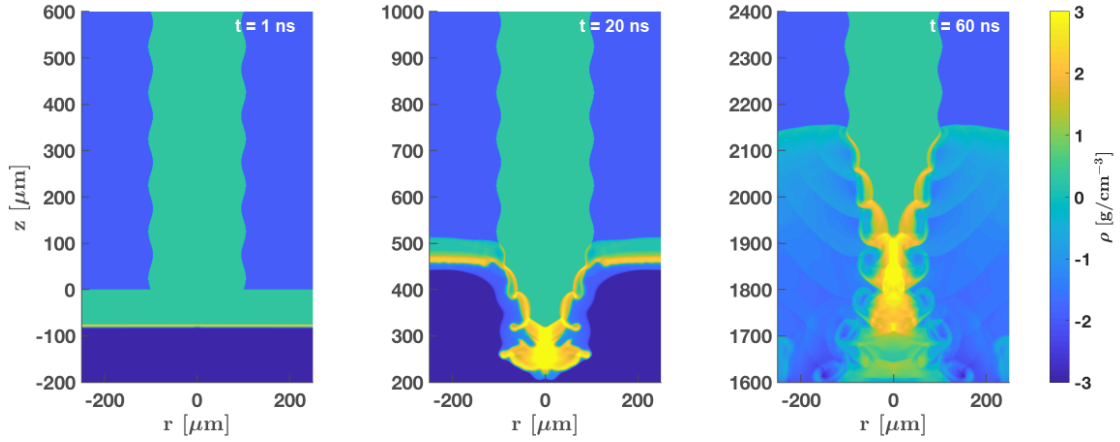

Figure 3.2: A pseudocolor plot showing the $\log_{10}$ density of a CRASH simulation of the experimental system at three times during its evolution. (Left) The initial configuration at 1ns of laser drive. (Middle) 20ns into the drive, the filament has collapsed and begins to reflect axially. The incident and transmitted shocks are evident. (Right) The drive is in a desired configuration of the quasi-steady dynamics 30ns after the laser drive has ended (60 ns total). The shock reflections are visible in the foam due to interactions with the perturbed interface in addition to shock structure in the shocked filament. The apparent shock curvature is largely the consequence of laser energy deposition and not intended to replicate curvature in the astrophysical case.

In the following discussions, variables with the subscripts s and b will denote stream/filament (plastic rod experimental equivalent) and background (foam equivalent) quantities, respectively. Furthermore, when the two systems are discussed together, state variables with a superscript $*$ will be used for experimental quanitites, where those without will be used

for astrophysical quantities. The proposed target begins with a thin 50 μm plastic layer to which a 50 μm plastic thermal insulator and narrow rod assembly are attached. The rod assembly contains the physics package of the experimental platform. Single-wavelength $\lambda = 100$ μm sinusoidal perturbations of amplitude $h_0 = 5$ μm are machined on the plastic rod of diameter $d = 200$ μm to seed the KH instability (KHI). This specific initial wavelength was chosen considering the experimental time and length scale, and is relevant to the scaling to the astrophysical system, discussed further below. A foam cylinder surrounds the plastic rod and is attached to the thermal insulator. The entire target is 2.6 mm in length and 1.2 mm in diameter.

The plastic layer, thermal insulator, and rod are identical in density (stream density $\rho_s = 1.4\ \mathrm{g\,cm^{-3}}$) and polycarbonate material. The thermal insulator and rod contains a trace iodine dopant, but we consider all the plastics to be hydrodynamically equivalent. The dopant is optically thick to x-rays: in the thermal insulator it serves to prevent unwanted radiative pre-heat from the laser pulse; in the rod it provides a sharp imaging contrast for x-ray radiography. The shell is a CH foam with a density of $\rho_b = 0.14\ \mathrm{g\,cm^{-3}}$, placing our base density contrast at $\delta = \rho_s/\rho_b = 10$. This choice in contrast is again directly relevant to the ranges of density contrasts in the astrophysical case. Furthermore, a contrast of roughly 28 is accessible by dropping the foam density to ~ 50 of $\mathrm{mg\,cm^{-3}}$.

As mentioned, the experiment is designed for Omega-EP, which can provide up to a 30 ns long laser pulse delivering up to a total 6.6 kJ incident directly onto the plastic surface in a spot size of 1100 μm. Specifically for our design, Omega-EP will stitch three 351 nm wavelength, $10\,\mathrm{ns}$ pulses of 2.2 kJ each to assemble the primary laser drive and use the fourth beam for the x-ray radiography diagnostic. The primary laser spot is spatially supergaussian (order 8), yielding an approximately flat-top shape. The duration of the experiment is roughly $\tau_{exp} \sim 100100\,\mathrm{ns}$, and depending on the drive duration or energy delivered, diagnostics begin after $\sim 30\,\mathrm{ns}$ of drive. Edge effects, such as inward propagating wall shocks caused by the unevenly heated plastic, are negligible as they arise on a timescale proportional to the foam thickness times the sound speed in the foam, which is $\sim 2 - 10\ \tau_{exp}$. Propagating wall shocks induced by this blow-off plastic plasma and other edge effects may be partially prevented or mitigated by using a beryllium shock tube casing, as will be considered in future experiments if needed.

3.2.1 Deflection of the background-filament interface

Fig. 3.2 shows the density structure as predicted by a two-dimensional CRASH simulation in cylindrical, rz geometry at several times. CRASH is an Eulerian, radiation hydrodynamics code, designed to simulate laser experiments and high-energy density systems. The long pulse laser is initialized at $t = 0$ns. The pulse drives a shock which proceeds from bottom to top, into the plastic. After 1 ns, the shock progresses through the plastic layer. The shock continues to propagate through the plastic, crossing the thermal insulator interface at $t \sim 5$ ns. By $20\,\mathrm{ns}$, the shock has long exited the dense plastic, propagating through the physical package, while transmitting an oblique shock into the plastic rod. The filament collapses inwards, since the shock travels faster in the foam, compared to the rod. Note that the filament collapse converges cylindrically about axis. The shock reflects about the axis, causing the filament to reflect cylindrically back outward into the shocked material downstream. The perturbations on the deflected foam-filament interface grow continuously throughout the collapse and reflection. This is well evident by $60\,\mathrm{ns}$ (right panel).

Two shocks are present: the incident, nearly planar shock in the background foam and the transmitted shock in the filament. Following the analysis of [102] we can fully describe the post-shock flow behind the incident shock as a function of the incident shock velocity U and the initial state: the densities of the unshocked background and filament (or their contrast ratio δ), their initial pressures, and the adiabatic indexes γ in each material. This planar analysis is suitable for describing the bulk post-shock flow but becomes inaccurate near the axis where radial compression is considerable. U is taken radially away from the initial interface where the shock appears planar (e.g. roughly 200 $\mu\mathrm{m}$), assumed to be the effective free-streaming limit of the incident shock. In the analysis the CRASH simulations employ both the ideal $\gamma = 5/3$ and the values of γ from equation of state tables created by the PROPACEOS software [109].

In the stationary shock frame, the experimental flow is analogous to the proposed astrophysical case: a dense cylindrical filament flows into the virial boundary of the galaxy under gravitational force, high pressures drive a shock into the filament, the filament collapses, and along with the dissipative KH instability it disperses its matter into the galactic environment (visualized from the simulation of the experimental system in the right panel of Fig. 3.2). Fig. 3.3 idealizes the flow geometry of the stationary incident shock frame, labeled $S1$.

Transforming to this frame, the Euler balance equations for the case of an oblique

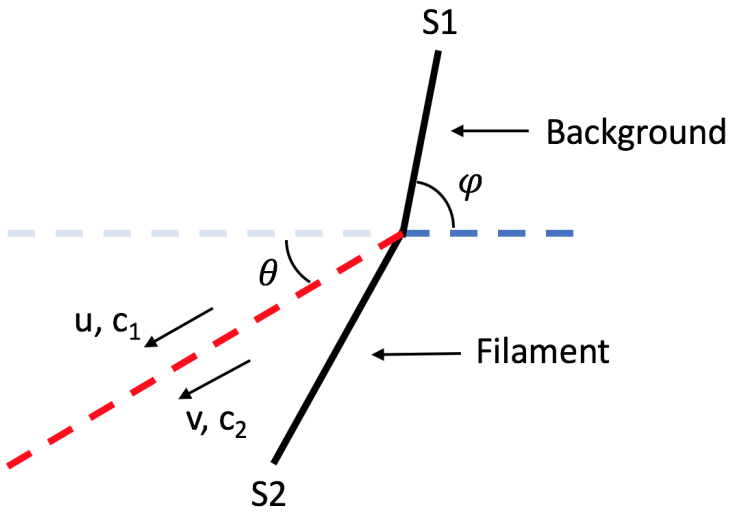

Figure 3.3: Idealized flow geometry in the stationary shock frame. A background and filament flow into incident shock S1 and transmitted shock S2, respectively. The dashed line indicates the interface between materials, red denoting the deflected interface.

shock can be solved to determine the flow field properties. On the key assumption that there is pressure equilibrium on the deflected interface, these equations for planar flows in rectangular geometry take the form, [102]

$$\rho_0 U \sin\phi = \rho_1 u_1 \sin(\phi - \theta), \tag{3.1}$$

$$p_0 + \rho_0 U^2 \sin\phi = p_1 + \rho_1 u_1^2 \sin(\phi - \theta), \tag{3.2}$$

$$\rho_0 \tan\phi = \rho_1 \tan(\phi - \theta), \tag{3.3}$$

$$\epsilon_0 + \frac{p_0}{\rho_0} + \frac{U}{2}\sin\phi = \epsilon_1 + \frac{p_1}{\rho_1} + \frac{u_1^2}{2}\sin(\phi - \theta). \tag{3.4}$$

In this frame, the flow with initial density ρ_0, pressure p_0, and specific energy ϵ_0 (respective to each material) is seen to enter from right to left through oblique shocks at angles ϕ for the background and $\phi - \theta$ for the filament. Both materials travel with an initial velocity U. Each of the shocked flows then has velocities parallel to the deflected interface (red dashed line), labeled u and v as in Fig. 3.3, respectively for the shocked background and filament. The velocity difference $\Delta u = |u - v|$ defines the shear velocity at the interface, corresponding to KH evolution. In solving (3.1)-(4) simultaneously for each material, where the shocked velocity variable u_1 is u for the background or v for the filament, a theoretical estimate for the growth rate may be obtained.

3.2.2 Subsonic, compressible KH evolution on the deflected interface

For the following discussion we assume negligible surface tension and viscosity. For incompressible flow, a perturbation on the interface having a small amplitude to wavelength ratio (i.e. $\lambda >> h$) will exponentiate at the rate

$$\gamma_{ic} = \frac{k\Delta u}{2}\sqrt{1-A^2}. \tag{3.5}$$

where $k = 2\pi/\lambda$ is the wavenumber, $\Delta u = |u - v|$ is the difference in shear speeds in each material parallel to the interface, and $A = (\rho_2 - \rho_1)/(\rho_2 + \rho_1) = (\delta - 1)/(\delta + 1)$ is the Atwood number [1]. In the so-called linear regime, the perturbation will grow exponentially, according to $h \sim h_0 \exp(\gamma_{ic} t)$; this occurs until approximately $h/\lambda \sim 0.1$.

However, for the compressible case in the limit of $A \to 0$ the KHI will evolve with a rate

$$\gamma_c = -i\gamma_{ic}\frac{\sqrt{-1 - M_c^2 + \sqrt{1 + 4M_c^2}}}{M_c}, \tag{3.6}$$

where M_c is defined as the convective Mach number, or $M_c = \Delta u/(c_1 + c_2)$ [110, 102]. Here c_1 and c_2 are the sound speeds in the shocked materials. Note in the reference frame of one of the fluids being stationary, a convective Mach of $M_c = 0.5$ corresponds to the transition to supersonic flow with a Mach number $M = 1$ flow in the moving fluid. Using the model described in Section 2.1 with an ideal gas with $\gamma = 5/3$, the transition to subsonic Mach flow occurs with an incident shock of 6-7 $\mu\mathrm{m\,n^{-1}\,s}$. This will be employed as the cutoff when seeking a subsonic $M_c < 0.5$ regime later. Additionally Eq. (3.6) suggests that increasing the shear velocity has the effect of reducing the instability growth rate, stabilizing the KHI; a value of $M_c = \sqrt{2}$ yields an imaginary growth rate, theoretically stifling the instability altogether. Note, that this result was confirmed in full numerical simulations [102].

The KHI evolving on the deflected interface is assumed to evolve in the linear, subsonic, compressible regime, with a growth rate predicted by Eq. (3.6) and a corresponding timescale $\tau_{KH} = 1/\gamma_c$. However, the initial perturbation wavelength λ is compressed to λ_s, due to the oblique shock compression of the background and filament as discussed in Sec. 2.1. This shocked wavelength is approximated as [102]

$$\lambda_s \approx \lambda\frac{u_c}{U}. \tag{3.7}$$

The quantity u_c is called the convection velocity, an average speed at which a point on the interface drifts or equivalently, the net velocity at which the KH vortices convect. It can be found by assuming there exists a stagnation point between each pair of KH vortices. At these points, the fluid flow can be approximated as quasi-steady and in pressure equillibrium [111]. Applying the Bernoulli equation yields

$$\rho_1(u - u_c)^2 = \rho_2(v - u_c)^2. \tag{3.8}$$

The total time available for KH evolution at any point on the deflected interface is the time it takes that point to travel the length L of the interface, $t_{growth} \approx L/u_c$. Referring to Fig. 3.3, the deflected interface is assumed to be a straight line, extending from the point of shock continuity between oblique shocks $S1$ and $S2$ to the point where the deflected interface reflects about axis. Thus $L = R_s/\sin\theta$, where R_s is initial radius of the stream.

3.2.3 Summary of model assumptions and connection to the astrophysical case

Before making the case for hydrodynamic similarity between the experimental and astrophysical systems, here we briefly summarize the model.

- The cold stream of radius R_s in a comoving background system flows through a strong shock whose flow properties in the planar geometry assumption may be described by (3.1)-(4). The two fluids have infall velocity U and a density contrast δ. In stationary shock frame, the physics of each system will evolve similarly. Similarity will be established in Section 3.3.1 - 3.3.2 and the flow solutions discussed in Section 3.3.3.

- KH on the filament is assumed to evolve exponentially, in the linear growth regime of standard KH formulation. This is justified by the initial wavelength λ, perturbation amplitude h_0, and compressible KH dynamics quantified by M_c, discussed in Section 3.3.3

- The dynamics of the system are driven by the ram pressure $P \approx \rho_b U^2$ of the background. The shocked background maintains constant pressure. This has an important consequence in considering radiative cooling, discussed in Section 3.3.4.

- If the KH growth is prominent, it will have the effect of increasing mixing between the shocked background and filament. The KH could be capable of entraining the

entire shocked filamentary region. The conclusions in Section 3.4 will address this.

3.3 Scaling

We argue that the physical processes of the laboratory experiment described here and the idealized astrophysical picture are hydrodynamically equivalent on certain length and timescales by establishing scaling relations between the two. Namely, we seek to show the applicability of the Euler equations to the processes, that the same terms in each apply, establish Ryutov scaling between the systems, and address specific scaling of more detailed phenomenon [18]. The first two points follow simply from prior assumptions and assertions, but will be strengthened by global Reynolds, Peclet, collisionality, and similar arguments used to determine physical consistency between the two systems. Ryutov scaling will be established by identifying characteristic state parameters,

$$\tilde{u}_1\sqrt{\frac{\tilde{\rho}_1}{\tilde{P}_1}} = \tilde{u}_2\sqrt{\frac{\tilde{\rho}_2}{\tilde{P}_2}}. \tag{3.9}$$

where subscripts 1 and 2 denote characteristic velocity $\tilde{u}$, pressure $\tilde{P}$, and density $\tilde{\rho}$ of each system [18].

Parameter	Physical description	Symbol	Cold Stream	Exp. (filament)
Length scale (cm)	Filament radius	R_s	3×10^{21}	0.01
Velocity (cm/s)	(Virial) shock speed	U	2×10^{7}	3×10^{6}
Density (gpcc)	Filament density	ρ_s	10^{-26}	1.4
Temperature (eV)	Filament temperature	T_s	86	2
Eff. ionization	Avg. of plasmas	Z	2	10.3
Eff. mass number	-	A	1	0.1
Ion Density (cm^{-3})	-	n_i	0.003	1.7×10^{27}

Table 3.1: Characteristic parameters for the galactic cold stream and experiment as discussed in Section 3.3.1.

Finally, we make a case for detailed scaling beginning with the idealized system proposed by [98] and [99], then addressing the caveats of our system, to include discussions of radiation, geometrical considerations, and gravity.

3.3.1 Scaling parameter range

The astrophysical scalings can be built from parameter ranges as derived by [98] and [99], following the semi-analytical analysis of virial shocks by Dekel and Birnboim (2003) and subsequent work. We again note that in the work of [98] and [99], the assumption is that the cold stream is embedded in a stationary, hot galactic background, with *pressure equillibrium* between the stream and background. We begin by assuming the presence of a shock, behind which post-shock pressures exceeds the material pressure of the cold stream, thus driving a shock into and collapsing the filament. For the relevant astrophysical regime, i.e. an unstable galactic regime, we assume the interaction of a cylindrical filament with a planar shock for a galaxy of characteristic mass $M_{12} \sim 10^{12} M_{\odot}$ around a characteristic redshift of $z \sim 2$. Note that the assumption of a planar shock neglects the spherical geometrical effects. However, this assumption is justified considering the stream radius to virial shock radius ratio, $R_{\rm s}/R_{\rm v} \ll 1$. Also assumed is a co-moving background, infalling with the filament that contributes the high pressure post-shock background. Within this picture, no shear occurs between the filament and unshocked background.

The cosmic background plasma can be assumed to be a polytropic hydrogen gas with $\gamma = 5/3$. The virial temperature for a galaxy of this mass and redshift is given by

$$T_{\rm v} \approx 1.5 \times 10^6 \times M_{12}^{2/3} [3/(1+z)] = 1.5 \times 10^6 K \tag{3.10}$$

which is taken to be the temperature of the shocked infall [99]. The virial shock for such a characteristic galaxy is assumed to remain at the virial radius and the cold stream accretes at a roughly constant infall velocity comparable to the virial velocity $U \sim V_{\rm v}$. This is estimated from the virial theorem,

$$\frac{3}{5}\frac{GM}{R_{\rm v}} = \frac{3}{2}\frac{k_B T_{\rm v}}{m_p} = \frac{1}{2} V_{\rm v}^2, \tag{3.11}$$

yielding $U \sim 200 \ {\rm km\,s^{-1}}$. This is assumed to be the shock speed.

Since we are not considering an embedded flow, a useful physical scaling parameter here would be the upstream Mach number, defined in stationary shock frame as the speed of the shock over the sound speed in the upstream (unshocked) material $M_b = U/c_{\rm s}$. Simulations suggest that the streams may have densities $\rho_s = 10^{-26}$ to 10^{-27} ${\rm g\,cm^{-3}}$ and temperatures of $T_s = 10^4$ K and the background material $\rho_b = 10^{-27}$ to 10^{-28} ${\rm g\,cm^{-3}}$. This is further supported by the derived density contrast range of $\delta = 10 - 100$ by [98]. For

the model here, we assume $\delta = 10$ with $\rho_b = 10^{-27}\,\mathrm{g\,cm^{-3}}$ and $\rho_s = \delta\rho_b$. However, if we the consider the unshocked, comoving background material to be on order of stream temperature $T_s = 10^4$ K, then the sound speeds on order of $20\,\mathrm{km\,s^{-1}}$ suggest strong accretion shocks at $M_b \sim 10$ for the background. This justifies use of the strong-shock conditions. Note in the radiative analysis of virial shocks, if a shock has receded, it is because the post-shocked material once behind it has cooled, thereby weakening the shock. Further radiation considerations are discussed in Section 3.3.4.

Parameter	Symbol	Cold Stream	Experiment
Hydrodynamics:			
Localization	l_c/h	1.8×10^{-5}	4.9×10^{-6}
Ryutov number	$\tilde{v}\sqrt{\tilde{\rho}/\tilde{p}}$	2.2	2.3
Heat transport:			
Thermal diffusivity ($\mathrm{cm^2\,s^{-1}}$)	χ	2.4×10^{26}	5.1
Peclet number	Pe	2.5×10^3	6.0×10^3
Momentum transport:			
Thermal viscosity ($\mathrm{cm^2\,s^{-1}}$)	ν	3.2×10^{24}	4.4×10^{-2}
Reynolds number	Re	1.9×10^5	6.8×10^5
Radiation:			
Compton mfp (cm)	l_{rad}	1.3×10^{26}	41
Cooling time	$\tau_{cooling}/\tau$	2.3	-

Table 3.2: Derived scaling parameters for the galactic cold stream and experiment as described in Section 3.3.1. While the cooling time of the cold stream is relevant, in the experiment cooling is negligible.

The radius of the filament is taken as $R_s/R_v \sim 0.005 - 0.05$. [99] modifies this estimation to include cosmological inflow but we assume the simplified model presented in [98]. From [98] we also take $R_s/\lambda \gtrsim 1$. This constraint on the wavelength λ is perhaps the biggest uncertainty regarding our model assumptions, however, we choose a wavelength that yields experimental time and length scales to ensure a considerable effect of KHI as well as diagnostic capability.

3.3.2 Applicability of the Euler Equations to describe both systems

We proceed to show that the Euler equations, with negligible heat transport and viscosity, describe these systems in a similar manner.

In the experiment, initial foam and plastic densities are $\rho_b = 0.14\,\mathrm{g\,cm^{-3}}$ and $\rho_s = 1.4$ $\mathrm{g\,cm^{-3}}$. Thus, laser driven shocks on order of tens of $\mu\mathrm{m\,n^{-1}\,s}$ produce highly collisional

plasmas, having ion and electron mean free path (MFP) ranging from 10^{-2} to 10^{-6} microns. However at such sparse densities, the galactic plasma is a little more complex. The fully ionized infall at 10^4 K has ion and electron mean free paths on order of $\lambda_{mfp} \approx 10^{14} - 10^{15}$ cm, (several thousands of a parsec), and equillibrates on order of 10s of years. With the lowest length scales on order of hundreds of parsecs and millions of years, the collisional mean free path satisfies the condition $\lambda_{mfp} << L$, permitting a single fluid description of the dynamics. It is worth noting that collective plasma effects of the magnetized plasma may bring the MFP to 10^{16} cm, and the fluid approximation still holds. Only when the temperature exceeds 10^8 K, and the density drops below 10^{-28} g cm^{-3} (at the outskirts of a cluster, for example), does the fluid approximation begin to break.

However, at temperatures in excess of 10^4 K radiation emission is strong, and at such low densities the galactic matter is completely unable to entrain the photons and even more so for the post-shocked medium. The mean free paths associated with Compton scattering and Bremstrahhlung are order 10^{26} cm and greater, thus the photons can be considered free-streaming (despite a tremendously high photon viscosity). However, one must address the effect of radiative cooling, to ensure that on relevant time scales cooling effects are minimal. This is considered in Section 3.4.

At present we consider only the adiabatic case, neglecting photon viscosity. For the galactic plasma at 10^6 K assuming a Coulomb logarithm of $\ln \lambda = 24$, the kinematic viscosity is 3×10^{24} cm^2 s^{-1}. With length scales on order of the filament radius, roughly 1 kpc $\sim 3 \times 10^{21}$ cm and shock velocities 2×10^7 cm^2 s^{-1}, the corresponding Reynolds number is 10^5.

For the experiment, simulations approximate that the CHI plastic and CH foams reach average ionizations of $Z = 0.1$ at $T = 2$ eV and $Z = 0.9$ at $T = 8$ eV, with effective atomic masses $A = 10.3$ and $A = 8.3$, respectively. Taking the Coulomb logarithm to be 1 yields viscosities on order of 1 cm^2 s^{-1} for the foam and 0.04 cm^2 s^{-1} for the filament, corresponding to Reynolds numbers of roughly 7×10^5 and 3×10^4, respectively. The characteristic length for both flow descriptions is the filament radius and the characteristic velocity is the shock (infall) speed. Note that these exceed Reynolds numbers required for shear instabilities ($Re \sim 10^3$) and turbulent mixing [112]. Furthermore, these Reynolds numbers are comparable to those of the adiabatic galactic case, and both systems satisfy that viscous effects are negligible.

(γ_1, γ_2)	R_s/λ	$U]$	$\theta[^\circ]$	$\phi[^\circ]$	Δu	M_c	$\tau_{KH}[\mathrm{s}]$	t_{growth}/τ_{KH}
(1.67, 1.67)	1	20	86	19	13.6	0.87	5.41×10^{-9}	3.76
(1.31, 1.92)	1	20	88	21	15.9	1.19	6.75×10^{-9}	3.01
(1.67, 1.67)	1	200	86	19	136	0.87	1.62×10^{14}	3.76
(1.67, 1.67)	3	200	86	19	136	0.87	3.25×10^{14}	11.27

Table 3.3: Solutions to the oblique shock equations for the idealized flow geometry. Materials with index pairs (γ_1, γ_2) for the background and filament, respectively, with an initial pressure of 10^{10} bar, and flow velocity U produce the listed values of the flow. In order, the first two lines correspond to the experimental model: first, ideal values of γ, then CRASH obtained values (taken from simulation at $t = 90$ ns) using ideal values for lower velocities U, easily obtained with lower laser drives with no significant modifications to the experiment. The following two lines correspond to the astrophysical model. Note velocities are reported in [$\mu\mathrm{m\,n^{-1}\,s}$].

Now we wish to ensure that heat transfer is dominated by convection, assessing the thermal conductivity of each system. For the astrophysical case, the thermal conductivity is $2 \times 10^{26}\ \mathrm{cm^2\,s^{-1}}$, yielding a Peclet number of 3×10^3. The plastic filament has a conductivity of $0.31\ \mathrm{cm^2\,s^{-1}}$ yielding a Peclet number of roughly 10^5. The foam being 10 times less dense is roughly 10 times more diffusive, with a Peclet number of 6×10^3. As such, the effects of thermal heat transport can be ignored.

Having determined that these systems are physically consistent, we assess the Ryutov similarity, stated in Table 3.3.1. Since both systems are shown to be strongly driven, Ryutov similary is guaranteed. We can choose either post-shock conditions to be characteristic or assume a characteristic pressure that is proportional to the fluid ram pressure $\tilde{p} \sim \tilde{\rho}\tilde{u}^2$ for this purpose. In the next section we assert that the systems are ram pressure dominated. Hydrodynamic evolution then proceeds similarly if both the initial conditions are identical and the shock driver evolves similarly on the timescale $t = L/\tilde{u}$. In future work, we will seek to identify this specific scaling between initial conditions.

3.3.3 Experimental predictions and projections to the astrophysical case

For the model experiment and the astrophysical analog, the solution of Eqs (3.1)-(4) for the convective Mach number given in Eq. (3.6) and other flow properties is shown in Table 3.3.2. Because both systems are ram pressure dominated, we show that the solutions are fundamentally identical and predict potential KH growth values. We note that the growth time scale is largely geometrical, fixed by the time of travel for a point down the deflected

interface (red, dashed line in Fig. 3.3), and is not sensitive to ΔU for the parameter ranges given here. The KH growth rate, however, is much more sensitive to non-geometrical parameters, quickly stifled by large contrast ratio and high wavelength perturbations $\lambda \sim R_s$, assuming a relatively stable shock velocity of $U \sim 200\ \mathrm{km\,s^{-1}}$.

The systems with $\gamma_s = \gamma_b = 5/3$ are predicted to be supersonic with a convective Mach of $M_c = 0.87$ and a growth time to KH growth rate ratio $t_{growth}/\tau_{KH} = 3.76$. In the model experiment with $\lambda = R_s = 100$ μm, a $h_0 = 5\,\mathrm{nm}$ perturbation amplitude will grow to $h/\lambda_{shocked} \sim 0.1$ in roughly 0.5 t_{KH} cycles. This implies that the growth observed will be out of the linear, exponential growth model after roughly 1.8 ns. With regards to diagnostic capability, for a collapse length estimate of $L = 312$ μm (neglecting the point of shock reflection) and with a shocked wavelength of $\lambda_s = 77$ μm we can expect to observe in the linear regime at least the first of roughly four KH unstable peaks on the collapsed interface. At similar shock velocities and for a wavelength greater than this, it is expected that the KH instability will stay longer in the linear regime.

For example, if $\lambda = 2R_s = 200$ μm, the model predicts that $t_{growth}/\tau_{KH} = 1.88$ so that all four of the deflected peaks will be in the linear regime. However, if $\lambda = 0.5R_s = 50$ μm, then $t_{growth}/\tau_{KH} = 7.52$. For smaller wavelengths, current radiography diagnostics may become increasingly difficult. We again note that to be consistent with current astrophysical predictions, $R_s/\lambda \geq 1$.

For the astrophysical case, the same (adiabatic) behavior is expected via hydrodynamic similarity. A consequence of the KH instability is that if KH is allowed enough time to evolve, then significant mixing will occur between the hot shocked background and colder, denser shocked filament. As the KH instability is only able to grow to the effective width of the shocked filament layer (the region between the transmitted shock and the deflected interface as shown in Fig. 3.3), maximally the shocked layer can be mixed into the background. This does not reduce the unshocked areal mass flux of the filament. However, the KH instability may reduce the areal mass flux of the shocked filament region. The overall effect is inhibited mass delivery towards a critical radius inside the galaxy, where gas may accrete and coalesce into stars. This expected behavior is modeled in Fig. 3.4 where low and high disruption describes the low and high growth time scenarios for a relevant parameter range. We plan to develop this consideration in further work.

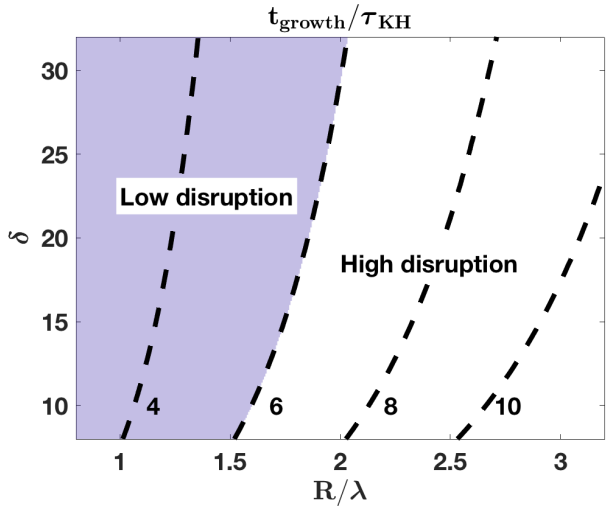

Figure 3.4: Contours of t_{growth}/τ_{KH} as predicted by the oblique shock model for a range of ratios R_s/λ and δ. As the system becomes dominated by available growth time, the KH becomes more disruptive to the overall collapsed filament evolution, increasing mixing between the shocked background and filament. In order to achieve such enhanced mixing, we estimate several turn over times are required during the stage of KH growth, indicating that t_{growth}/τ_{KH} should exceed $\sim 3-5$. Here, we choose $t_{growth}/\tau_{KH} \sim 6$, in order to satisfy the $R_s/\lambda > 1$ condition, discussed in Sec. 3.3.3.

3.3.4 Radiative cooling of the background plasma

Strong radiative cooling in both the shocked background and filament plasmas can significantly alter the collapse dynamics and KH growth. In this section we discuss the radiative cooling model for both plasmas and apply it to the background plasma.

As the photon mean free path, l, is many orders larger than the typical length scale of the system $l \gg L$, the cooling in both plasmas is assumed to be free-streaming with no effect on the optically thin infall. We utilize the microscopic cooling function Λ_{mic} as a function of temperature T provided by [113, 4], shown in Fig. 3.5. The microscopic cooling function identifies the power radiated per particle with units $\mathrm{erg\,cm^3\,s^{-1}}$. Fig. 3.5 shows two curves of Λ_{mic} for a low density astrophysical plasma in collisional-radiative equilibrium with a hydrogen mass fraction $X = 0.9$, a varying helium mass fraction Y, and a varying mass fraction of elements heavier than helium $Z = 1 - X - Y$ in units of solar metalicity. For both curves, at less than a few eV, hydrogen is molecular and cools inefficiently. At $T \sim 10^4$ K, cooling locally peaks due to Lyman α line emission at roughly $\log \Lambda_{mic} \sim 2 \times 10^{-22}$ $\mathrm{erg\,cm^{-3}\,s^{-1}}$. At 10^5 K the second peak appears due to recombination of He. The presence of metallicity $Z > 0$ introduces more atomic bound-bound

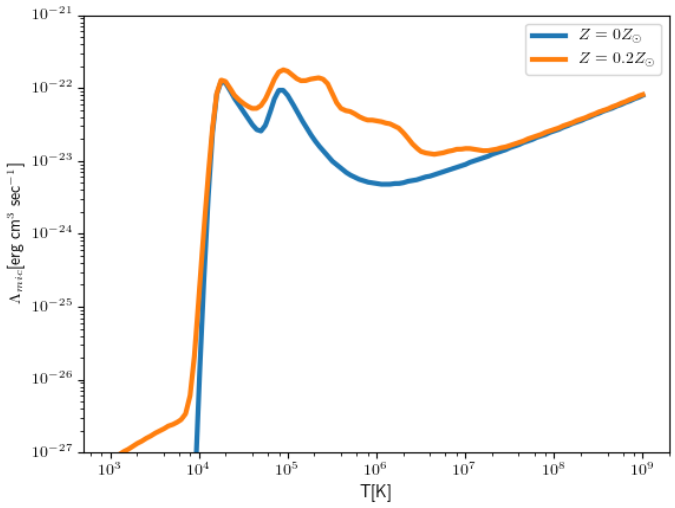

Figure 3.5: The logarithmic microscropic cooling function, Λ_{mic}, as a function of temperature for a low density astrophysical plasma with a $X = 0.9$ hydrogen mass fraction and varying helium and heavier element mass fractions Y and $Z = 1 - X - Y$, respectively. Based on the MAPPINGS-V plasma code [4].

transitions that increases the cooling rate after being collisionally ionized by free electrons. At much higher than 10^6 K Bremmstrahulung dominates. While the presence of metallicity adds additional features, we assume a $X = 0.9, Y = 0.1$ plasma.

The microscopic cooling function can be used to approximate the cooling time via

$$\tau_{cool} = 4 \times 10^{-36} \frac{A(Z+1)T(eV)}{Z\rho(\mathrm{g\,cm^{-3}})\Lambda_{mic}} \tag{3.12}$$

which is the ratio of the energy density of the plasma to the radiated power per unit volume [18]. For the shocked background at temperatures on order of $10^6 K$, the cooling time is $\tau_{cool,b} \approx 2.8 \times 10^{16}$ s. We compare this to the compression timescale of the virial shock

$$\tau_{virial} = \frac{28}{5} \frac{r_s}{|u_0|} (1 - 3\tilde{u_s})^{-1} \tag{3.13}$$

suggested by the stability criteria of [91]. Here r_s is the shock radius (assumed to be the virial radius ($r_s \sim R_v$), u_0 is the radial velocity of the pre-shock gas (assumed $u_0 = U$), and $\tilde{u_s}$ is a term proportional to the shock velocity. Assuming a stationary shock, i.e. $u_s = 0$, Eq. 3.13 can be reduced to a simple relation $\tau_{virial} \sim R_v/U$, which is the effective hydrodynamic timescale in the strong-shock limit (less the multiplicative factor of $28/5$). It is a necessary condition for the existence of a virial shock that the cooling timescale of

the hot background plasma in the halo is at least on order of this hydrodynamic timescale, that is that $\tau_{cool,b} \gtrsim \tau_{virial}$ in the background plasma. For the parameters used here, we note that $\tau_{virial} \approx 8.4 \times 10^{16}$ s. This is on order of the cooling timescale, arguably in the regime in which an accretion shock at the virial radius may exist based on prior order of magnitude estimates.

3.3.5 Radiative cooling of the filament

For the KH evolution on the filament, the hydrodynamic timescale of interest is the compression time of the filament, the ratio of the filament radius to the sound speed in the filament, $\tau_{hydro} = R_s/c_s \approx 1.1 \times 10^{12}$ s. In the shocked filament the material at a temperature of roughly 10^5 K, the cooling time is $\tau_{cool,s} \approx 2.0 \times 10^{13}$ s. Using an expected astrophysical value of τ_{KH} such as one from the third row of Table 3, the hierarchy of timescales is obtained:

$$\tau_{virial} \sim \tau_{cool,b} > \tau_{KH} > \tau_{cool,s} > \tau_{hydro}. \tag{3.14}$$

The last equality implies that radiative cooling in the filament is not likely to compress the filament faster than hydrodynamic effects. Thus the assumption that the pressure of the background drives the overall collapse dynamics is reliable. However, because $\tau_{KH} > \tau_{cool,s}$ cooling is likely to be important in describing the KH evolution, as the dynamical rate is $\gamma \sim 1/\tau$. Radiative cooling therefore has the potential to transport energy from the filament to the background faster than KH mixing. We develop this further.

Consider the change in energy density $\rho\epsilon$ of the shocked gases, which is proportional to $\rho T \sim$ const. The denser filament is a much more efficient cooler at roughly 10^5 K than the background at 10^6 K. In removing energy content from the post-shock filamentary gas, radiative cooling removes pressure support behind the oblique shock in the filament. Across the deflected material interface, the post-shock materials have equal pressure $P_0 \approx \rho_b U^2$. The shocked filament material will cool faster than the shocked background, which will maintain its pressure P_0. The cooling layer then condenses to maintain pressures P_0 at the new cooled temperature T_{cool}. This effectively causes the filament shock to recede, with the velocity of post-shock gas relative to the shock growing increasingly subsonic and thus increasing pdV compression of the post-shock material. Such a reduction in shock-speed has the effect of reducing the post-shock temperature towards 10^4 K, where the cooling rate rapidly drops off. The overall hydrodynamic response is that of a wider deflected angle θ with a shallower post-shock region in the filament at higher density ρ_{cool}. This decreases the

sound speed of the material $c_2 \propto \rho^{-0.5}$, increasing the convective Mach M_c. Alternatively, we may effectively assume the filament is isothermal, having $\gamma = 1$, with a constant cooled temperature of 10^4 K. In this case, the convective Mach number can be estimated as

$$M_c \sim \frac{\Delta u}{\sqrt{P_0}\left(\sqrt{\frac{1}{\rho_b}} + \sqrt{\frac{1}{\rho_{cool}}}\right)}. \tag{3.15}$$

The Atwood number will increase as the shocked filament goes to higher density, thus reducing the classical KH grown rate. The shear difference between the layers Δu will be smaller, since at higher deflections the velocity component parallel to the interface decreases. An idealized limit thus has $M_c \rightarrow U\sin(\phi - \theta)/c_b$ as $\rho_{cool} \gg \rho_b$, approaching the Mach number of the oblique shock $S1$, $M \sim U/c_b$. Thus, any significant amount of radiative cooling is predicted to stifle the KH instability. To illustrate this effect, the ideal astrophysical model with $R_s/\lambda = 1$ as discussed in Section 3.3.3 may have a cooled convective Mach of $M_c \sim 1.13$ and $t_{growth}/\tau_{KH} \sim 0.5$ as the shocked filament cools to 10^4 K. Compared with the value of $M_c = 0.87$ in the third row of Table 3, the effect of cooling may be dramatic.

Without significant cooling the experimental platform therefore provides the upper adiabatic limit to the astrophysical case, one in which KH may have the most significant role in the hydrodynamic evolution of the filament. If cooling is as significant as the arguments presented above may suggest, then KH might play a very minimal role in the overall dynamics. As we move to more radiative regimes with the experimental platform to study this phenomenon, we will be able to validate more of the physics described.

3.3.6 Additional instability modes

For the platform and regime discussed we consider conventional surface modes, so that the primary behavior is described by the KH theory presented. These modes grow as a fraction of the virial crossing timescale $t_v \sim R_v/c_b$, where c_b is the sound speed of the background material. However, the series of papers analyzing the instabilities subject to cold filaments, namely [98, 99, 100] identify that body modes may dominate over surface modes for a range of parameters (δ, M_b), where M_b is the background flow Mach number, and geometrical configuration. These grow as instabilities inside the body of the filament, on a time scale of the order of the virial crossing time less the sound crossing time of the stream, $t_v - t_s$, where $t_s \sim 2R_s/c_s$ and c_s is the sound speed in the filament. For the experimental model, $t_v \sim 100t_s$, suggesting that the virial crossing time dictates the

available growth time for both mode types. However, as

$$M_b = M_c \left(1 + \sqrt{1/\delta}\right), \tag{3.16}$$

with $M_c \sim 0.87$ and $\delta \sim 10$ in our configuration (resulting **in** stable body modes with $M_c < 1$), we get $M_b \sim 1.15$. This is a little below the critical Mach $M_{\text{crit}} = 1.29$, idenitifed in [98] as

$$M_{\text{crit}} = \left(1 + \delta^{-1/3}\right)^{3/2} \tag{3.17}$$

for which surface modes are expected to dominate.

[99] extends this work to the non-linear analysis for 2D slab geometry. However, we note that it is still applicable for cylindrical geometry. Moving to 3D simulations, [100] revealed that the behavior is drastically different for supersonic streams, wherein azimuthal surface modes may grow in a much larger rate than the conventional radial surface modes as expected for 2D streams. For the model experiment, the seeded radial perturbation has $h/\lambda = 0.05$, with no azimuthal modes. However, some azimuthal modes might appear, due to symmetry breaking and asymmetries introduced in target fabrication. The initial amplitude to wavelength ratio of these modes should be very small ($h/\lambda \ll 1$), therefore their amplitude is not expected to exceed that of the radial modes during the experimental timescale. As we develop this platform further, full 3D calculations will help identify if this is the case for the experiment, as well as provide useful insight into expecting increase in mixing.

3.3.7 Additional Physics

There are several other physical processes that will need to be considered in future work. These processes are summarized in [98, 99], but briefly they include radiative cooling, the effects of which have been considered in Sec. 3.3.4; thermal conduction, which is hydrodynamically negligible for large wavelengths as discussed in Sec. 3.3.2; external gravity of the background on the filament; self gravity of the filament on in itself which may lead to filamentary fragmentation, as recently considered in [114]; magnetic fields that could drastically affect overall KH evolution as well as thermal conduction, as recently considered in [115]; and potentially other effects of galaxy formation. Some experimental campaigns which include magnetic fields for astrophysical relevant Rayleigh-Taylor instability applications are planned for the National Ignition Facility (NIF). Future design work might adapt the current experimental platform to NIF, exploiting both NIF's much larger

laser energy combined with relevant magnetic fields, resulting with a significant magnetic Reynolds number.

3.4 Conclusion

In this chapter I presented a hydrodynamically scaled experiment meant to study the dynamics of filamentary mixing (i.e. KH related mixing) in dark matter halo galaxies. The experimental regime is expected to be close to the adiabatic limit. In this regime, the experimental model presented here may adequately describe the astrophysical case of a KH unstable filament terminating in a virial accretion shock during galaxy formation. Under strong shock scaling the two systems exhibit Ryutov scaling and thus are said to evolve hydrodynamically similarly. Thus the radiography diagnostic used in the experiment may help verify the physics of filament collapse and KH evolution on the deflected interface of the collapsed filament, by enabling the measurement of the angles involved in the flow through oblique shocks as well as the perturbation height during the KH growth. The experiment will allow the examination of KH growth on a filament interface, and provide insights regarding the largest amount of mixing that might be expected. Radiative cooling effects may be important and would be expected to decrease the mixing. The design is based on full, 2D simulations, along with a simple oblique shock model, for estimating expected Mach numbers and growth rates for KH.

In future work, the mixing will be analyzed for its role in reducing aerial mass flux of the shocked filament. As the experiment is expected to be the upper limit as the adiabatic case, this aerial mass flux may be directly translated to a astrophysically relevant aerial mass flux and correspondingly linked to predictions for the star formation rate. Furthermore, the dependency between mixing and instability related quantities such as wavelength and Atwood number will be investigated. We note that future experiments would benefit from the use of larger laser platforms, such as NIF, capable of providing stronger shocks needed to increase radiative cooling rates, along with increasing typical target dimensions for late time evolution.

CHAPTER 4

Inferring the Temperature Profile of a Radiation Wave Undergoing a Supersonic-to-subsonic Transition in the COAX Experiment

4.1 Introduction

Modeling radiation flow experiments with radiation-hydrodynamics codes faces a number of challenges with uncertainties in the initial conditions, equation of state, opacity, and the numerical techniques coupling radiation to matter. A wide range of physical regimes is often present, such as plasma conditions whose electrons, ions, and photons have temperatures out of equilibrium in the hohlraum, radiation-collision-dominated transport in the target, multiple transmitted and reflected shocks, and ablation fronts. Constraining the uncertainties in each part of the modeled physics presents another challenge: the development of robust experimental test suites to probe and validate individual aspects of the radiation flow.

A large number of experiments use laser facilities to provide the direct or indirect laser drives and generate radiation driven waves under a various configurations, such as GEKKO II [35], VULCAN [116, 117], NIF [44, 45], and OMEGA [37]. The COAX experimental platform uses OMEGA-60 to deliver a laser drive into a hohlraum [118], producing a radiation wave and radiatively driven shock down a low-density foam [5]. The COAX platform is a successor to the Pleiades experiment, which employed a soft x-ray breakout measurement to inform the temperature and timing of the shock wave, but the simulations had limited predictive capability using the breakout measurement alone [45, 46]. Designers found it difficult to constrain their computational models due to the large, systematic underprediction of the breakout times. The discrepancies came from large, biased uncertainties in the simulations and experimental measurements that were too integral [46]. COAX

Shot	Duration [ps]	Outer ρ [g cm^{-3}]	Inner ρ [g cm^{-3}]	Spectral timing [ps]
86456	1260 ± 4	66.7 ± 4.2	70.9 ± 3.5	3226 ± 25
86459	1212 ± 4	66.8 ± 2.6	69.1 ± 1.5	2220 ± 25
86462	1256 ± 4	70.7 ± 1.5	66.0 ± 1.5	1199 ± 25

Table 4.1: Summary of COAX smooth target shots analyzed. Listed are key target and simulation parameters such as outer and inner foam densities, ρ. The radiography is performed approximately 800 ps after the spectra, where the integration windows are roughly 333 and 200 ps, for the radiography and spectra respectively.

improves upon Pleiades by using a titanium-laden foam that, via broadband backlighting across the radflow and measuring the ionization state of the titanium, provides spatially-resolved, time-gated, spectral information about the wave within the target [5]. Additional experimental constraints include a radiography diagnostic that provides a highly-resolved shock position as the radiation goes subsonic and a Dante x-ray diagnostic that measures the x-ray drive flux emitted by the laser irradiated hohlraum [119, 120].

Guided by the uncertainty quantification frameworks detailed in [46, 121], we develop a suite of 2D simulations with a laser-hohlraum model to inform our physical understanding of the radiation hydrodynamics occurring in the COAX experiment and increase the predictive capabilities of our codes [122]. The key focus of study in the COAX experiment is assessing, in detail, the radiation wave profile and consequently propagating uncertainties in the spectral diagnostic, in order to constrain the radiation hydrodynamics simulations. This work represents the first validation using the COAX platform diagnostic with uncertainty propagation.

Section 2 details the COAX platform, assessing the key physics that requires careful modeling. In Section 3, we present simulations of COAX experiments, first establishing a tuned configuration that matches shock positions using a base simulation model, then understanding how changing or implementing different physical models affects the simulation results. In particular, we focus on the drive and its effect on the shock position and temperature profiles. Section 4 summarizes model uncertainties and discoveries in the COAX platform. We form conclusions and propose future work in Section 5.

4.2 Modeling the COAX Platform

4.2.1 The COAX Experiment

COAX is an indirectly driven, radiation tube experiment. In a standard shot, 13 laser beams from OMEGA-60 deliver 500 J/beam with a 1 ns square pulse to the interior of a gold halfraum with an outer diameter of $1600\,\mu\mathrm{m}$, a laser entrance hole (LEH) diameter of $1200\,\mu\mathrm{m}$, a rear exit hole (REH) diameter of $800\,\mu\mathrm{m}$, a length of $1200\,\mu\mathrm{m}$, and a wall thickness of $25\,\mu\mathrm{m}$. Fig. 4.1 displays the dimensions and layout of the the target.

The laser-irradiated hohlraum generates a radiative flux through the hohlraum REH and launches a supersonic radiation wave into the foam that rapidly transitions to a subsonic wave, producing a shock wave that propagates axially down a foam cylinder assembly [5]. Inside the assembly is a Ti-laden, aerogel inner foam cylinder. Surrounding the inner foam coaxially is an undoped, aerogel outer foam cylinder. The inner foams have densities of $68.7\,\mathrm{mg\,cm^{-3}} \pm 3.5\,\mathrm{mg\,cm^{-3}}$ and outer foams have $68\,\mathrm{mg\,cm^{-3}} \pm 4.2\,\mathrm{mg\,cm^{-3}}$. A low opacity Be sleeve encases the entire foam assembly to prevent blowoff. In this work we consider only targets with sub-micron ($< 0.1\ \mu\mathrm{m}$) $\mathrm{TiO_2}$ dopant particles and having an atomic ratio of 1:5 dopant to $\mathrm{SiO_2}$ foam (approx. 21% by mass titanium). The summary of the selected shots is provided in Table 5.1.

Fig. 4.2 illustrates the configuration of the target with the diagnostic axes for a shot. All experimental setup information is described in detail in reference 8 and will only be summarized here. The Dante x-ray diagnostic measures the radiative flux from the LEH for the duration of the experiment at an angle of 69° from the coaxial center of the target. As the radiation flows down the tube and ionizes the inner foam, a Kr-filled, laser-imploded capsule backlighter, which is located off to the side of the tube, illuminates 1s-2p and 1s-3p absorption transitions of the titanium. An x-ray framing camera using a four-strip microchannel plate detector collects the absorption spectroscopy on film through a slit width of $37.5\,\mu\mathrm{m}$. The absorption spectra were collected with a 1-D space resolving spectrometer with a Ge (111) crystal and 3.8eV dE spectral resolution [5]. Finally, a radiography diagnostic provides flow feature information such as the position of the shock. Both radiography and spectroscopy are nearly orthogonal to one another, and their lines of sight are perpendicular to the coaxial center.

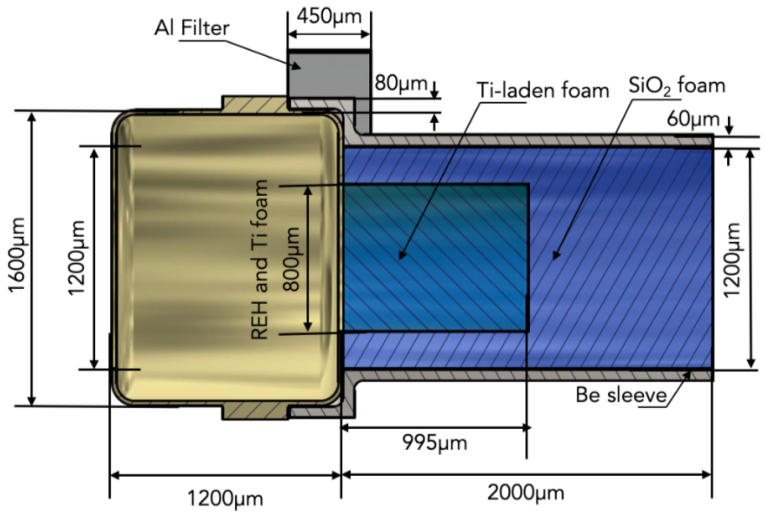

Figure 4.1: A diagram of the COAX target, showing the arrangement of the hohlraum, Be sheath, Al radiography filter, inner Ti doped aerogel foam, and outer aeorgel foam. Reproduced with permission from High Energy Density Physics 39, 100939 (2021) [5]. Copyright Elsevier.

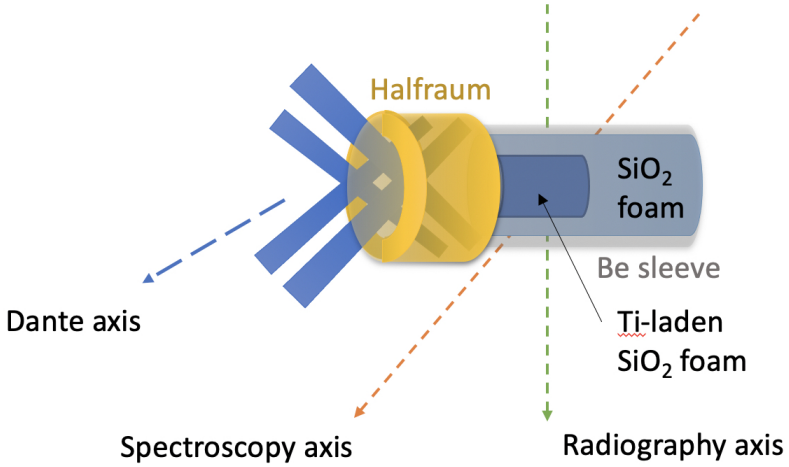

Figure 4.2: Illustration of the target and diagnostic configuration. Reproduced with permission from High Energy Density Physics 39, 100939 (2021) [5]. Copyright Elsevier.

4.2.2 Physics modeling

At early times in the foam, radiation heat transfer is the dominant energy transport mechanism. The maximal radiative fluxes into the target are approximately $\sim \sigma T^4$, where T is the radiation temperature of the incoming hohlraum flux ($T \approx 125\,\mathrm{eV}$ at peak, 1 ns), and σ is the Stefan-Boltzmann constant. These fluxes greatly exceed the material flux of the foam

$\sim \rho c_s^3$ where ρ is the density of the target and c_s is the sound speed of the foam, and thus material motion is negligible. The corresponding radiation hydrodynamic energy equation under these simplifications suggests purely diffusive behavior of the heat wave

$$\rho \frac{\partial e}{\partial t} = \frac{4}{3} \boldsymbol{\nabla} \cdot \left(\frac{1}{\rho \kappa_R} (\sigma T^4) \right) \tag{4.1}$$

where e is the specific energy of the wave and κ_R is the Rosseland mean opacity. Marshak [34] derived a solution for the spatial evolution of this front given a constant boundary temperature, $x \sim \sqrt{t}$. The Mach number of this wave $M = \frac{\dot{x}}{c_s} > 1$ dictates that the radiation wave is supersonic. However, as the radiation wave heats the material, material fluxes no longer remain negligible and heated material piles up near the front.

We can estimate the Mach number for which the transitioning radiation wave can generate material fluxes leading to compression of the wave heated fluid, by analyzing the equations governing conservation of mass $\rho_1 u_1 = \rho_2 u_2$ and conservation of momentum $p_1 + \rho_1 u_1^2 = p_2 + \rho_2 u_2^2$ [123]. Here subscript 1 denotes the downstream region heated by the wave and subscript 2 denoting the upstream region. Assuming a steady radiation heat wave, with near constant temperatures ahead and behind the front, we can express the corresponding pressures in terms of their isothermal sound speeds, $p = \rho c^2$ [1]. The conservation equations can then be arranged to express this compression,

$$\frac{\rho_2}{\rho_1} = \frac{u_1^2 + c_1^2 \pm \sqrt{(u_1^2 + c_1^2)^2 - 4 u_1^2 c_2^2}}{2 c_2^2}. \tag{4.2}$$

Eq. (4.2) has only real solutions when $u_1^2 > 2 u_1 c_2 - c_1^2$. For the downstream temperatures much higher than the upstream, $c_2 > c_1$ and $u_1 > c_1$ so that $u_1 c_2 \gg c_1^2$, we can argue that critically the downstream Mach number must be $M = u_1 / c_2 \gtrsim 2$. This transition has been experimentally observed [123]. For the COAX experiment, we find that this transition occurs when the wave slows to approximately 150 μm ns$^{-}1$ at approximately 2 ns into the experiment, with an upstream Mach of $M \approx 1.8$. Eq. 4.1 no longer remains valid during the transition to subsonic behavior and the corresponding wave must be modeling with the full equation of radiation transport, at minimum including a PdV work term in the energy equation of Eq. 1 and treating the density ρ as non-constant. Ideally, the ionizing plasma conditions and opacities of the now heated foam require more detailed physics as well.

The heated material couples to radiation more strongly and increasing pressure behind the front may eventually form a strong shock. In the temperature and density regime of COAX, the wave follows this behavior in the transition from a supersonic heat wave to a

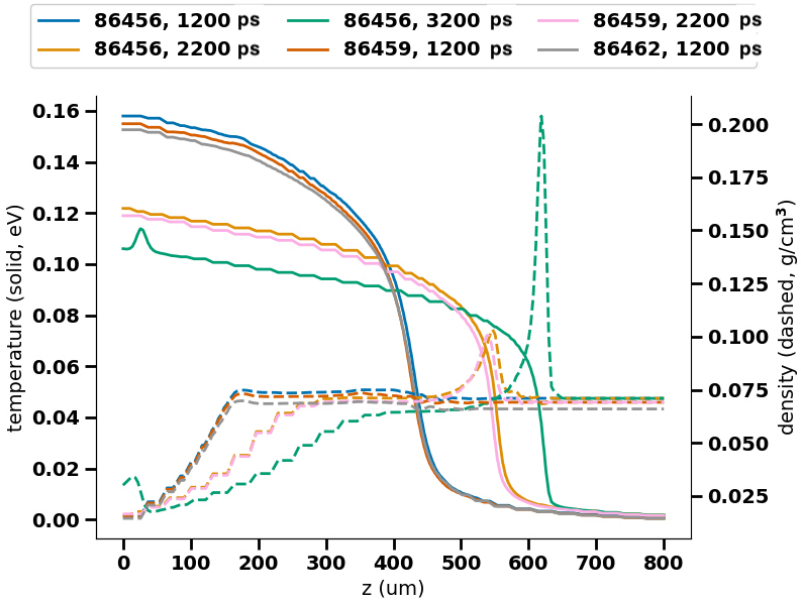

Figure 4.3: Temperature (solid) and density (dashed) from idealized 2D simulations of the experiment, taken along the coaxial center of the target. The evolution of the temperature wave demonstrates a transition from supersonic behavior (1200 ps) where material motion is negligible near the front, to subsonic behavior (2200 ps). By late times (3200 ps), we readily see the formation of a strong shock.

subsonic wave with a the formation of a strong shock. Fig. 4.3 demonstrates this behavior. Shown are the temperature profiles of the waves (solid lines) along the coaxial center along with density at the same times (dashed lines) for the shots listed in Table 1. The times are chosen to reflect the times during which the spectra are taken. At early times (shown at 1200 ps) the wave is supersonic, but by approximately 2200 ps into the experiment, the wave coupling to the foam generates small fluxes that eventually become a strong shock (green curve at 3200 ps for shot 86456).

However, while numerous analytical models exist for the evolution of a supersonic heat wave in HEDP conditions [124, 48], curvature of the supersonic wave due to lossy boundaries [76], the subsonic behavior [77], and recently a solution for a full transition from supersonic to subsonic behavior [3], none are yet readily applicable to COAX. For example, the drive used in COAX is a relatively short drive 1 ns pulse generating a high peak flux but low and rapidly cooling flux after peak, yielding a strong deviation from an approximately constant temperature source. Furthermore, the rear exit hole (through which the hohlraum flux enters the target) is the diameter of the inner foam and not the outer foam. This seeds much stronger curvature because the heat wave must diffuse radially

through the outer foam in addition to axially down the target. Such features produce radiation waves that significantly deviate from analytical behavior. While COAX was not purposefully designed to verify analytical behavior of Marshak waves, the theoretical basis described provide an understanding of the modeling physics needed to simulate the wave.

Thus modeling the full COAX experiment requires at minimum a simulation code that solves the full equations of radiation hydrodynamics to evolve the transition from the supersonic heat wave to subsonic behavior and eventually the strong shock. This includes multi-temperature plasma physics to account for photon, electron, and ion populations; appropriate multi-group opacity physics that span the wide temperature, density, and equillibria regimes between the photon and electron populations; and a laser modeling package capable of simulating the laser-hohlraum interactions that provide the drive for the radiation heat wave into the foam target.

4.2.3 Modeling and analysis tools

For our simulations, we use the LANL Eulerian radiation-hydrodynamics code Cassio, which is a version of the xRage code including advanced methods for coupling radiation to matter [53]. Cassio solves the radiation transport equations using diffusion, implicit Monte Carlo (IMC) [125], or discrete-ordinates (S_N) [126, 127]. We use the IMC method with adaptive-mesh refinement, a three temperature (3T) model for separate ion, election, and radiation heat conduction, and SESAME tabulated equations of state for all materials [56]. To model the indirect drive, we use the ray-tracing laser package Mazinisin [128, 129] adapted for use in the Cassio code. Cassio has been tested against a number of analytical models in radiation transport with diffusion and IMC solvers, including Marshak waves [130, 53, 131, 132, 46].

Time-dependent nLTE atomic physics modeling must account for not only distinct temperatures between the electron, ion, and radiation populations, but possibly the more general case of time-dependent, non-Planckian photon and non-Maxwellian electron distributions [133]. However, calculating opacities and emissivities in this manner, using inline nLTE methods, typically dominates the computational cost and significantly limits a systematic study of an experimental suite. Cassio's 3T implementation allows for separate temperatures for the electron and ions, but assumes each can be described by a Maxwellian fit by individual temperatures. For hohlraum models, we know this to be an approximation of the electron distribution. The laser ablation of the hohlraum walls produces a low-density

coronal plasma at densities on order of $0.01\,\mathrm{mg\,cm^{-3}}$ with electron energies ranging from approximately 1200 to $1800\,\mathrm{eV}$, greatly exceeding the average radiation temperature of roughly $180\,\mathrm{eV}$, resulting in a state of non-local thermal equillibrium (nLTE) [134]. This affects not only the treatment of the ion/electron pressure, but also the atomic opacities. The simulations in this work employed a tabular nLTE approach to investigate the effect of unequal electron/radiation temperatures on the atomic quantities via a linear response method (LRM) [135]. The present nLTE opacity tables were pre-generated with Planckians as the reference photon distribution. Within a particular cell of the Cassio simulation, the LRM is applied to account for any non-Planckian behavior of the photons, and then nLTE opacities and emissivities are obtained via interpolation of the tabular data at the specific conditions of interest. We contrast this to LTE models using opacity multipliers to emulate an enhanced opacity in the hohlraum for use in the laser-hohlraum modeling [122]. These LTE models enable a useful estimation of electron temperatures in the hohlraum that may be comparable to those found in nLTE simulations. We note that in this work, when we refer to LTE and nLTE models, we are referring only to the implementation of the opacities and that these models do not apply to the atomic physics of the foam.

The choice of an opacity multiplier of 4 for LTE hohlraum opacities is used consistently in this work. This opacity multiplier is not tuned to recover the nLTE model but to yield a physically consistent solution: opacity multipliers below this can lead to very high electron temperatures, overestimating the flux exiting the hohlraum, and injection of hohlraum material into the foam; multipliers above this may yield hohlraum models that cool too rapidly [136]. While the lower opacity multipliers may generate higher plasma pressures, our simulations do not predict the generation of jets of hohlraum material or any secondary shock waves generated from on-axis stagnation of the hohlraum plasma (eg. [137]), nor has it been observed in COAX experimental data.

In the foam, LTE assumptions are suitable for modeling the atomic physics of the radiation flow. The densities are sufficiently high that the electrons will equilibrate quickly and are reasonably-well described by a Maxwellian. In addition, electron collisions dominate the atomic level states and the small deviation between electron and effective radiation temperatures does not alter the opacity for these foams. Hence, using LTE opacities for the foams is sufficient for the models studied in this work [121]. Furthermore, we treat the foam as a perfectly homogoenous mixture, whose bulk thermodynamic properties are described by a pure $\mathrm{SiO_2}$ SESAME equation of state [56]. The opacities for the doped foam are calculated at the atomic mixture of 1:5 $\mathrm{TiO_2}$ dopant to $\mathrm{SiO_2}$ foam using opacities from

the OPLIB database [70].

In all simulations, we allow the AMR grid to refine to $0.5\,\mu\mathrm{m}$ in the hohlraum while the laser is active (first approximately $2\,\mathrm{n\,s}$) and then $2\,\mu\mathrm{m}$ after. At all times, the resolution of the foam and other materials are allowed to refine to $4\,\mu\mathrm{m}$, which is an appropriate maxmimum level determined by shock feature convergences in the foam. We ensure time steps of $1 \times 10^{-14}\,\mathrm{s}$ during the laser drive, then allow the time step to relax to $4 \times 10^{-12}\,\mathrm{s}$ for the remainder of the simulation.

We use simulated radiography in Cassio processed with Canny edge detection and various filters to find shock positions and features [138]. To determine experimental radiography features, we use XRIPL. XRIPL uses median and morphological filters for denoising, divides out a pseudo-flatfield to remove large scale lighting differences and retain fine-scale differences in contrast, and watershed segmentation to identify shock and Be inflow contours [139]. The process of tuning parameterized runs begins with matching shock contours and a detailed analysis on shock and radiography feature comparison is presented in Section 4.3.

For drive analysis, the Dante diagnostic data is processed by the open-source Dante analysis code FIDUCIA, which unfolds time-resolved spectra from the Dante measurements by using a cubic splines method [140, 141]. In simulations, we employ a radiation energy tally surface, whose fluence data can be converted to flux and directly compared to the FIDUCIA data. Section 4.4 discusses this comparison.

For spectra, experimental data is processed in IDL and the continuum is fit with ACOFI (automated continuum fitter), which uses an asymmetric least-squares fitting method that has been specially adapted to the problem of continuum fitting in absorption spectra [142]. Subsequently, the experimental transmission data is compared to simulated transmission spectra we produced using the SPECTRUM code [46, 121, 136], which is a ray-trace code modeling radiation transport with self-emission in the optically-thin approximation. We compare the processed spectra in Section 4.5.

4.3 Constraining density and laser power from features in simulated radiography

Because the spectra are obtained over a 200 ps window 800 ps before the radiography, the shock conditions for a given shot are not directly known at the time of spectroscopy. They can be inferred from the other shots due to the staggering of the spectra timings at 1200, 2200, and 3300 ps (see Table 1). We demonstrate the density and temperature of the shocks as a reference, for each shot simulation, at each of these times in Figure 4.3. We note that even with similar densities in each shot, we still must modify the laser drive multiplier by up to 5-10% to correctly match shock positions at each timing. For reference, the shock velocity in the range of interest is approximately $80\,\mu\mathrm{m\,n^{-1}\,s}$.

A significant modeling challenge is accurately detailing the shock in simulated radiography and then identifying the conditions needed to produce a simulated shock comparable to the experiment. In this section, we detail the process of modifying the key parameters of inner and outer foam densities, and laser power; how each affects features in radiography; and how we can constrain the parameters. We have conducted simulations to demonstrate that secondary parameters, such as the choice in heat flux limiter, spatial and temporal resolution, beam waist, and any hohlraum opacity modifiers, often have minimal sensitivity on the overall physics.

4.3.1 Examining radiography features and shock curvature

Fig. 4.4 identifies the features that can be confidently captured in a simulated radiograph of COAX shot 86456. We integrate simulated radiography over 20 ps simulation frames in a 340 ps window to emulate the motion blur in experimental radiography and then process them using Canny edge detection with filters. The primary shock (blue) and reflected wall shock (orange) are the key features we focus on in this study.

By integrating through the spectral window of 200 ps we can infer to what degree a shock and its leading heat front has passed a spectral lineout position. Fig. 4.5 shows that upper (dashed, red) and lower extremes (solid, red) fit the radiography error range, but during the spectral timing window, the shock may have not passed a spectral lineout position and perhaps produced weaker transmission. For example, compare how the lower shock position (blue, solid) has not crossed lineout position $617\,\mu\mathrm{m}$, but the upper shock position (blue, dashed) has. This is discussed in Sec. 4.5.

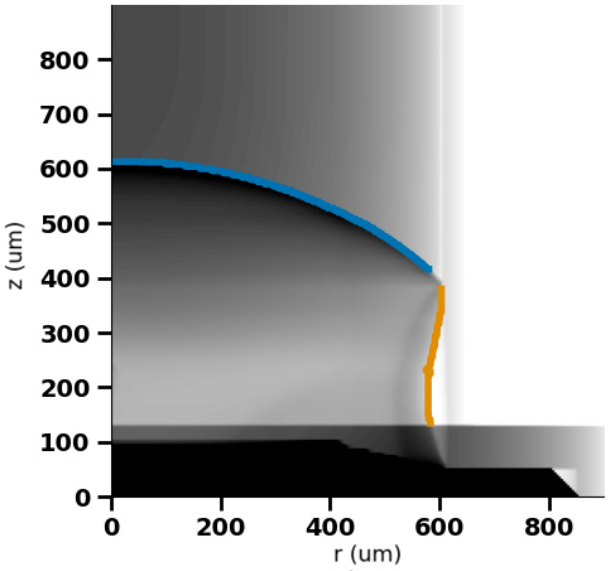

Figure 4.4: Example of features detected in a simulated radiograph of a shot 86456 simulation. The radiative shock (blue) is the primary feature of interest. The flow also produces a wall shock in the Be sleeve and a reflected shock into the foam (orange).

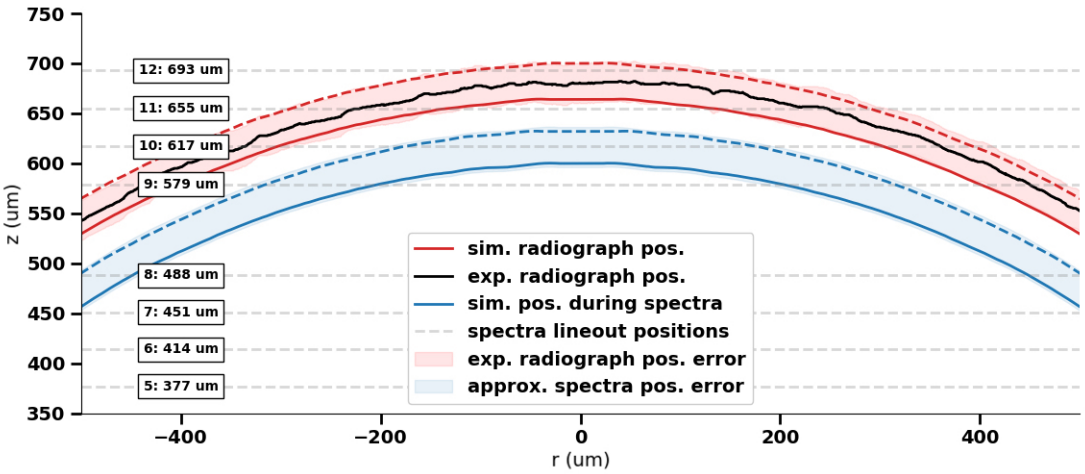

Figure 4.5: Upper (dashed) and lower shock bounds (solid) for a model of shot 86456 using two laser powers of 70% and 80% of nominal power in the expected radiography error range (red region). The black line indicates the experimentally determined shock position. When considering the shock profile while the spectral diagnostic is performed (blue), we must consider how the shock propagates through a spectral lineout position (for example see position 10, at $617\ \mu\mathrm{m}$.

When matching feature positions and curvature in cylindrically symmetric simulations, we must account for any natural asymmetry present in the experiment. The shots demon-

strate a relatively high degree of symmetry in the primary shock, roughly within a mean of 4.5 μm and maximum of 10 μm error. We expect an additional 2% error on the spatial conversion factor in the experimental analysis. The total asymmetric error may amount to $\pm$ 32 μm, while on average, the error is $\pm$ 26 μm. Additionally, the range of velocities present in the experiment do not significantly alter the amount of motion blur nor do they increase the stated uncertainty in shock position while integrating through the radiography window.

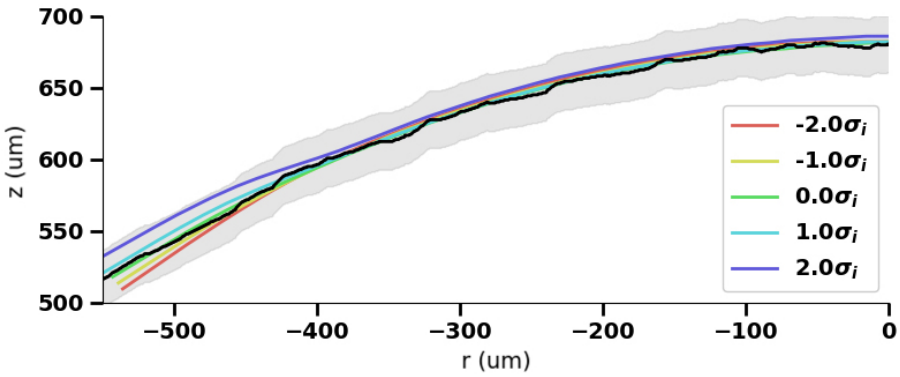

Figure 4.6: By changing the inner foam density and laser power we can produce nearly identical shock positions. Changes in curvature behave in an opposite manner to outer density changes: as inner density is decreased the shock curves more sharply compared to the experimentally determined shock position (black). At the $r = -400\,\mu$m position is the inner and outer foam boundary.

4.3.2 Constraining inner (doped) foam density to simulations and observing extrema

Fig. 4.6 shows the shock positions for shot 86456 simulations with fixed outer foam density, using inner foam densities within ± 1 to $2\sigma_i$, where the nominal density is $\rho_i = 68.7$ mg cm^{-3} and $\sigma_i = 4.2$ mg cm^{-3} is chosen as the largest uncertainty in all of the analyzed shots. The shock curvature and position in the inner foam varies within a few microns of one another. This precision is achieved by controlling the laser energy delivered in the laser-hohraum model and in this case represents a variation of 65% to 85% of nominal laser energy from lowest to highest density, respectively. In this inner density case study, the shock curves more strongly as the inner density is decreased as the shock is able to travel more quickly in a less dense foam (relative to the fixed outer foam density).

For completeness, we have analyzed how the shock curvature in the outer foam is affected when changing the density (see 4.6.3). The curvature evolves in a nearly opposite manner as those analyzed for the inner density changes. As the outer density was increased in the outer case study, the laser power did not need to be changed to match the shock in the inner foam, however, the shock curved more strongly (lagged) in the outer foam as the density increases and correspondingly, the sound speed of the outer foam.

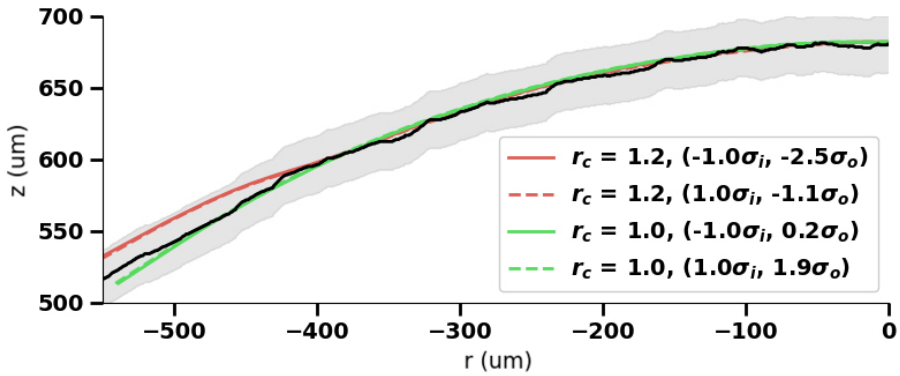

Figure 4.7: Despite a large difference in inner/outer density pairs and laser power delivered for each set of runs shown, the shock curvature is nearly identical for a fixed density contrast ratio r_c as compared to the experimentally determined shock position (black). At the $r = -400\,\mu\mathrm{m}$ position is the inner and outer foam boundary.

This phenomenological observation suggests that curvature is strongly a function of the contrast ratio between the inner and outer foam densities, r_c. In the outer density case study, the laser power was fixed constant, however, the laser power is allowed to change in the inner density case study. The drive spatial, spectral, and angular distributions into the target do not change significantly between these laser energy changes. We illustrate this observation directly in Fig. 4.7 where we analyze a set of fixed density contrast ratios. The shock position and curvature is nearly identical for each set of fixed contrast ratios, a case with higher inner density $r_c = 1.2$ and a case with lower inner density of approximately $r_c = 1.0$. In each case, the laser energy differs by roughly 20% yet still produces a nearly identical shock position.

With this analysis we present how simulations may be parameterized to produce nearly identical shock curvatures, identifying that radiography alone is not a sufficient constraint unless more features such as the Be wall shock are also analyzed (Section 4.6.3). Even

when considering the Dante as a constraint for hohlraum flux, due to complete uncertainty in flux values at the time of the radiography and spectral diagnostics, the wide range of parameterizations may still satisfy the potentially large error range. In the following section, we show that the spectral measurement is arguably the strongest constraint.

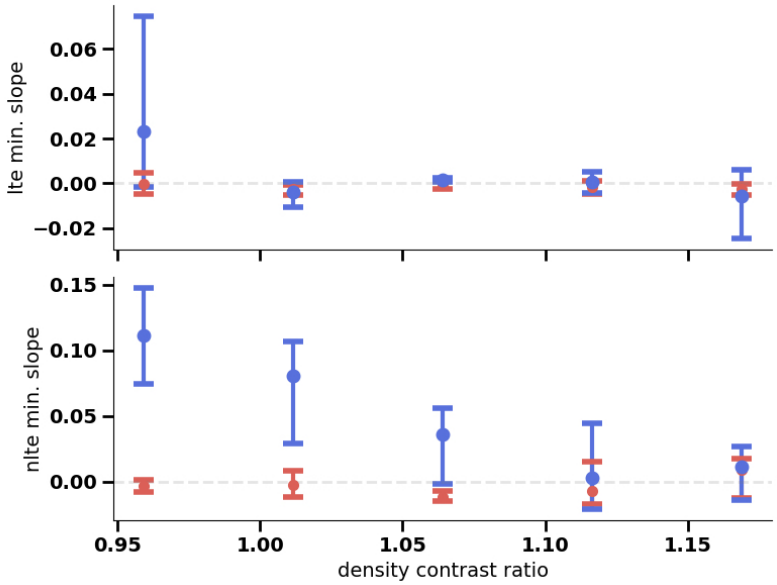

Figure 4.8: Error minimization for the primary shock in shot 86456 for LTE models (top subplot) vs nLTE models (bottom). Red error bars highlight the error in fitting the inner foam curvature, whereas blue includes error in the mean for the outer foam shock curvature. We find that LTE models with inner density sigmas of -1, 0, and 1 more consistently reproduce the shock curvature. The nLTE models reveal stronger curvature in the outer foam, indicating that an inner density sigma of 1 produces the best fit. Both models combined may reasonably select $+1\sigma_{inner}$ although this analysis may more confidently eliminate $-2, -1$, and $2\sigma_{inner}$. This analysis becomes more powerful when we are able to further constrain drive characteristics into the target.

4.3.3 Constraining the target densities

The preceding analysis demonstrates a number of important features of the experiment regarding the relationship of the densities and laser power to the positions and curvatures of the shocks present. What we seek now is refinement of the parameter space for each shot in this study by assessing the quality of fit of the simulated shock curvature. We use a least-squares fit on the error difference with prominent outliers removed. The simulation that produces the best curvature is then the minimization of the slope of the least-squares fit.

Shot	Shock position	Outer density	Inner density	Laser power
86456	680	70.9	74.4	76%
86459	844	69.4	72.1	85%
86462*	503.5	70.7	66.0	65%

Table 4.2: Summary of findings after shock error minimization analysis with nominal suggested parameters. Shock positions are in μm and densities in $\mathrm{mg\,cm^{-3}}$. For each of the shots analyzed, we suggest the maximum acceptable laser power given the discovered density contrast ratio. *While a higher outer foam density does visibly produce a better fit for shot 86462, because an outer foam shock was insufficiently imaged, we cannot make confident assessments but instead report the base nominal values.

Fig. 4.8 shows how the different opacity modeling choices for shot 86456 consistently suggest an inner density preference of $+1\sigma_{inner}$ when matching shock curvature. The blue and red indicate slope minimization in the shock curvature error when considering the entire shock and the inner foam shock only, respectively. By selecting the slope that is closest to 0 with the smallest error, we can select ideal density parameters for the shock matching. When comparing to the spectra, we look to data points constrained by this model as the ideal case.

As suggested in the inner and outer density case studies (Section 4.6.3), because the curvature in the inner foam is least sensitive to these changes and the outer foam shock is strongly sensitive to changes in the either inner or outer density, this analysis is most useful when a significant portion of the outer foam shock is available. In the analyzed data set, shot 86462 does not have a reliable shock position in the outer foam and thus the predictive capabilities of this method are not applicable.

The summary of the minimization analysis is available in Table 4.2. Compared directly to nominal values in Table 5.1, we are able to identify that simulations with typically higher than expected densities produce closer shock curvature for all shots except shot 86462. This in turn means that our models typically favor higher laser powers used in the simulations. We discuss the implications of this analysis when compared to the spectral analysis in Section 4.5.3.

4.4 Constraining hohlraum temperature and laser power with Dante measurements

The Dante x-ray diagnostic is used to probe the radiation emanating from the LEH of the target, located at an angle $\theta = 69°$ from the axial center of the hohlraum. Fig. 4.9 shows the spectrally integrated power and variability, suggesting up to $\pm 10\%$ in total power variability during the first $1.2\ \mathrm{n\,s}$. The peaks at late times are from the spectral backlighter. The time axis on this plot is arbitrarily shifted such that the peak flux from the hohlraum occurs at $1\ \mathrm{ns}$.

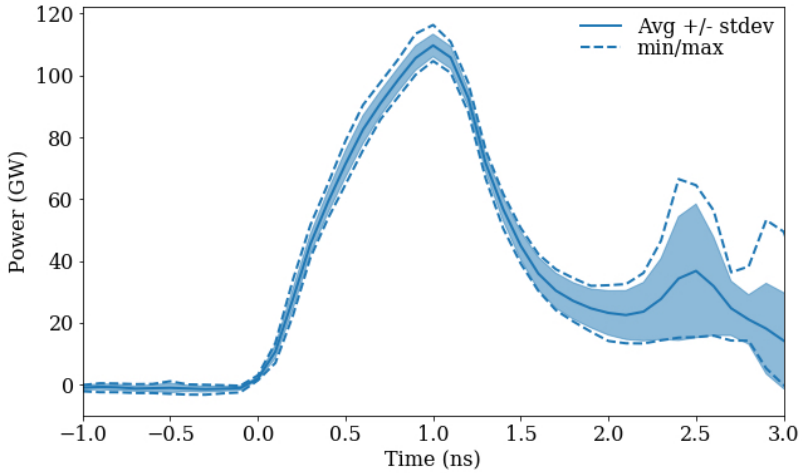

Figure 4.9: Power variability in the COAX shots. We expect up to 10% min/max variation in the Dante measured LEH flux. The sudden power increase near 2.4 ns comes from the spectral backlighter. We are unable to confidently infer hohlraum fluxes at times later than approximately 1.2 ns due to both high noise-to-signal ratio in the channels used as well as these backlighter signal intrusions.

To compare the simulated Dante flux to the experiment, we calculate angular flux from tallied fluence, then integrate over the binned angular resolution at the Dante angle. Fig. 4.10 shows the average simulated Dante flux, when models have $\pm\ \sigma$ in inner density and laser powers adjusted $\pm$ 5% of their nominal value. In this range of practical models where our expected parameters have errors of one sigma, the flux varies within 14% of the experimental Dante measurement. The model extremes having parameter errors of two sigma have peaks as low as 30% less and as high as 32% more flux compared to the peak of the Dante measurement. Thus we can argue that 2σ models have limited applicability because they do not capture the Dante measurement. Overall, the integrated total radiant energy ranges within 20% variation of the expected energy of Dante over the duration of

roughly the first $2.0\,\mathrm{n\,s}$.

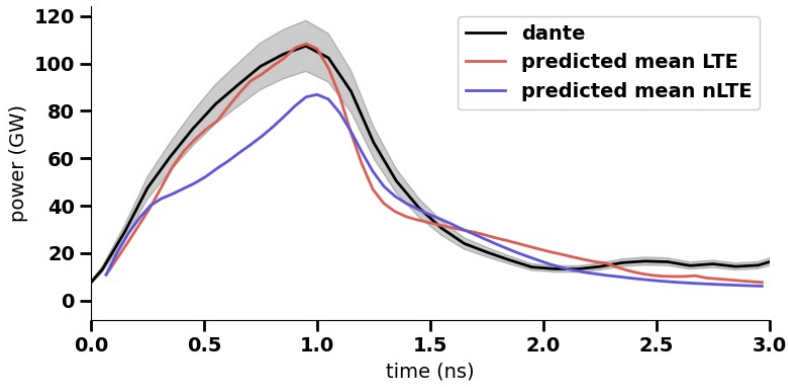

Figure 4.10: Simulated Dante measurements for the mean LTE (red) and nLTE (blue) models with 1σ density errors predict fairly different power, with LTE comparing well within the 10% variability through experimentally determined power (black) to 1.2 ns. We reiterate that LTE models are tuned with an opacity multiplier of 4 times the nominal opacity values to reproduce this flux profile, whereas nLTE models are unmodified by any parameters. The opacity choices modify the hohlraum opacities only and yield comparable evolution of the radiation wave in the foam.

These calculations do not account for LEH closure due to the irradiated plasma filling the hohlraum (e.g. [143]), however, for COAX this effect may only become important nearest the end of the first 1 ns of Dante measurment, beyond which noise-to-signal ratios become significantly higher and our measurement quality worsens. Assuming that the plasma flows away from the wall as an isothermal rarefaction via $n = n_s \exp(-x/c_s t)$, where x is the distance from hohlraum inner edge, c_s is the isothermal sound speed of the heated plasma taken to be $c_s = 7.3 \times 10^6 \sqrt{T_w/100\mathrm{eV}}$ cm s^{-1} for a wall temperature T_w, and $n_s = 10^{24}$ cm^{-3} as the approximate electron density of the wall, the time t to reach $0.001 n_s$ at the center of the hohlraum used in COAX is $\approx 0.61R/\sqrt{T_w/100\mathrm{eV}} \approx 0.4$ ns [1]. This implies approximately 2.5 filling times during the first nanosecond, and because the LEH radius is 600 μm compared to the hohlraum radius of 800 μm, the plasma having traveled 200 μm is expected to be $n \sim 0.12 n_s$ at $t = 1$ ns by this simple estimate. This effect may explain the larger discrepancy in simulated and measured Dante powers after 1 ns. As we continue to improve our diagnostic inference, we will incorporate appropriate Dante corrections. Nonetheless, given the uncertainties discussed, we consider these models reasonable predictors of the expected Dante flux.

4.5 Constraining shock temperature profiles with spectra

Our team applies several corrections and transformations to produce transmission data from the raw film, thouroughly described in Johns et al. [5] but briefly summarized here. The raw film must be spatially rotated; the film density converted to an intensity scale; artifacts, hot pixels, and flaws in the film removed; and each frame isolated to be analyzed individually. A frame is a section of the micro-channel plate (MCP) within the camera that provides four neighboring lineout positions. After the frames are ready, lineouts in the image yield the spectra. We then require some critical calibrations in processing these lineouts, namely an energy axis correction by comparing to known theoretical line positions and the removal of background continuum from the raw intensity measurement (Section 4.6.3).

4.5.1 Comparison of synthetic to experimental spectra

In Figure 4.11, we present the synthetic spectra for our model extremes for shot 86456, with the lower density case of $63.9\,\mathrm{mg\,cm^{-3}}$ and the upper density of $77.9\,\mathrm{mg\,cm^{-3}}$. The dashed curves are the results for the tabular nLTE models and LTE are represented by solid curves. These represent our coldest (blue, green) and hottest (orange, red) models, with all other models producing spectra that lie between these extreme transmission values. For the specfic energies of each ionization state of TiO_2 we refer the reader to Johns et al. [5]. We identify ionizations Ti^{13+} through Ti^{16+} as the accessible peaks in the analysis of 1s-2p data – these are the four distinct peaks evident in the solid, red curve in the lineout position $173\,\mu\mathrm{m}$ of Fig. 4.11 for example.

Comparison of the synthetic and experimental data of shot 86456 suggests several trends, consistent across all shots. Immediately evident is that even our most extreme LTE model may barely produce temperatures hot enough required to match the spectra at all lineout positions. For this example, in our coldest to hottest models we may achieve peak temperatures of approximately 94-95 eV to 102-106 eV. In all cold models, we fail to predict the spectral features at higher energies. However, at early lineout positions up to 251 $\mu\mathrm{m}$ it is possible that our higher temperature simulations predict hotter features than the experimental data, suggesting a hotter profile nearer to the hohlraum REH.

Another consistent feature of this analysis is the temperature sensitivity of certain spectral features. At some temperatures, the number of particles in a particular charge state may not change much in a given temperature range. For example in the first four lineout posi-

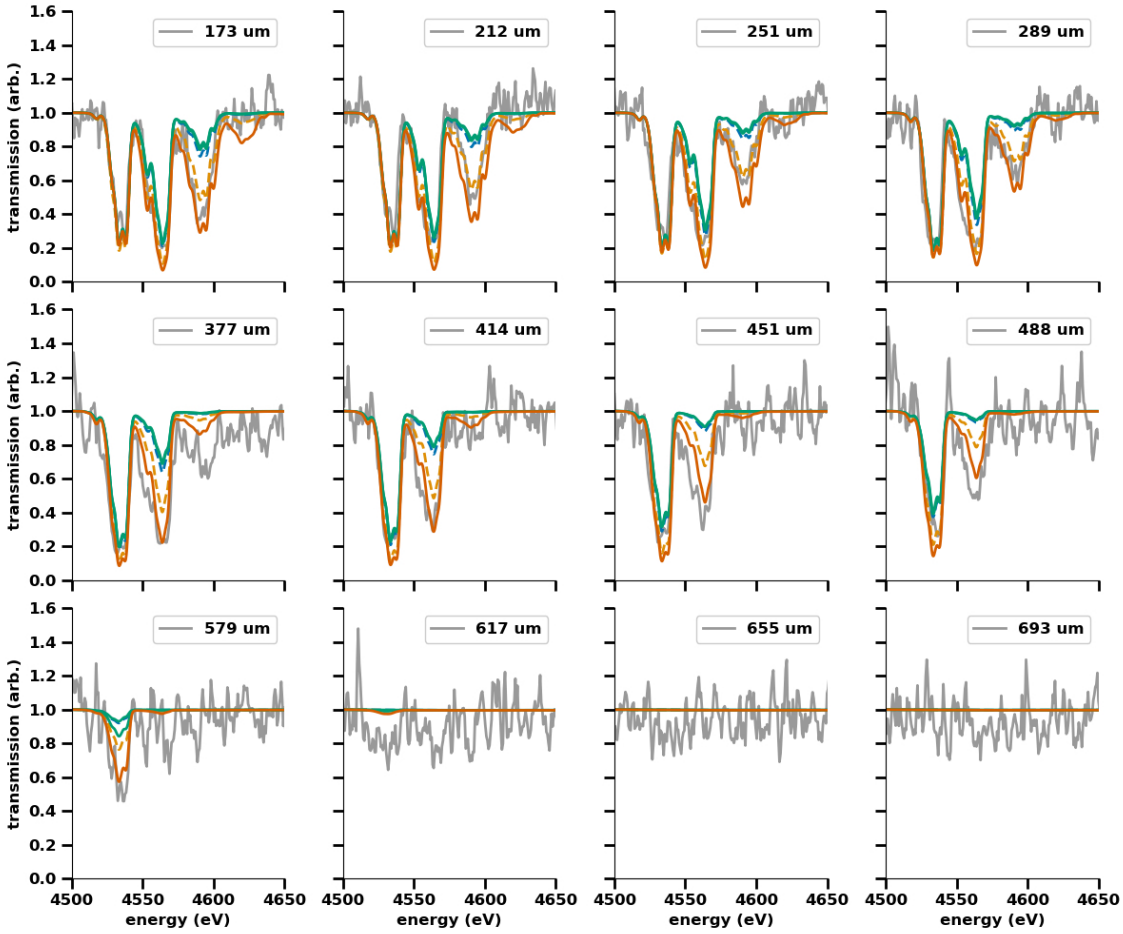

Figure 4.11: Experimental (grey) and synthetic (color) 1s-2p transmission for shot 86456 for all frames with analyzable data. Green and blue curves represent the coldest models (at $63.9\,\mathrm{m}$); orange and red are the hottest models (at $77.9\,\mathrm{mg\,cm^{-3}}$). The solid and dashed lines are LTE and nLTE for each set, respectively. These spectra highlight trends consistent across all shots, namely: the existence of lower energy peaks that may slowly decay with temperature (temperature insensitive), higher energy peaks that rapidly decay from position to position, and potentially a hotter position .

tions, the first peak at approximately 4540 eV, corresponding to the Ti^{13+} ionization stage, is insensitive to temperature change, despite spanning a temperature range of 90-110 eV. During the decay of higher energy lines such as the Ti^{15+} and Ti^{16+} ionization states, the line ratios between the Ti^{13+} and $Ti14+$ states remain approximately constant. The higher energy peaks begin to decay much more rapidly before these temperature insensitive peaks show significant decay. The sensitivity study performed by Fryer et al. [121] identifies that there are indeed a few 1s-2p lines that are very sensitive in this temperature range.

A final observation, present in all shots, is that there may be higher temperatures near

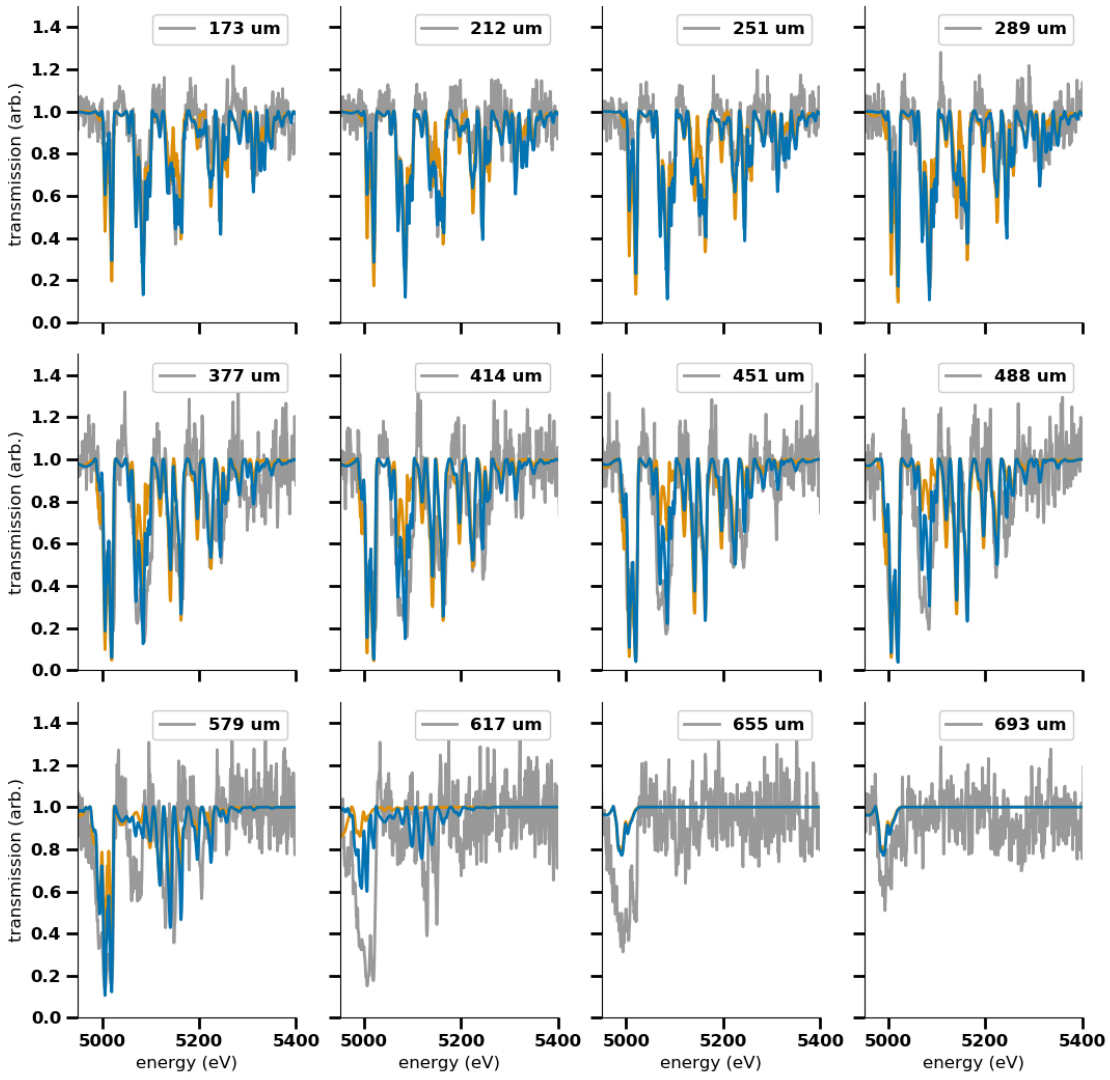

Figure 4.12: Experimental (grey) and synthetic (color) 1s-3p transmission for shot 86456 for all frames. Here we only show the hottest (blue at $63.9\,\mathrm{mg\,cm^{-3}}$) and coldest (orange at $77.9\,\mathrm{mg\,cm^{-3}}$) LTE spectra.

the predicted shock front during the time of spectra. This could be due to a number of reasons. The first is that our model may not accurately capture preheat or model higher energy transport appropriately at the front. The plasma between the radiation front and the shock front may not have thermalized yet. The second is that the shock position is further along in time or has more energy behind it than expected, despite our best efforts at matching shock positions during the spectral window. Other likely possibilities encompass the entire modeling effort, such as uncertainties in specific heat or equation of state.

For shot 86456, the nominal shock position is approximately 618 μm with temperatures of roughly 60-70 eV. The lineout positions show at 579 μm that the hottest models may be slightly cool, but by the lineout at the nominal shock position (617 μm), there is insufficient evidence in the 1s-2p spectra of features present. However, when we turn to the more sensitive 1s-3p features, as shown in Fig. 4.12, we can clearly see a slowly decaying feature at roughly 5000 eV in lineout positions 617, 655, and 693 μm. This is likely indicative of a hotter region ahead of the nominal shock position during spectra.

Constraining the data using the 1s-3p data is particularly challenging, as readily evidenced in even the first frame of Fig. 4.12 (lineout positions 173-289 μm), which shows the coldest (blue) and hottest (orange) LTE only models. While the colder model may produce slightly sharper lower energy features in this transition range, nearly all features are indiscernible until a lower temperature threshold is reached, approximately 92 eV by lineout position 377 μm, evidenced in the second transmission peak located between 5068 and 5075 eV. These first and second peaks are two easily accessible constraints on the temperature.

The differences in spectra produced by nLTE and LTE models are apparent but we argue that they are bound by laser energy choices. While LTE models do appear more temperature sensitive than the nLTE models, this discrepancy is likely caused by LTE models allowing a slightly wider range of permissible laser energies, thereby producing slightly colder and slightly hotter temperature profiles in the foam than nLTE models. The temperature profile differences shown in Figure 4.13 for a model of shot 86456 suggest that nominal LTE simulations are consistently only slightly hotter than the nLTE. A variation of a few eV is expected at late times, particularly near the shock front where the temperature profile steepens. At early times this variation can be tens of eV where nLTE models lag, but the nLTE model can quickly recover this lag. This is expected for our choice of opacity multiplier of 4 times the hohlraum opacity in the LTE models.

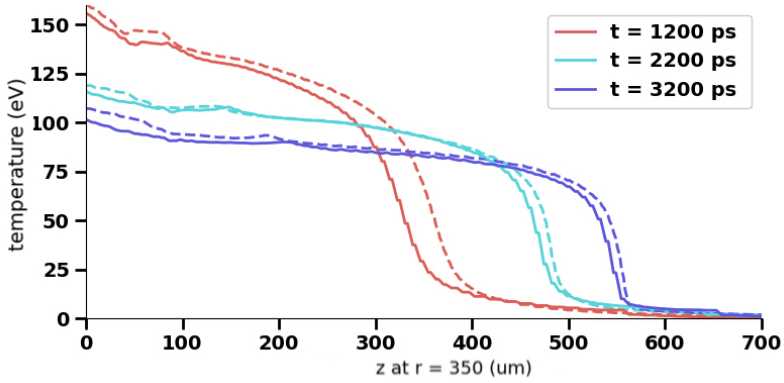

Figure 4.13: A shock wave travels axially down the foam and forms a distinct temperature profile. The shock is approximately located at the sharp temperature front. LTE (dashed) simulations may form hotter and slightly faster waves than nLTE (solid) if matching drives for a late time. At early times the difference is more notable. We note that the LTE and nLTE modeling choices modify the hohlraum opacities, used for laser-hohlraum interactions only. These choices do not affect atomic physics in the foam.

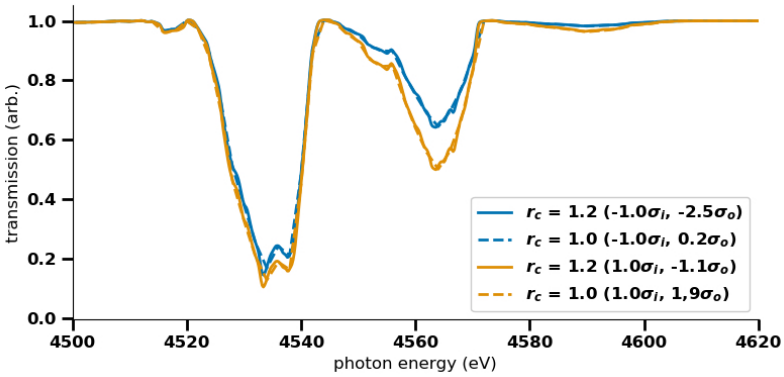

Figure 4.14: Selected 1s-2p transmission for the fixed contrast ratio cases of Fig. 4.7 at the radial lineout of 341 μm. In conjuction with Fig. 4.7, this figure demonstrates that theoretical spectra can be made practically identical for two different density configurations and that only temperature in the inner foam dictates the signature.

Despite these differences in the opacity models, at certain lineout positions we may not be able to distinguish modeling choices using spectra alone. Consider the contrast ratio tests of Fig. 4.7. Fig. 4.14 shows the spectra of the tests at lineout position 341 μm for LTE models and highlights that even given the wide density contrast range, temperature is key, as similarly explored in previous work [5, 136]. This has been observed for nLTE models as well. Laser energy changes directly change the temperature profile and remains

the most critical element of our modeling. Due to this relative insensitivity of the spectra to the density, our analysis is most effective when considering the LTE and nLTE models as temperature scalings of one another. At the same temperature, minor variations in curvature do not otherwise affect the spectra as we have shown minimal difference in shock evolution in the inner foams due to other parameter changes.

4.5.2 Temperature profile reconstruction

From the analysis in the preceding sections, we assert that temperature dominates the strength of transmission peaks in our parameter space and is arguably the key parameter in sensitivity analysis. By taking a reference model with nominal densities and laser drives required to produce a matched shock position, we scale the temperatures of the lineout profile by a constant factor to emulate a hotter profile and determine the approximate peak temperatures needed to reproduce the spectra. While spectroscopy does not integrate through a single temperature but rather a temperature profile, in this work we assume that in scaling the temperature profile we capture the fundamental spectral characteristics of our platform.

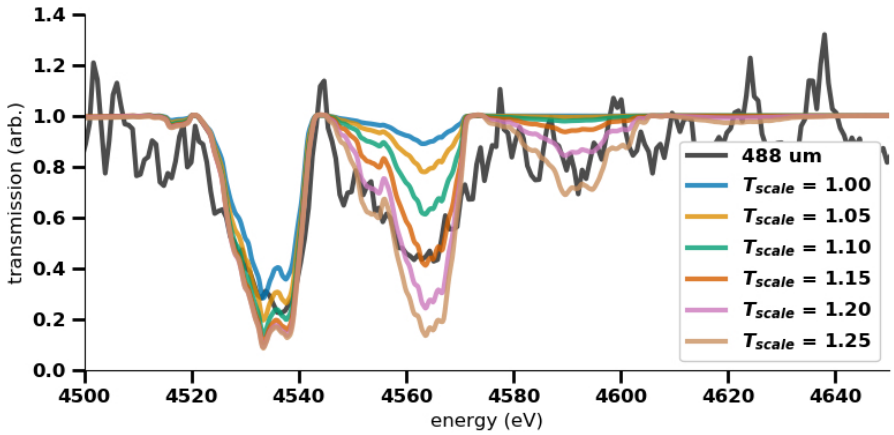

Figure 4.15: Spectra from scaling the temperature of the base LTE model at 488 μm. Evident are the Ti^{13+},Ti^{14+}, and Ti^{15+} features represented by the three prominent lines. At these temperatures, we are unlikely to predict higher energy ionization levels, thought they may not be distinguishable from background noise.

As an example, we show the base model and its temperature scalings for shot 86456 at position 488 μm in Fig. 4.15. In this figure we show the 1s-2p spectra for a model with nominal drive and density, along with scaled versions of the temperature profile at 5%, 10%, 15%, 20%, and 25%. At higher temperatures we can easily recover the spectra for

higher energy peaks in the lineouts closer to the shock position. We reiterate that generally we can increase the laser drive and correspondingly the density to achieve hotter temperatures, however, such increases (for example, to achieve a 25% hotter profile), we would need to model densities outside of the expected $\pm\sigma$ range.

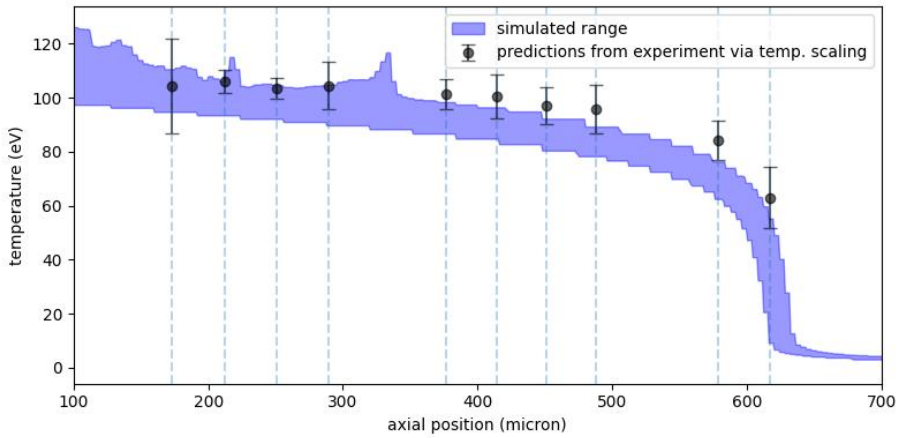

Figure 4.16: Temperature reconstruction of shot 86456 from temperature scaling of the base LTE shot. The blue region represents the peak temperatures achieved in the $\pm 2\sigma$ model range, and the points represent the inferred temperature from spectral comparison. At extreme laser powers, some hot hohlraum material may be present in simulations near the center axis where these temperatures are taken.

Using scaled profiles of each model, we can systematically infer the best fits to higher energy features and thereby assess what peak temperature the system ought to be to reproduce the spectra. By Fig. 4.15 we see that we begin to recover the feature at 4565 eV with a 10% increase in temperature of our base model but may recover a feature at 4590 eV with a 15% increase, although this feature is largely indistinguishable from noise in the experimental signal. Using similar estimations for each lineout position and interpolating between our temperature scalings, we can reconstruct the temperature profile. Fig. 4.16 shows such a reconstruction for 86456.

This figure clearly illustrates that in lineout positions closer to the hohlraum, simulations produce temperature conditions capable of matching the experimental spectra and likely exceeding them. For shot 86456, simulations suggest overlap with all inferred temperature points. However even within the 2σ range shown, all shots underpredict the temperature trend.

This is evident in the temperature reconstructions of shots 86459 and 86462 (Figs. 4.17

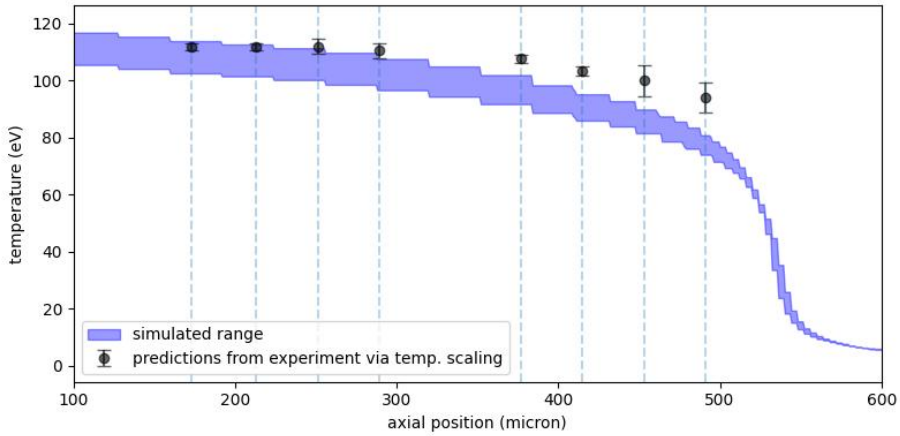

Figure 4.17: Temperature reconstruction of shot 86459 as done in the manner of Fig. 4.16.

and 4.18). Furthermore, as the lineouts approach the shock front, the experimental spectra suggest a more slowly decaying temperature front. These profiles begin flatter and only sharply steepen near the shock front. In all simulations, the profile decays more strongly from the REH.

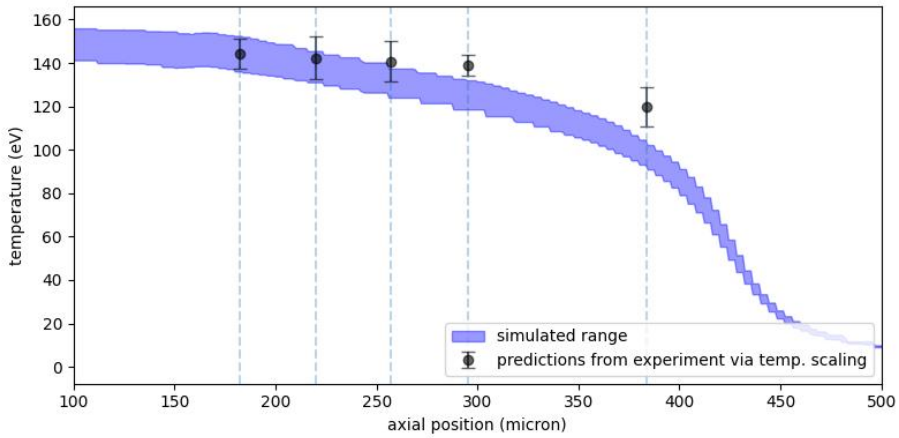

Figure 4.18: Temperature reconstruction of shot 86462 as done in the manner of Fig. 4.16.

4.5.3 Implications for constraining simulation parameters

We have demonstrated that radiography analysis can constrain the inner and outer densities, and most consequentially, the laser powers needed to reproduce shock feature curvature in each shot simulation. Furthermore, the predictions in this analysis produce simulated hohlraum fluxes that match reasonably well to the Dante measurements. Nonetheless, the

range of possible parameters in the temperature profile reconstruction fall short in predicting the spectra. We briefly discuss the implications of the forward modeling process on quantification of the spectra, namely using simulated radiography and simulated hohlraum flux, and the reverse process, how we can use spectra via the temperature reconstruction to understand needed physical improvements.

Clearly our analysis indicates that laser drive with our current hohlraum choices dominate the spectra. We can certainly increase laser power in our simulations, or change for example, opacity multipliers in our hohlraum simulations to produce hotter temperature profiles. However, a consequence is overdriving the shock in our simulations, as well as producing unrealistically hotter flux from the hohlraum and near the hohlraum REH into the target. Fig. 4.16 and Fig. 4.18 demonstrate this effect, that our hottest models may be over predicting temperatures at positions nearer the hohlraum. Furthermore, Fig. 4.16 demonstrates a more chaotic profile for the hottest simulations, resulting from hohlraum material being injected coaxially. This prediction is considered unphysical, as there is no radiography evidence to suggest such strong material injection. Finally, the nature of the flux entering the target are dictated by the hohlraum modeling choices in this work, and higher laser power may drive more oblique shocks into the Be tube walls, yielding a reflected shock with a shape that disagrees with the radiography.

One suggestion in the temperature reconstruction analysis is that the temperature profile would be a high quality reproduction of the experimentally inferred temperature if the simulated profiles were spatially shifted forward, approximately 40-80 microns. Such a large physical discrepancy is dubious due to our confidence in metrology and calibration. However, more suggestive of this shift is that the simulated temperature gradients decay more quickly towards the wave front and is potentially too hot in positions nearer the hohlraum.

An unlikely source of error is that our hohlraum models cool too quickly, potentially 0.2 to 0.3 ns faster than inferred Dante measurements (evidenced by Fig. 4.10). Simulations studied in detail here fix the pulse duration modifying only laser power. The effect of modifying the pulse duration (shortening or extending the pulse width) would emulate faster or slower cooling, respectively, by nearly 0.2-0.3 ns from peak (Section 4.6.3). However, we observed minimal change, in both shock position or shock temperature from such an adjustment to simulations. Furthermore, as our simulated fluxes do reasonably match later time predictions from the available and reliable Dante data, we do not expect a significant deviation in the temperature profile from late time cooling data. The temperature recon-

struction of our earliest spectral measurement for shot 86462 (Fig. 4.18) demonstrates that even at early times of 2.2 ns, our models underestimate the temperature nearest the shock front by approximately 12 eV.

A potentially large source of uncertainty is the equation of state. Fryer et al. argues that for regimes modeled in the Pleiades experiment, that uncertainty is dominated by how equation of states model electronic excitation and ionization, and consequently the specific heats used in internal energy calculations [46]. In their work, they found that their standard SESAME equation of state under-predicted breakout times (radiation flux escaping the end of the foam cylinder) by 6-10%. We expect that such uncertainties may be present in our experiment as well, as our models employ similar SESAME equations of state for our foams and access similar physical regimes as the Pleiades experiment.

4.6 Other model effects

4.6.1 The effect of outer (undoped) foam density and laser power on the shock profile and spectra

Fig. 4.19 shows a simulation set with outer foam density ranging within $\pm 2\sigma$ (58.3 to $75.1\,\mathrm{mg\,cm^{-3}}$), a fixed laser power, and a fixed inner foam density. In this demonstration, all of the shock positions fall within the symmetrized error bounds, however, visibly the -1σ outer density change suggests a best fit for curvature. Furthermore, simulations predict that the effective shock position in the inner foam is not a function of outer foam density.

Another constraint in density matching for the outer foam is the position of the inflow from the Be wall into the outer foam. Fig. 4.20 shows the experimental wall shock in blue and the simulated shock in orange, overlaid on the simulated radiograph. As the outer foam density is decreased, the wall shock propagates further into the target. Only nominal density (0σ) approximately captures the experimental shock contour. A likely source of error could arise from the flux entering the target into the hohlraum in simulations – the Dante x-ray measurements are only able to infer flux exiting the target. The spatial, angular, and frequency distributions of the flux entering the target are able to alter how the shock evolution occurs in the outer foams as well as into the Be wall.

While the lower density cases produce a reflected shock that travels further back into

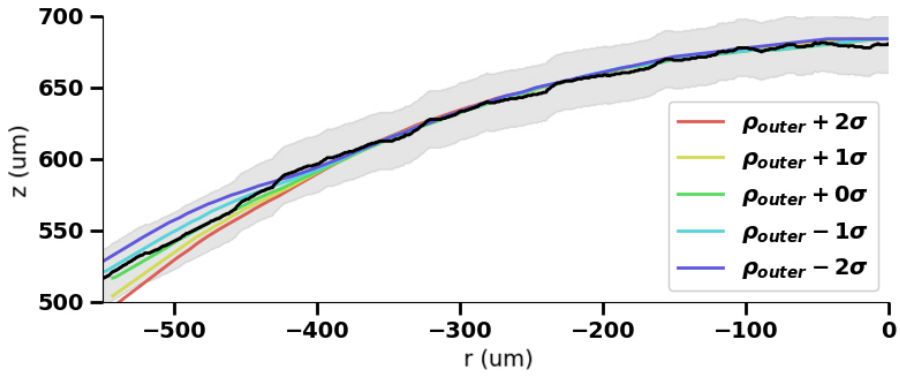

Figure 4.19: Changing the outer foam density within 2σ does not affect the shock curvature or position in the inner foam, but may produce a shock spanning over 40 microns at the outer edges. At the $x = -400\,\mu\mathrm{m}$ position is the inner and outer foam boundary.

the outer foam, the point where the primary shock meets the beryllium wall may be approximately $y = 450\ \mu\mathrm{m}$ in the case of -2σ, but may be $y = 400\ \mu\mathrm{m}$ in the case of $+2\sigma$. In future work, we will need to consider more closely such details when constraining outer density from the wall shock contour.

Due the wide range of outer foam densities, simulations suggest a large temperature and density gradient at any given radial lineout position that crosses the shock in the outer foam. Regardless, this gradient bears virtually no effect on the spectra. Additionally, the Be wall contributes no noticeable transmission signature and the system heats little beryllium in the wall shock.

4.6.2 Continuum removal from the transmission

The removal of continuum requires dividing the raw transmission by the estimated continuum fit found by ACOFI. However, the continuum fit may also have difficulty predicting the correct continuum near the boundaries of low signal. In Figure 4.21, we show the standard ACOFI fit, in addition to fit estimates if we consider all points shifted by $\pm\sigma$ in the transmission. While the continuum fit is our best estimate, if our fits under- or over-estimate the continuum range near the spectral features, the transmission may have a slight skew that cause more error in comparisons to synthetic spectra at higher energies. Nonetheless, we expect less than a few percent deviation from mean in transmission peaks at higher energies.

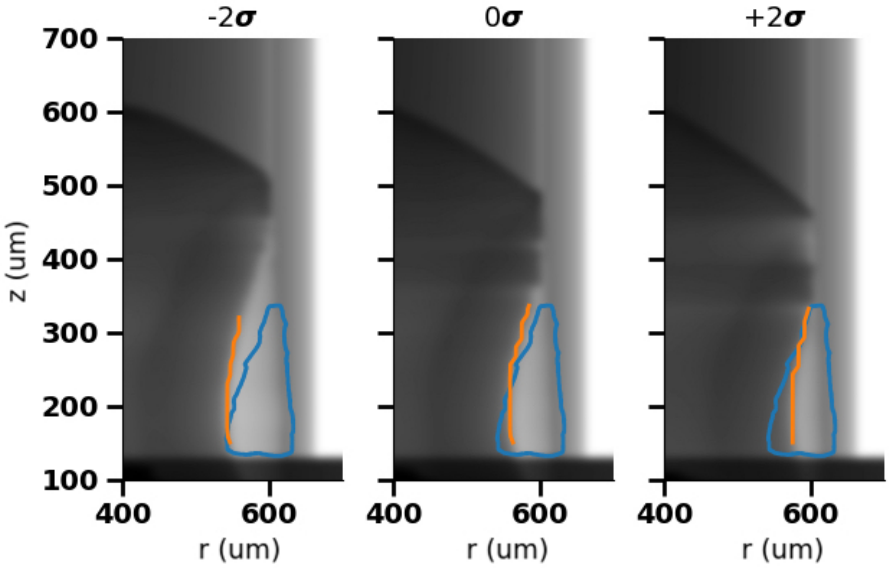

Figure 4.20: The effect of decreasing the outer density from 58.3 to $75.1\,\mathrm{mg\,cm^{-3}}$ on the position and curvature of the simulated wall shock (orange) compared to the experiment (blue) is also significant. Here for shot 86456, the density extrema span roughly 18 microns in peak wall shock position, however, the overall shape is significantly enhanced in the lower density case, exhibiting much stronger curvature.

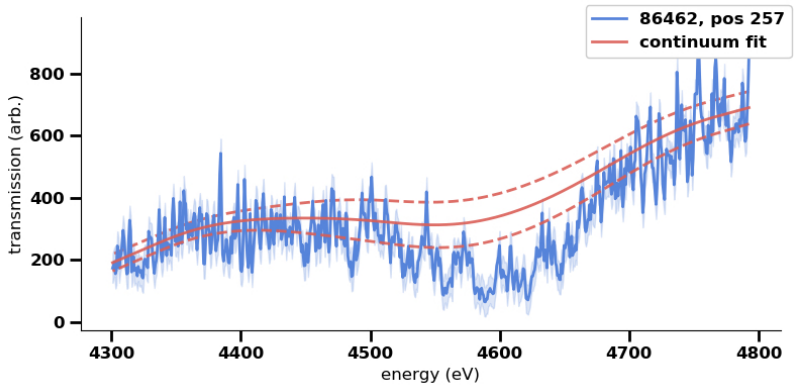

Figure 4.21: ACOFI produces the continuum estimates (red) that we use to remove the continuum and produce transmission values from the intensity (blue). In this example for shot 86462, ACOFI may overestimate the continuum at higher energies near 4700 eV making comparison at higher energy peaks more uncertain.

4.6.3 Effect of pulse energy and duration in simulations

By modifying laser power in simulations we are directly attempting to observe the range of laser energies that reproduce the shock position in the expected error range. We are also indirectly attempting to account for the measured target flux. Comparing between shots still requires laser power adjustments in simulations of up to $\pm$ 10% depending on the timing of the diagnostics. For example a shot 86456 simulation may require 10% more laser power to observe the correct shock position at radiography timing than 86462, despite having similar densities. This 10% may cause the shock position to vary roughly $\pm 20\,\mu\mathrm{m}$ from nominal shock position.

The experimental variability in the laser pulse duration is approximately ± 4 ps, which, in simulations yields minimal change in shock position or temperature. However, in simulations, a laser duration variation of ± 50 ps yields a shock position change of roughly $20\,\mu\mathrm{m}$ at $3.3\,\mathrm{n\,s}$ into the simulation, on par with the reported 10% laser power change above. Even with this extreme variation in laser timing, we observe only 4-5% power variability as seen in Fig. 4.22, well within the estimated upper bounds of 10% as shown in Fig. 4.9. Thus it may be possible to eliminate laser duration variability as a modeling parameter.

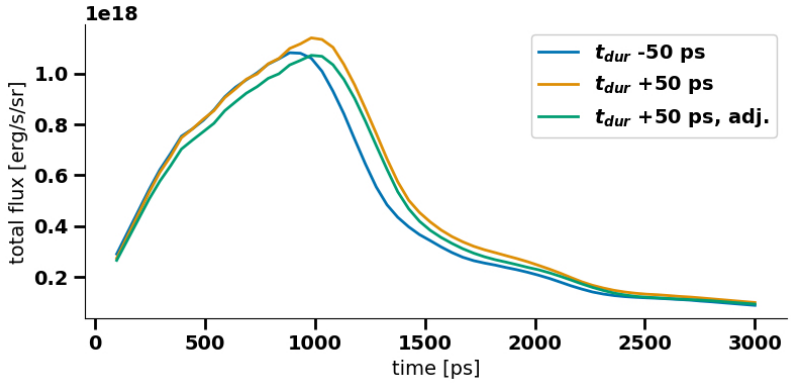

Figure 4.22: Changing the pulse duration to within 1σ and accordingly the laser power produces little more than 5% variation in the total simulated flux.

4.7 Conclusion and Discussion

In this work we use state-of-the-art simulation tools Cassio integrated with implicit Monte Carlo to model the COAX experiment in 2D, using both LTE and tabular nLTE models for the opacities and emissivities in the hohlraum. The primary goal is to assess the constrain-

ing capabilities for each diagnostic in the experiment: a Dante x-ray diagnostic for flux information from the hohlraum LEH, a radiography diagnostic for positional information about the shocks and flow features in our system, and a novel spectral temperature diagnostic that enables a spectral comparison between experimental and synthetic spectra from our simulations.

First, we find that radiography is our most robust tool, yielding a wealth of constraining information in the numerous features identified in Section 3. As the starting place for tuning simulations, we are able to match the position and curvature for our shots while identifying constraints on the inner and outer densities. Analysis of the radiography and shock dynamics detail other important physics, namely that the curvature is largely a function of the contrast ratio between the inner and outer foam densities and that the reflected wall shock can help constrain the outer foam density.

Changes in outer foam density do not have an effect on spectra nor does it affect the shock position in the inner foam. The wall shock position is most sensitive to a change in outer foam density and can help constrain the outer density. High quality data is required out to both integrated wall edges in the radiograph. As such, in future analysis the wall shock curvature can be a useful constraint on simulation parameters.

Inner foam density changes can alter the shock curvature in the outer foam, both with and without changes in the laser drive. However, for a given inner density and laser energy pair, simulations may produce a shock with functionally identical position and curvature in the inner foam. Thus it is the curvature in the outer foam that most strongly constrains density uncertainties. This is evidenced by shot 86462, where lack of an outer foam shock position leaves a high uncertainty in the inner foam density after the curvature minimization analysis. Combined with the outer density discoveries, this identifies the contrast ratio as the most important factor for determining the primary shock curvature. For a given simulation set, the best curvature fit is chosen by minimizing the slope of a least-squares fit to the error difference between a simulated shock position and the symmetrized, mean experimental shock position whose error bounds are approximately $\pm 25 \mu\mathrm{m}$. We find that for all shocks, we can reasonably expect no more than $\pm 1\sigma$ in density, with preference to higher density in the outer foam ($+\sigma$).

All of our models compare favorably to the integrated flux, but are likely to fall outside of the 10% power variability predicted by FIDUCIA unfoldings. We find that our LTE

and nLTE nominal models with one sigma in density variation may produce flux variations within 14% and our two sigma model extremes can produce a peak flux with a 30% variation. However, due to lack of reliable data after 1.2 ns when the hohlraum cools we suggest that the Dante x-ray diagnostic discussed in Section 4 may be our most qualitative tool. We nonetheless argue minimal effect of late-time cooling on the temperature profile.

Finally in Section 5, we argue that the spectral diagnostic is our most revealing tool. As we have shown that transmission data is largely insensitive to changes in density, the spectral diagnostic is capable of directly constraining the temperature profile of our models. We have shown that our models compare well with the temperatures nearer the hohlraum, but typically underpredict temperatures at lineout positions close to the shock front by as much as 20 eV. The reasons this may occur include transport not correctly capturing the thermalization of plasma between the shock front and radiation front, spatial discretization errors in the radiation solve, hohlraum and drive modeling errors, and other modeling uncertainties such as equation of state. Furthermore, in this work we considered integrated flux in the Dante comparison. Getting the correct ratio of M-band flux may be difficult and may involve detailed nLTE effects. In future work we will continue to explore these considerations.

CHAPTER 5

Probing the Collision of Supersonic Radiation Waves and Radiative Shocks in the Radishock Experiment

5.1 Introduction

Radiation flows and shocks are fundamentally important phenomenon in many high-energy density physics (HEDP) settings such as experiments in ICF, astrophysics, and HEDP laboratory experiments. In the laboratory, radiation waves may provide sustained radiation environments and alongside shocks, serve as drivers for a variety of physical phenomenon. The propagation of these waves has been the focus of intense study for the past several decades, in both the laboratory, e.g. [144, 49, 48] and in astrophysics. Applications in astrophysics include strongly to weakly coupled regions including the energy deposition in Stromgren spheres [145], radiatively-driven winds focusing on momentum deposition [146, 147] and conditions in between where both energy and momentum coupling are critical such as shock breakout [8].

The nature of sufficiently hot shocks in high-energy density environments can be characterized in two ways [148]. The first depends on the importance of the radiation flux compared to the material flux, and systems in which the radiation flux becomes comparable to or exceeds the material flux are said to be flux-dominated. For typical low-density foams below 100 mg cm^{-3}, this is easily accessible in the laboratory by driving shocks on order of tens of eVs. Furthermore, the structure of the shock is largely dictated by the optical depth, $\tau = \rho\kappa l$ which is the number of mean-free paths of the radiation in a material with some representative density ρ, mean opacity κ, and length scale l. A material whose optical depth $\tau < 1$ is called optically thin and radiation streams easily and through many mean free paths before interaction; it is optically thick if $\tau > 1$, where radiation is

absorbed and re-radiated many times across the scale l. This identifies four basic types of shock transitions dependent the optical depths of the shocked, downstream material and the unshocked, upstream material into which the shock can effuse radiation [49]. In the Radishock experiment described in this work, the $40\,\mathrm{eV}$ shock generated is a thick-thin radiative shock with prominent radiation fluxes.

Similarly, the transport of momentum and energy by photons in a media depends on how strongly the radiation and matter are coupled. In simplified models of radiation waves, it is useful to consider the ratio of the radiation energy flux of a blackbody plasma, $F_{rad} = \sigma T^4$ where σ is the Stefan-Boltzmann constant and T is the temperature of the plasma, and the material energy flux $F_{mat} = \epsilon \rho c_s$, where ϵ is the specific internal energy and c_s is the sound speed of the material. In situations where the radiation flux exceeds the material flux, the plasma is said to be radiation-dominated. Typical radiation-dominated cases in HEDP are found in temperatures exceeding $100\,\mathrm{eV}$ in low-density foams and environments below $100\,\mathrm{mg\,cm^{-3}}$. Radishock generates radiation waves of $140\,\mathrm{eV}$ into a foam of density $55\,\mathrm{mg\,cm^{-3}}$. Additionally in a seminal analytical work, Marshak employed a Mach number to describe supersonic flows (wave exceeds the material sound speed; no material flux generated) to a subsonic (wave approaches material sound speed; material fluxes become important) [34]. In many cases, the radiation wave may even form a shock, as rising material fluxes near the wave front may pile up and quickly steepen into a shock, e.g. in the COAX experiment [46, 47]. Radishock employs a radiation wave which is supersonic throughout the experiment.

When supersonic radiation waves meet radiation-dominated shocks, the resulting interaction leads to a spike in energy-density, corresponding to an increase in temperature. The Radishock experiment is the first experiment seeking to characterize the direct, head-on interaction of the wave and shock fronts, to develop preliminary theory behind their interaction, and confirm numerical models using state-of-the-art radiation hydrodynamics simulations. This work is a first look at this phenomenon and the ongoing design of the experiment, combining experimental, theoretical, and numerical aspects of the problem.

Radishock is a laser-driven, high energy density physics experiment that builds from the COAX platform and leverages our uncertainty quantification work and growing analysis of the spectral diagnostic [121, 136, 5, 47]. In Radishock, the supersonic radiation wave is driven into a uniform, low-density, doped foam and this wave collides with a counter-propagating shock. The primary goal of the experiment is to identify the conditions before

the collision: the state and spatial characteristics of the shock and radiation wave; during early collision: when the head-on interaction of the wave and shock produces a strong, localized temperature spike; during intermediate evolution of the spike: when the shock dissipates through the wave and the radiation wave rapidly becomes subsonic, generating a dense front; and late interaction: when a strong temperature slope inversion occurs in the cooling region ahead of the interaction. To understand how the interaction changes the development of the radiation flow and the shock over time, we collect data on experiments featuring only a radiation wave (indirect, hohlraum drive only), only a shock (direct, ablator drive only), and the interaction between the shock and wave (both drives).

As in the predecessor experiment COAX, we employ three diagnostics and conduct our experiments at the Omega-60 laser facility. A Dante x-ray diagnostic measures the radiation fluence exiting the hohlraum and is used to qualitatively verify reasonable simulated fluxes from the laser-hohlraum modeling efforts in simulations of the experiment. Analyzed experiments in this work use the same hohlraum drive configuration from COAX [5, 47]. A radiography diagnostic images dense features in the experiment, providing a useful benchmark of the expected shock position between experiment and simulation and helps to constrain the laser power modeled in simulations. Finally, an absorption spectroscopy diagnostic delivers transmission data through axial lineouts along the target. With the analysis developed in [47], we can not only directly compare synthetic transmission to experimental, but also reconstruct the temperature profiles to understand how accurately our computational and experimental models agree. In this work, we focus on radiography and spectra, with emphasis on detecting the spike and characterizing the interaction.

In Section 5.2, we describe the design of the experiment and the diagnostics that provide shock and interaction information via radiography and spatial temperature information via absorption spectroscopy, briefly summarizing the tools needed to extract the information from these diagnostics. Section 5.3 presents simulations of the experiments and demonstrates some new theory on how the interaction evolves spatiotemporally. We use an example (the "nominal") simulation to detail the primary physics involved and how we can spectrally identify the interaction feature, linking the experimental and simulation efforts; additionally, in this section we look at how parameter variability and experimental uncertainty may affect the detectability. Section 5.4 then presents some direct comparisons between the simulation suite and available experimental data, testing our ability to detect the interaction. We provide discussion into future work and improvement in 5.5 and finally summarize the work in 5.6.

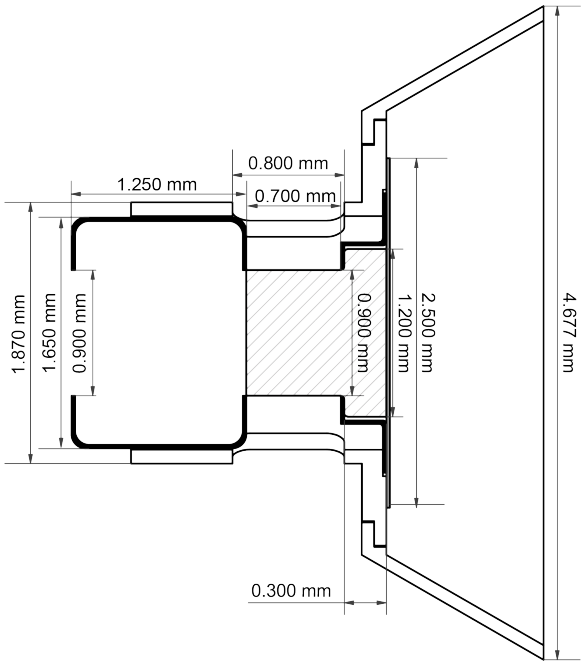

Figure 5.1: The experimental target diagram showing the hohlraum (left side), the foam (center, hatched), and the ablator assembly (right side).

5.2 Experimental design and analysis

We employ a radiation-tube design, building on the COAX platform [5]. Schematically depicted in Figure 5.1 the target consists of a cylindrical plastic tube linking a vacuum hohlraum and a beryllium ablator. Between the hohlraum and the ablator is a Ti-laden aerogel foam ($TiSi_5O_{12}$) represented as the lightly hatched center region. A cylindrical plastic tube surrounds the foam and is structural. The ablator side (right side) of the target is a gold clipper, which acts as a wave-shaper to reduce the curvature shock from the directly-driven beryllium.

This platform leverages the diagnostic and experimental approach used for the COAX platform [5], but unlike the platform in COAX, the target used in the radiation-shock interaction experiment is driven from two sides and we use a single, uniformly doped foam. The Be ablator is directly-driven 4 ns prior to the indirect-drive of the hohlraum. The 4 ns timing offset is set to capture in interection in the field of view. Point projection X-ray absorption spectroscopy is fielded perpendicular to the target axis, using a Kr-filled capsule backlighter. The laser pulses were chosen to keep the indirectly-driven radiation wave supersonic in the entire length of the field of view. The target and laser pulses are designed to capture the interaction between the direct-drive shock and the indirect-drive hohlraum in

the field of view of the spectroscopy and the radiography.

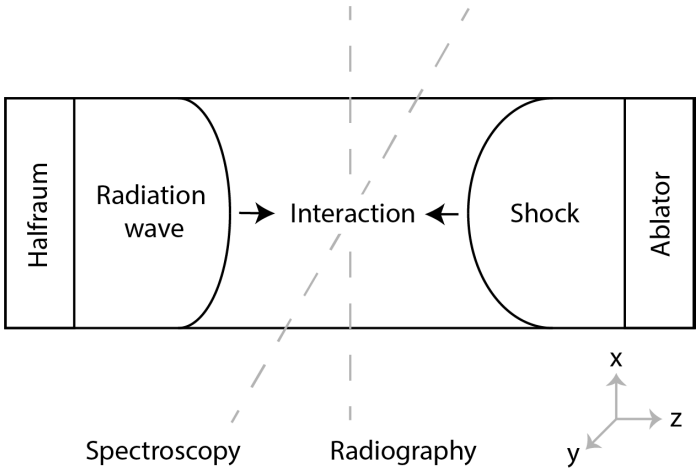

Figure 5.2: A simplification of the target diagram, showing the spectroscopy and radiography diagnostics fielded perpendicular to target axis to characterize the interaction of the radiation wave emanating from the hohlruam and the counterpropagating shock emanating the ablator. All simulation plots showing state variables use this directionality of the propagating waves.

Imaging and streak spectroscopy are used to characterize the size and spectrum of the capsule backlighter. The Kr-filled backlighter capule is driven with more beams. Radiography is subsequently fielded perpendicular to the drive-axis using pinhole-apertured V-foil backlighter and a close-in ported snout tip. For additional diagnostic details refer to [5].

To determine experimental radiography features, we use XRIPL [139]. XRIPL uses median and morphological filters for denoising, divides out a pseudo-flatfield to remove large scale lighting differences and retain fine-scale differences in contrast, and watershed segmentation to identify shock and Be inflow contours [139]. The experimental spectra is processed in IDL and the continuum is fit with ACOFI (automated continuum fitter), which uses an asymmetric least-squares fitting method that has been specially adapted to the problem of continuum fitting in absorption spectra [142]. ACOFI outputs the absorption transmission, calculated as the detected signal divided by the original backlighter signal, e.g. $T = I/I_0$.

In addition to the interaction shots, additional indirect- drive only (hohlraum-only) and direct drive only (ablator-only) were fielded to provide additional modeling constraints and verify the simulated behavior. The experiments are conducted at a wide variety of tim-

ings, staggered so that radiography information from one set of experiments may be used to compare directly to another set of experiments with spectroscopy conducted at roughly the same time. The full summary of shots analyzed in this work is presented later in Table 5.1 of Section 5.4, with shot numbers, diagnostic timings, densities, and other relevant information.

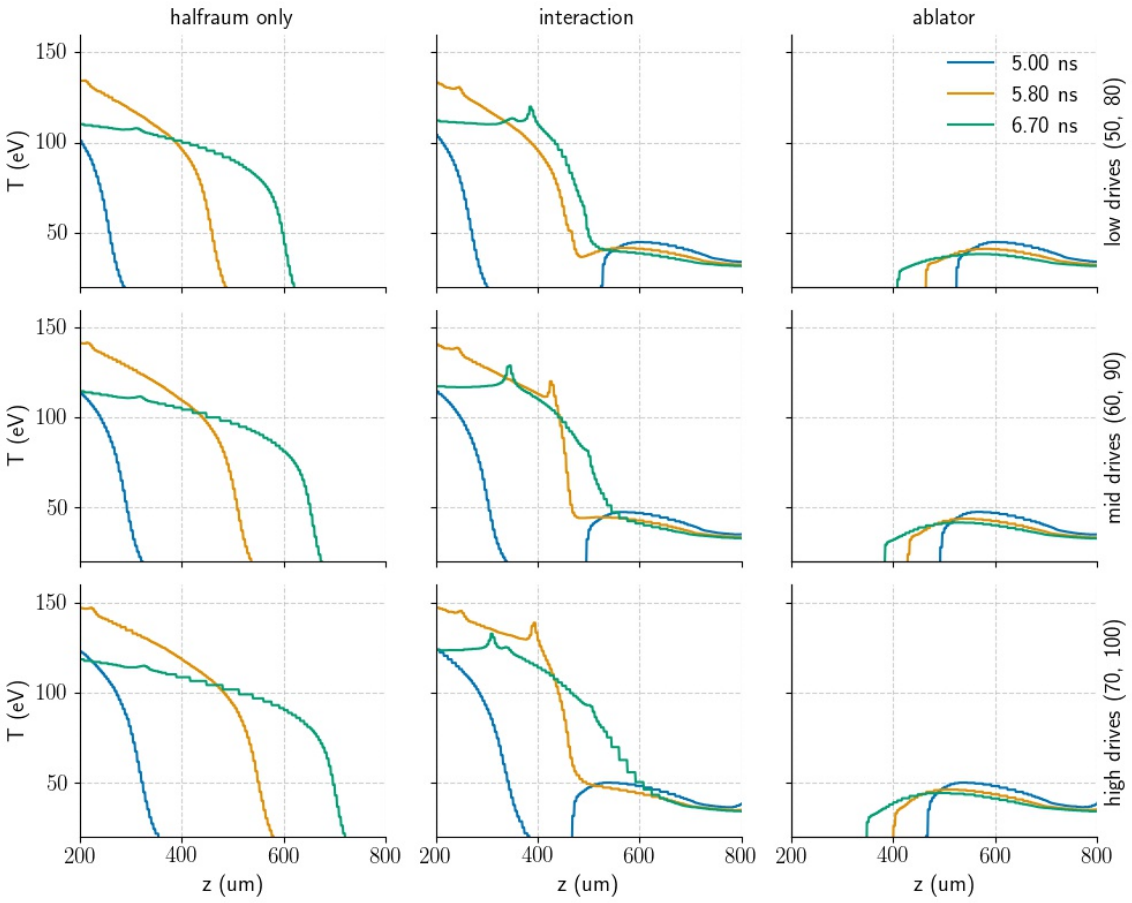

Figure 5.3: Simulations showing the temperature of the waves in the experiment, considered for the nominal experiment with a 57 $\mathrm{mg\,cm^{-3}}$ foam. Each row corresponds to a laser-drive configuration for the halfraum and ablator drive scaling percentages. The first row is a configuration using the least-power, with 50% of the total halfraum power and 80% for the ablator power. The second row is the nominal configuration, with 60% and 90% respectively. Finally, the bottom row is the highest drive with 70% and 100%, respectively. All demonstrate the same qualitative behavior, but with a delay or advance in the interaction timing. Interestingly, for the interactions considered, these simulations demonstrate that the spike feature has consistent characteristics such as peak amplitude relative to the background temperature of the radiation wave ahead of the interaction. We note that this spike is likely to be hotter and much narrower than simulated – see Section 5.3.2 for more details.

5.3 Modeling the Radishock experiment

Simulations of the Radishock experiment use the Eulerian radiation-hydrodynamics code Cassio developed by Los Alamos National Laboratory. The Cassio code is a version of the xRage code [53] that includes several advanced solvers, such as those coupling of radiation and matter by solving the radiation transport equations with implicit Monte Carlo [149, 130] and the integration of the ray-tracing lazer package Mazinisin developed by Laboratory for Laser Energetics [128, 129, 150]. As in modeling for COAX [47], to enable successful use of the laser-modeling package, we use three-temperature models for the ion, electron, and radiation species, as well as electron ion heat conduction. Similarly SESAME equations of state information for each species and the opacity microphysics are modeled by the TOPS codes [56, 70]. The reader is referred to [47] for a more detailed description of the modeling physics.

All simulations explored in this work model the problem in 2D cylindrical geometry, using adaptive mesh refinement to capture detailed physics at the smallest resolution of $4\,\mu\mathrm{m}$. For reference the fronts of the shocks and radiation waves span $40\,\mu\mathrm{m}$ to $80\,\mu\mathrm{m}$, typically allowing a few tens of cells to approximate the fronts.

For comparing spectral results, we produce simulated transmission spectra using a radiation ray-trace code, here observing negligible self-emission and assuming all radiation scattered out of the line-of-site is lost. Our spectra modeling for the Radishock experiment includes a number of improvements over previous techniques such as those used by the SPECTRUM code in earlier work [46, 121, 136], namely capabilities for full 3D ray-traces with arbitrary ray paths and arbitrary source, detector, and target geometries.

Here for our 2D Radishock simulations observing cylindrical symmetry, we map 3D ray distributions by projection onto the 2D data plane when needed. We assume a uniform, monochromatic planar source that is plane-parallel to the detector plane. The detector plane has a pixel resolution of 2 um by 2 um to ensure that the rays can integrate through the minimum resolution of 4 um in the AMR grid. The ray path itself also has 2 um linear resolution. Once the ray trace is performed to determine coordinates in the data plane, a k-d tree data structure performs a look-up for corresponding state values at those coordinates [151]. Finally, we calculate the transmission by integrating through the linearly-interpolated optical path and performing a Gaussian filter to emulate the diagnostic response. This process ensures convergence for the spectra produced, typically calculating around 100-250 ray

integrations for each time and measurement position. Unless stated otherwise for more specific studies, we average the spectra to a single point (the measurement position), integrating over a $20\,\mu\mathrm{m}$ by $8\,\mu\mathrm{m}$ region centered at that point, and thereby emulating the averaging for a measurement position in an experimental spectral position. This models the spatial binning and averaging to a single line position as performed in the experimental analysis. The opacities are calculated from TOPS [70], using a full monochromatic opacities, at roughly 10000 energies binned from $3500\,\mathrm{eV}$ to $5500\,\mathrm{eV}$. For the titanium dopant in our current configuration, the $1s-2p$ transitions of interest span between roughly $4500\,\mathrm{eV}$ to $4700\,\mathrm{eV}$ and the $1s-3p$ transitions lie between roughly $4900\,\mathrm{eV}$ to $5400\,\mathrm{eV}$.

As highlighted in recent results from analysis of the COAX experiment [47], the nominal laser drives must be modified to correctly model the experiment and capture correct wave front positions. There we make the assertion that if the fundamental behavior of the wave front is not significanty dependent on the density of the doped foam (e.g. shape and structure), variation in the temperature profile is largely dominated by the drive powers supplied to the target. A higher density, for example, allows more drive power in order to achieve wave front positions comparable to a lower density with a lower drive power. Both will have similar wave density structure yet yield different (hotter or colder) temperature profiles.

In this experiment we consider density variations within $57 \pm 5\ \mathrm{mg\,cm^{-3}}$, hohlraum laser powers of $60 \pm 10\%$ of the experimental hohlraum laser drive profile, and ablator laser drives of $90 \pm 10\%$ of the experimental ablator laser drive profile. Scaling the real-world drive powers down is necessary with current capabilities in drive modeling efforts [150]. We argue similarly here, in Section 5.4, and that such a density range encapsulates the observed diagnostic data from successful experiments. In this suite also, we observe that such minimal variation in the density has less of an effect on the diffusion rates of the radiation wave (the mean free path of the radiation is proportional to density, e.g. $\tau \propto \rho$, and thereby more weakly dependent on our density range). The physics is then arguably dominated and effectively modeled by the described changes in laser powers (in contrast, compare to the changes of up to $6\,\mathrm{mg\,cm^{-3}}$ explored in the COAX analysis needed to encompass expected experimental variation [47]). In future work we will continue to explore experimental variation, but the ranges explored in this work suffices to understand and develop the platform.

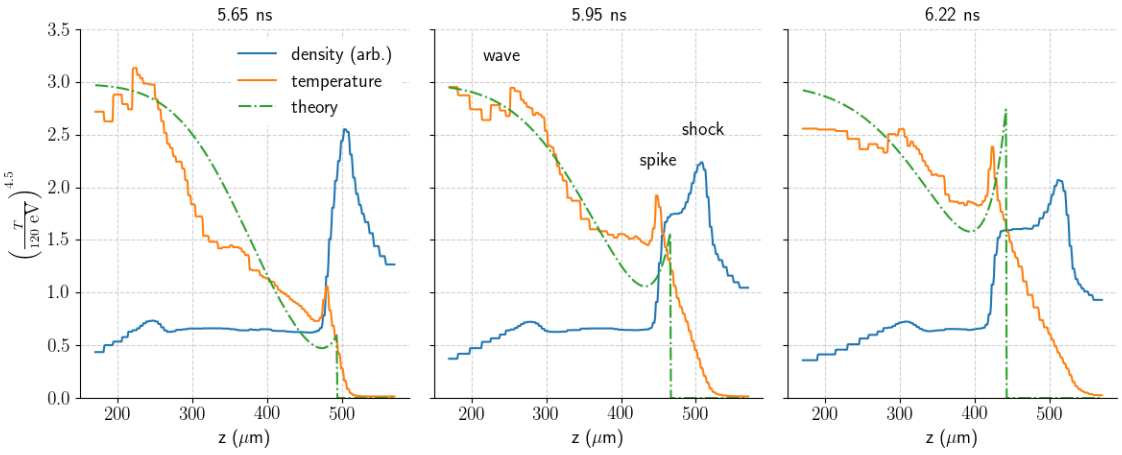

Figure 5.4: Simulations of the nominal experiment and theoretical predictions showing their respective predictions for the behavior of the spike during early interaction. At early times the theory predicts the position and qualitative behavior of the spike, but at later times the more idealized theoretical curves suggest a hotter and faster spike.

5.3.1 Primary physics of shocks interacting with radiation waves

To help understand the following analysis of shocks interacting with radiation waves in the experiment, consider the example simulations shown in Fig. 5.3 showing the temperature of the axial center in hohlraum-only (left column), interaction (middle column), and ablator-only (right column) configurations for low-drive powers (top row: hohlraum power at 50%, ablator at 80%), medium-drives (middle row: 60%, 90%), and high-drive (bottom row: 70%, 100%).

Despite spanning a significant range of temperature differences, the system evolves similarly for all configurations. An ablator drive powers a shock over the first $4\,\mathrm{ns}$, after which the hohlraum drive begins powering a radiation wave that will meet and interact with the shock around $5.2\,\mathrm{ns}$ to $5.8\,\mathrm{ns}$. The shock is $32\,\mathrm{eV}$ to $40\,\mathrm{eV}$ at its steep front (lowest to highest drive), reaching roughly $40\,\mathrm{eV}$ to $50\,\mathrm{eV}$ at peak just prior to first interaction. The supersonic radiation wave diffuses through the tube at speeds of roughly $5 \times 10^7\,\mathrm{cm\,s^{-1}}$ to $8 \times 10^7\,\mathrm{cm\,s^{-1}}$ prior to the interaction, while thermalizing the material upstream from the shock. The waves can be in excess of $120\,\mathrm{eV}$ to $140\,\mathrm{eV}$ nearer the hohlraum, achieving $70\,\mathrm{eV}$ to $90\,\mathrm{eV}$ nearer the wave front (measured near the point of strongest inflection). In early interaction, the shock decelerates from $8 \times 10^6\,\mathrm{cm\,s^{-1}}$ to $5 \times 10^6\,\mathrm{cm\,s^{-1}}$ in the radiation-thermalized material upstream that has sound speeds on order of $1 \times 10^7\,\mathrm{cm\,s^{-1}}$. Thus the shock reaches Mach numbers near 1 and erodes the strong shock front. The result-

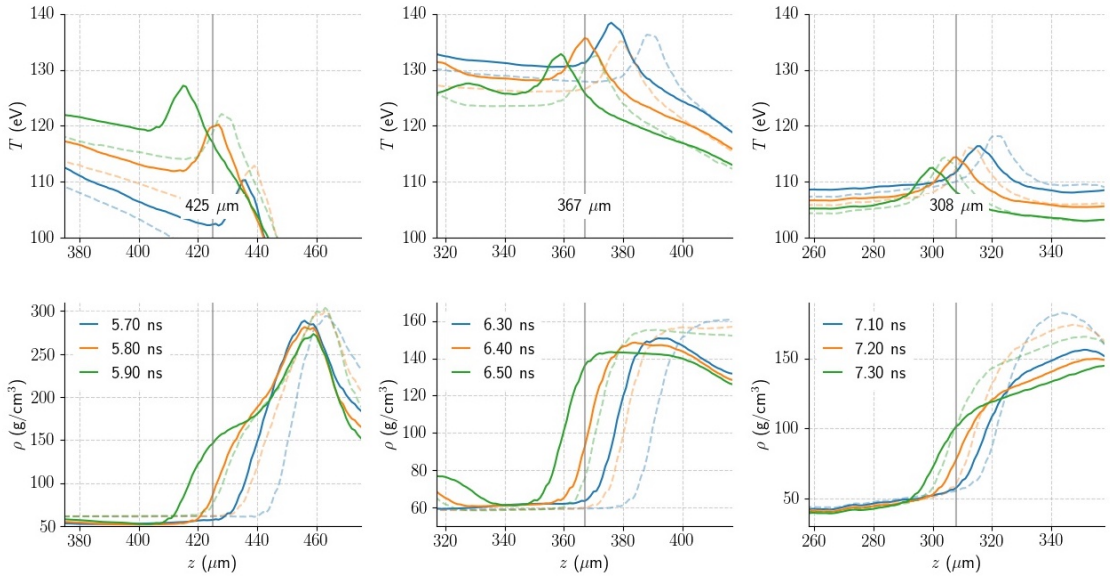

Figure 5.5: In the first row, close-up plots of the spike temperature show the feature evolution over a $200\,\mathrm{ps}$ window centered on times of $5.8\,\mathrm{ns}$, $6.4\,\mathrm{ns}$, and $7.2\,\mathrm{ns}$ of the nominal simulation. Corresponding density plots are in the second row.

ing interaction of the shock and radiation wave forms a matter wave having higher energy density than the local energy density of either wave. Local temperatures at the fronts are approximately a $80\,\mathrm{eV}$ wave front meeting a $35\,\mathrm{eV}$ shock wave.

The system must also account for one or several rarefaction waves emanating from the hohlraum side that can add additional energy to the feature. However the rarefaction is predicted to add only a few eV to the profile, unlikely to be detectable unless the rarefaction wave directly overlaps with the counterpropagating interaction feature.

At later times, for example shown at 8.2 ns, the outflow accelerates again down the rarified density gradient of the radiation wave, again approaching a Mach number of 1 and reforming a shock. In this work, we argue that late time detections are more difficult and uncertain.

A simple analytic model for the structure of the pre-shock radiation field is useful for both interpreting the experimental data and for designing future modifications to the experiment. Modeling the radiating shock as a moving, reflecting boundary condition for the heat equation, we can construct a model of the shock in which the incoming radiation field is reflected by the shock. In reality, of course, the heat is passing into the shock region, and

returned by radiation from the even hotter post-shock region, but by energy balance in the pre-shock region we can expect it to act much as if the reflection scenario is the case. The nonlinear radiation-diffusion heat equation is assumed to be of the form

$$\rho c_V \frac{\partial T}{\partial t} = \boldsymbol{\nabla} \cdot \frac{\kappa_0}{\kappa} \nabla T, \ \kappa \sim T^{-7/2} \tag{5.1}$$

This equation is linearized by introducing the diffusing variable θ, taken to be $\theta = T^{4.5}$, leaving a constant κ_0 for effective diffusion of θ.

The solution for a reflecting moving boundary condition for the heat equation can be found by the method of boosted Laplace transforms [152], and for this particular problem takes the form [153]

$$\begin{aligned}\theta(x,t) = \frac{\theta_0}{2} \Bigg[& \frac{v\sqrt{\kappa_0 t}}{\sqrt{\pi/4}} \exp\left(R v \kappa_0 - \frac{(x+R)^2 \kappa_0}{4t} \right) \\ & + \operatorname{erf}\left((R-x)\sqrt{\frac{\kappa_0}{4t}} \right) \\ & + (1 - v\kappa_0(x+R) + 2v^2\kappa_0 t) \exp\left(v^2 \kappa_0 t - v\kappa_0 x \right) \\ & \times \operatorname{erf}\left((x+R-2vt)\sqrt{\frac{\kappa_0}{4t}} \right) \Bigg].\end{aligned} \tag{5.2}$$

In (5.2), the diffusing variable θ and effective diffusion coefficient/opacity are as discussed above, v is the velocity of the shock, t is the time, and x is the distance from the shock's origin at $t = 0$. The distance from the radiation front and the shock at $t = 0$ is given by R.

Figure 5.4 shows the agreement for θ in the diffusive region between the shock and the rarefaction, which while not perfect, captures a number of features for such a comparatively simple analytic solution. This is expected as this estimate does not correctly model the shock, the detailed flux balance across the shock, or important material fluxes, but it does help provide basic insights into the piling of energy at the shock boundary. These insights include roughly the rate of the rise of the temperature spike at the shock location, and the distance to the temperature minimum where both the incoming and reflected radiation are filling in. Because the model knows only a constant θ_0 to characterize the incoming radiation field, it cannot handle the rise and fall of the actual hohlraum temperature, and both slightly underpredicts early and overpredicts at late time. Further study on models of

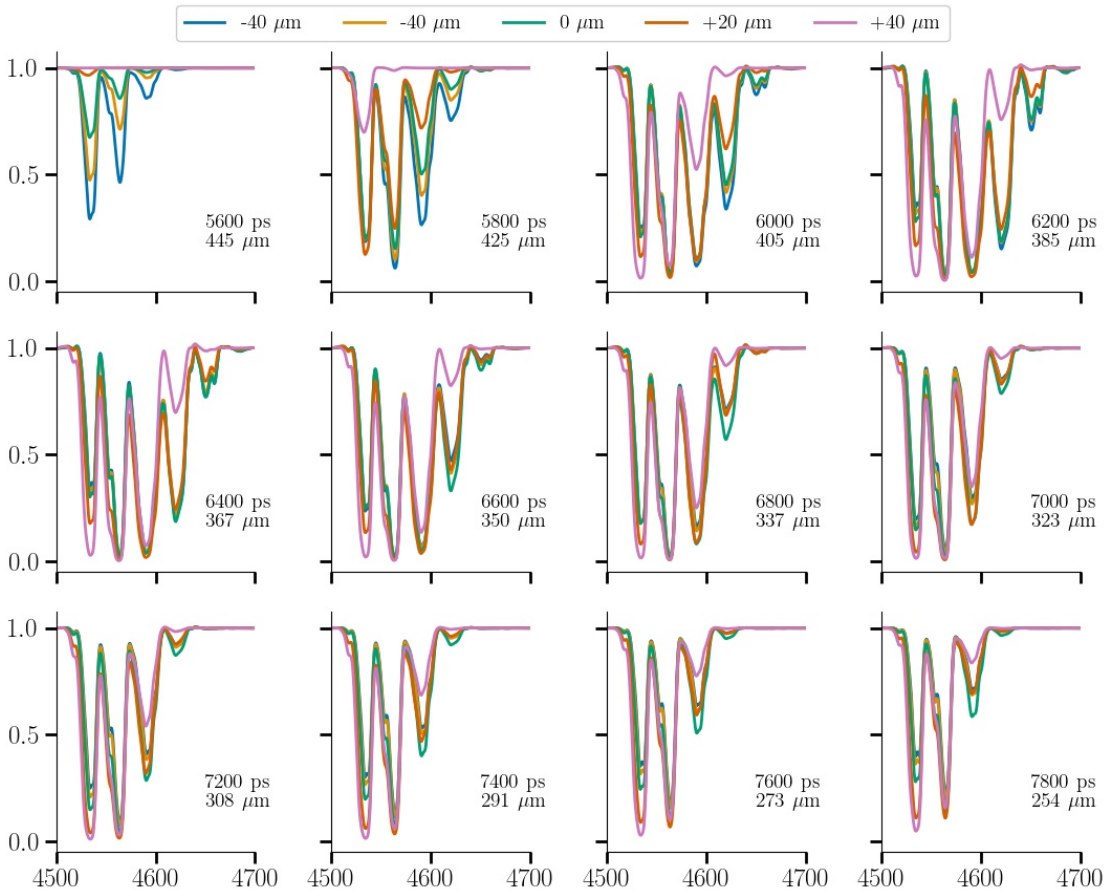

Figure 5.6: A full set of $1s - 2p$ synthetic spectra for the nominal simulation. Each subplot is centered on the middle of the spike feature during the center of the integration window, shown for spectral integration times spanning 5600 ps to 7800 ps. The green line in each subplot is the line centered on the spike annd shown are neighboring lines in $20\,\mu\mathrm{m}$ increments.

this type may provide insight to the nature of energy balance in the radiating shock system, and may constrain observables (such as the spike rise time) in the experiment.

5.3.2 Spectral detection of the spike feature

As both simulation and theory predict that a spike feature forms from the interaction between the radiation wave and counterpropogating shock, we must determine the extent of our capabilities in detecting the feature. In the remainder of this section, we first assess how well the code can model and predict the spike feature's extent and temperature, then look at the interaction signatures in studies to both define detectability and assess the detection quality. For clarity on nomenclature and discussion of results for all the studies: when

referring to spectra or transmission we are referring to the absorption transmission spectra; high transmission indicates less absorption (transmission values closer to one) and thereby integration through cooler or less dense temperatures; a measurement position or lineout is shorthand for a position along the axis where a single spectral measurement is sptially centered; and a line refers to an absorption line at a particular energy corresponding to an ionization stage of the Ti dopant (i.e. high energy lines, or the Ti^{15+} line).

First, we assess the code's ability to model the spike feature. The structure of radiative thick-thin shocks may be described by a three layer model, consisting of an upstream region, a cooling layer, and a downstream, shocked region [148]. The downstream region represents the final, steady state where ion-electron collisions equillibrate temperatures away the shock front. The upstream region determines the initial state, typically having constant density, temperature, and radiation fluxes. The shock traveling into this region will first radiate into and ionize the material upstream and lower its optical depth. However, this radiative precursor typically has a small spatial extent, as is true for the radiative shock in Radishock, having a radiative precursor of 10-20 microns in length.

The cooling layer lies just behind the density jump in which the hottest temperatures are in the ion temperature, produced on a length scale on order of a few ion-ion collision lengths, which then cool radiatively and through electron heat conduction [154]. For reference, this length scale is likely not more than a few nanometers at the temperature and density conditions for the shock through an SiO2 foam in the Radishock experiment. However, the heating of the electrons occurs over a much larger spatial scale – assuming that this scale is on order of a few collisional lengths, this region is not likely larger than one micron. A more refined estimate, emanates from the width of the cooling layer itself, proportional to the optical depth [148, 155]. Radishock may have a cooling layer optical depth of approximately $\tau = 0.1$, so that the spike length is effectively order 1 micron, consistent with the spatial extent of electron heating behind the shock.

Because the code does not refine further than 2 microns in grid resolution, the spike is considerably under-resolved and as such, will not only underestimate the temperature of the spike, but overestimate the spatial extent of the spike. However, because electron heat conduction is stronger upstream in the radiatively heated region upstream of the shock, the spatial scale may be more aptly determined by the local electron collision length just ahead of the shock. Assuming that these collisions are strongest in the precursor region, the spatial extent may be roughly 4 microns in length (one collisional electron mean free

path) during interaction of shock and the much hotter electrons upstream. Thus the code is still likely to overestimate the spatial extent of the spike, by perhaps five times as much, making spectral detection of this narrow feature even more challenging in experiment. The evolution of the spike in a quasi-steady-state flow (when upstream temperatures become more locally constant as the hohlraum cools) may be more complicated to determine, however, the spatial extent of the electron temperature in the spike is still likely to be on order of several microns by these estimates. We can assume for the following analysis, that our estimates provide a best case scenario for spectral detection.

The leftmost column of Figure 5.5 shows a close-up of early interaction at $5.8\,\mathrm{n\,s}$ in the nominal simulation. The spike formation begins approximately $200\,\mathrm{ps}$ earlier and rapidly rises to the local ambient temperature of the radiation wave front near $440\,\mu\mathrm{m}$. Each line represents the temporal start, middle, and end of the spectral integration window. Just prior to the interaction, the shock wave has a peak density of $300\,\mathrm{mg\,cm^{-3}}$, indicating a strong shock at a compression ratio of roughly 5.5. The strong shock has not yet fully weakened by the initial interaction, but the density at the shock front drops to $150\,\mathrm{mg\,cm^{-3}}$ over the next $600\,\mathrm{ps}$, and remains at this density throughout the propogation of the interaction feature, as shown in the density plots in the bottom row. The interaction is effectively an ablative process, with the radiative heating of the dense front eroding the front.

We provide Figure 5.6 for reference of the $1s-2p$ transmission of the spike in the nominal simulation, at all relevant times through the evolution of the interaction. This figure provides the rubric for a spectral comparison of the interaction between experiment and the ideal simulation. In this comparison, while a suitable hohlraum-only shot may not be directly applicable (due to potentially significant shot-to-shot variation), the synthetic spectra will be compared against hohlraum-only versions to observe feature evolution unique to the interaction.

Referring to Figure 5.6, at $5.8\,\mathrm{n\,s}$ in the early interaction, the $1s-2p$ spectra indicates that a spike in temperature is not singularly detectable, instead appearing as a steady decrease in integrated temperature. This means that interaction feature at any time in early interaction (e.g. the green line indicating spike center) has not achieved prominence above the ambient radiation wave temperatures at preceding integration times (e.g. neighboring lines at $\pm\,20\,\mu\mathrm{m}$ to $\pm\,40\,\mu\mathrm{m}$). While not shown, this behavior is also strongly indicated in analysis of synthetic $1s-3p$ spectra which is often deemed to be too experimentally noisy or narrow to be useful for careful analysis.

By $6.4\,\mathrm{n\,s}$, the temperature profile has begun to flatten due to the cooling drive source, as evidenced in Figure 5.5. At this point in the evolution, the interaction feature is able to achieve prominence above the wave temperature at earlier integration times, however, the temperature profile may not yet be locally flat enough to ensure that integration will detect a significant amount of the temperature spike at the interaction front. There are two modifications to this behavior that may make early time interactions more readily observable. First, a faster radiation or shock wave front can easily shift this by around $400\,\mathrm{ps}$ as witnessed in the high-power simulations at lowest density (see Subsection 5.3.4). Second, simulations may under-predict the degree of heating in the temperature spike as suggested by the theoretical model in Figure 5.4 – hotter spike temperatures will achieve greater prominence above local wave temperatures during integration.

We note that at $6.4\,\mathrm{n\,s}$, a rarefaction wave from heated material has yet to reach the interaction feature which will enhance the spike temperature (see slight temperature bump in the green curve of the top row, middle column of Figure 5.5. The 1s-2p spectra shows nearly indiscernible spectral features for the nominal spike position of $385\,\mu\mathrm{m}$ (orange line in spectra) at $6.2\,\mathrm{n\,s}$ and its neighboring positions $\pm\,20\,\mu\mathrm{m}$ as evident in Figure 5.6. However, despite not having a singularly detectable transmission line, we can still qualify this as a detection in synthetic spectra due to the specific evolution of spectra lines.

Beyond roughly $6.4\,\mathrm{n\,s}$ to $6.6\,\mathrm{n\,s}$ in this nominal case, the spike will always travel into lower temperatures towards the cooling hohlraum. This signals that the temperature spike will always be hotter than both the ambient local temperature behind it as well as the temperature ahead of it. This is demonstrated at plots for the simulation at $7.2\,\mathrm{n\,s}$ in Figure 5.5. Finally we observe ideal behavior in the higher energy peaks in the spectra due to integration through the hotter spike: prominent, singularly detectable lines (orange), showing successively higher transmission lines for neighboring measurement positions.

The interaction feature travels at approximately $100\,\mu\mathrm{m\,n^{-1}\,s}$, so during the spectral integration window it will have traveled roughly $20\,\mu\mathrm{m}$. The reason that the feature is able to travel faster than the initial shock speed is due to the addition of momentum from the ablative heating of the shock front. As the spike progresses into the lineout position, spectroscopy will integrate through denser material, apparent in Figure 5.5. Fortunately, due to both slight curvature of the feature and that the feature has a spatial extent of approximately $200\,\mu\mathrm{m}$ in diameter, lineouts near the spike nominal position ($\pm\,20\,\mu\mathrm{m}$) should show sim-

ilar transmission. This is evidenced by the highest energy transmission lines in the orange and red lines of Figure 5.6. We can therefore define late detection as an increase in the prominence of transmission lines in the vicinity of a predicted spike.

5.3.3 Radiographic detection of the spike structure

The radiation wave not only erodes the shock front through ablative heating, but will also propogate through the front, rapidly become subsonic, and pile material at the front of the subsonic transmitted wave. This occurs because the density is over 3 times higher than the ambient density, greatly reducing the mean-free path of the radiation. The corresponding flow structure will produce dense fronts that are unique signatures to the interaction and do not occur in ablator-only or hohlraum-only shots. Figure 5.7 shows this density structure along the axial center for the nominal simulation. In the case of $7\,\mathrm{ns}$ (green curve), we can clearly see the dense front of the left-traveling ablated shock, a less dense plateau, and finally the right-traveling dense front resulting from the subsonic transmitted wave.

These dense regions are imageable in radiography and provide another data comparison point. While the position of these dense regions are dependent on the velocities of the waves and thereby the drives and density of the foam, we find that they are consistent in the parameter space explored. For example, the relative distance of the transmitted wave front at peak density and the eroded shock front at peak density remains nearly the same with varying ablator laser power but will change largely with varying hohlraum laser power. This is measured from the onset of interaction.

5.3.4 Assessing experimental variability and other uncertainties

Within the variability explored in the simulation space, the interaction spike also evolves similarly, as seen in Figure 5.8. This plot shows the temperature evolution of the peak of the feature (solid line) compared to the range of temperatures neighboring the spike in a $20\,\mu\mathrm{m}$ by $20\,\mu\mathrm{m}$ region (shaded). This region is chosen to emulate spectral integration. The temperatures reach roughly $125\,\mathrm{eV}$ at peak of the weakest-driven simulation ($\rho = 62\,\mathrm{mg\,cm^{-3}}$, ablator 80%, hohlraum 50%) vs. a $155\,\mathrm{eV}$ peak in the strongest-driven simulation ($\rho = 52\,\mathrm{mg\,cm^{-3}}$, ablator 100%, hohlraum 70%). The simulation suggest a fairly rapid rise time $400\,\mathrm{ps}$ to $800\,\mathrm{ps}$ before steadily remaining at peak for $300\,\mathrm{ps}$ to $500\,\mathrm{ps}$ and then decaying for the rest of the interaction. Comparing the temperature of the spike against the ambient integrated temperatures, we consistently predict that the spike is approximately $7\,\mathrm{eV}$ to $10\,\mathrm{eV}$ hotter than ambient temperature. All cases predict this evolution and the re-

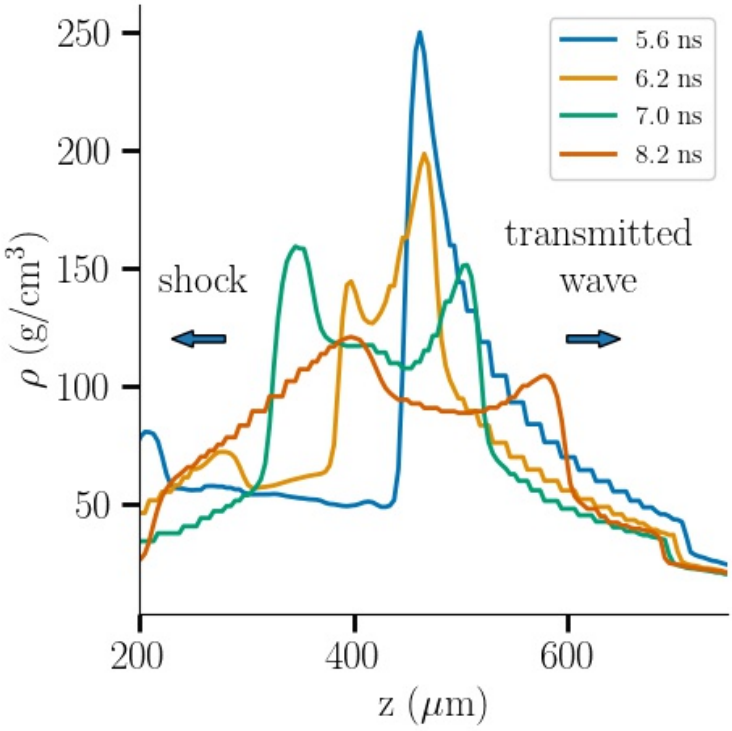

Figure 5.7: Across the simulation suite, the behavior of the spike is consistent. The top subplot shows the temperature of the spike (solid) and the range of temperatures that surround the spike in a $20\,\mu\mathrm{m}$ by $20\,\mu\mathrm{m}$ region. The bottom subplot provides the position of the spike. For clarity, the labels for the shock and transmitted wave are provided for $7.0\,\mathrm{n\,s}$ but are evident at all times after approximately $6.0\,\mathrm{n\,s}$.

sulting synthetic transmission broadly reflect the same behavior displayed in Figure 5.6.

Tilt or misalignment are likely sources of error that can alter the spectra. We consider this for up to 1.5 degrees of tilt as shown in Fig. 5.9, where even 1° of tilt can actually enhance the spike signature slightly, due to the spectral diagnostic integrating through more of the hotter curvature in the interaction feature. Tilt also emulates asymmetry in the flow, which to some degree is expected, as radiography shows interaction features with at least 20 microns of variation in the curvature of an axially symmetrized front.

Another uncertainty in the target is the true concentration of dopants. While requested concentrations are a 1:5 atomic ratio of TiO_2 to SiO_2, in reality the dopant may be mixed at concentrations higher or lower. A lower concentration reduces the number of absorbers in transmissions measurements, leading to higher peaks at all spectral lines (less absorp-

Indicator	Shot	Configuration	Rad. t	Spec. t	Density	Pos	Determination
○	92554	hohlraum	5.9	4.8	57.1	284	
☆	92556	interaction*	5.8	4.8	60.2	273	early
☆	92553	interaction*	5.9	4.8	57.2	255	early
★	92557	interaction*	5.9	4.8	57.3	340	early
★	90740	interaction	7.1	5.5	55.8	449	early
★	90741	interaction	7.1	5.5	61.6	319	*incomplete*
□	96981	ablator	6.7	5.7	56.0	376	
-	96974	interaction	6.7	5.7	55.82	380	early
●	92549	hohlraum	7.4	5.8	56.2	-	
-	92550	interaction	7.4	5.9	54.5	421	likely
■	96990	ablator	8.2	6.7	57.2	256	
○	94788	hohlraum	8.3	7.2	56.7	532	
□	94789	ablator	8.3	7.2	55.8	185	
-	94792	interaction	8.3	7.2	55.1	-	off-frame
★	94786	interaction	8.3	7.2	55.8	-	likely
□	94795	ablator	4.7	8.2	57.5	523	
☆	94793	interaction	4.7	8.2	57.6	489	indeterminate

Table 5.1: Selected experimental shots, their timings, densities, and wave positions, keyed to the position plot above in Figure 5.11. Also included is the likelihood of a spectral detection – after thorough spectral analysis, only two shots are deemed likely to show successful detection: shots 92550 and 94786. However, as we show, four shots show successful imaging of a transmitted subsonic radiation wave feature.

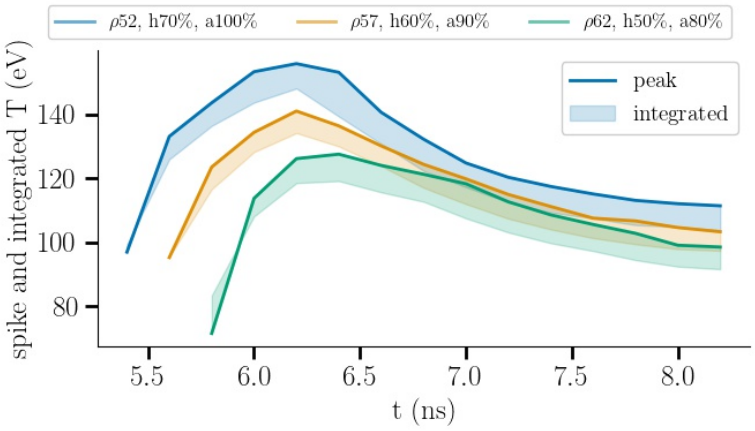

Figure 5.8: Across the simulation suite, the behavior of the spike is consistent: the temperature of the spike (solid) rises, reaches a peak near $6.2\,\mathrm{ns}$, and cools. The range of temperatures that surround the spike in a $20\,\mu\mathrm{m}$ by $20\,\mu\mathrm{m}$ region are shaded.

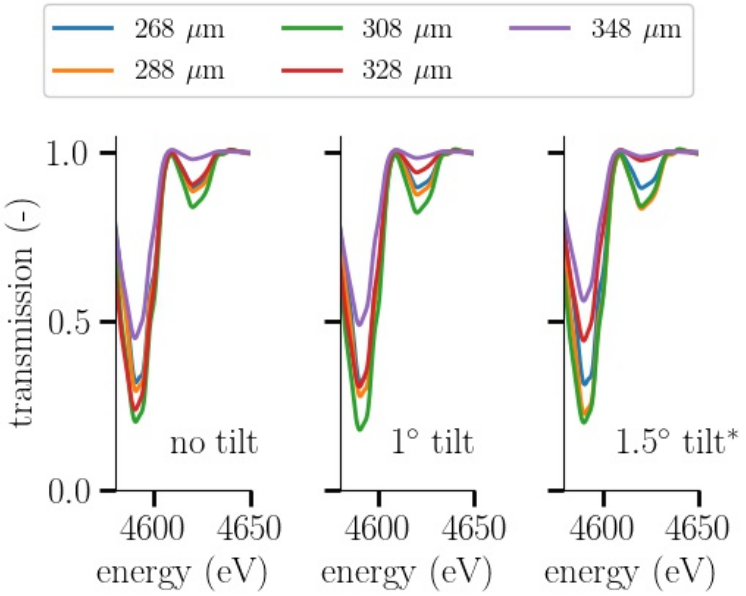

Figure 5.9: Any effective tilt or asymmetry in the spectral integration can change how much of the feature is integrated through. In the high energy features shown for an integration at $7.2\,\mathrm{ns}$, a 1° tilt can actually enhance the nominal spike position reading and preserves expected behavior; due to curvature of the interaction, a tilt can integrate through more of the hotter feature. * Greater tilt can modify the spectra significantly enough to require more analysis (unexpected).

tion). Conversely, a higher concentration may leader to stronger saturation of lines (lines approaching a 0 value/no transmission). Fig. 5.10 illustrates this concept, with some sim-

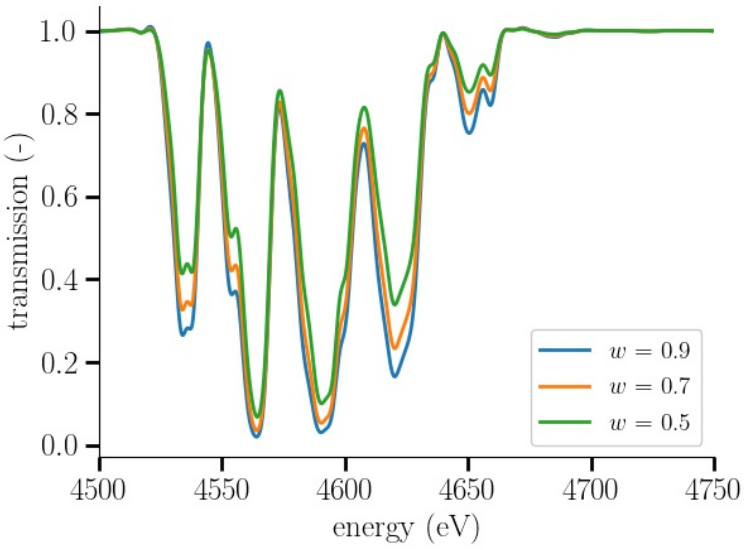

Figure 5.10: Each target batch has an uncertainty in mass fraction. Here we mix more dopant in via the mass fraction $f_{total} = w_{TiO2} + f_{nominal}$. While the range considered ($w = 0.5$ to $w = 1$) changes only the concentration of absorbers, such changes preserve the same evolution of the transmission peaks.

ulated spectra of the lowest density ($52\,\mathrm{mg\,cm^{-3}}$) with the highest hohlraum drive (70%) at several mixes at various mass fractions for reference line $255\,\mu\mathrm{m}$ at $5.4\,\mathrm{ns}$. Targets are likely to have spatial dependence on this concentration, and while currently this target uncertainty is unknown for all targets, we have evidence that this range encompasses these bulk uncertainties.

In all tests emulating potential sources of noise, including varying spatial and temporal integrations, possible tilt or misalignment in the target and/or diagnostic configuration, as well as random spatial noise in the intensity field or on the image plane, the same approximate behavior occurs as described by Figure 5.6 and its accompanying text. For example, in late interaction if the spike is detected, the higher energy features of the lineout position integrating through the interaction will show deeper absorption than neighboring lines even when accounting for predicted noise in synthetic spectra. Thus, if this integration error is systematic, we argue that the diagnostic quality is high enough to encapsulate the described behavior. However, as found in [46], we are unlikely to achieve finer than $8\,\mathrm{eV}$ in uncertainty in the wave temperature. This applies here as well and is our largest deciding factor in successful detection.

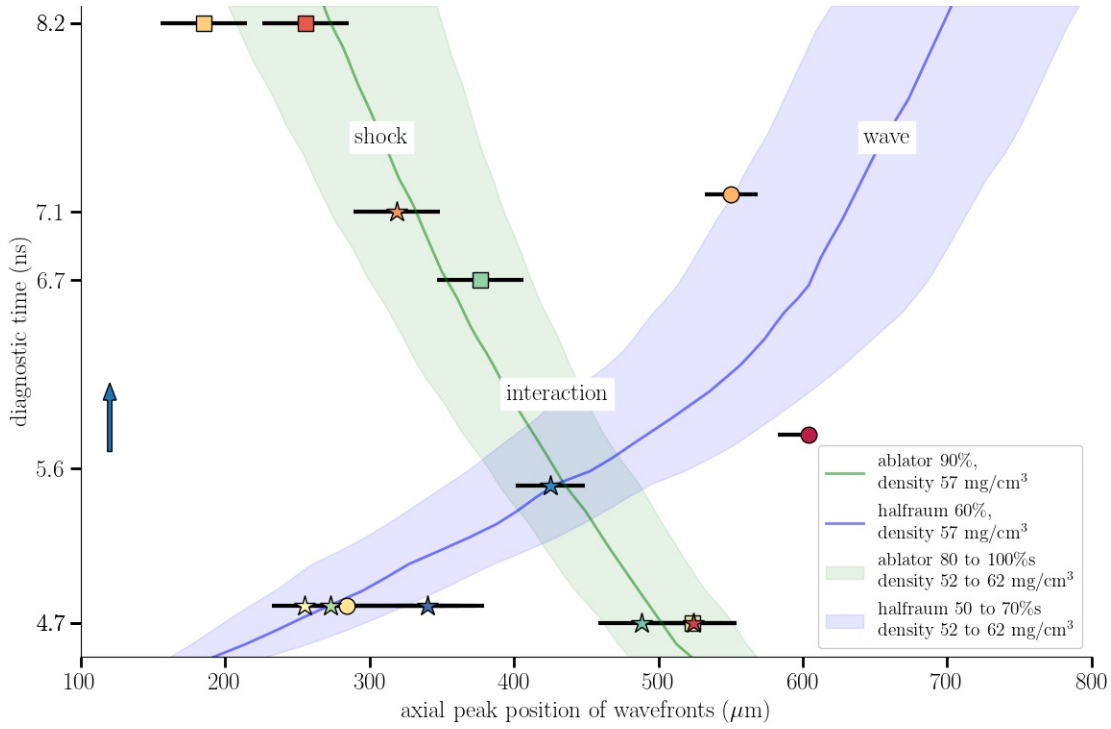

Figure 5.11: Approximate positions of the radiation waves and shock fronts for selected, experimentally determined data points overlayed over simulated positions. Square, circle, and star indicators are for ablator, hohlraum, and interaction shots, as also referenced in Table I.

5.4 Comparison to Experimental Measurements

Figure 5.11 provides guiding estimates for the front positions within the simulation parameter space. Square indicators represent shock positions determined from radiography of ablator-only shots via the direct extraction methods described in Sections II and III. Circlular indicators represent the position of the radiation waves, found by overlaying the spectra of a uniform 60 eV, $60\,\mathrm{mg\,cm^{-3}}$ lineout and identifying the experimental lineout position where we detect less transmission signal below that 60 eV threshold for the Ti-13+ transition stage where possible, or where subsequent lineout positions show only noise. Interaction shots may also be used by the same approximating methods and use star indicators in the figure.

The fastest waves are those having the highest drive power and lowest density (e.g. fastest shock is produceable with 100% ablator drive power into a $52\,\mathrm{mg\,cm^{-3}}$ foam), while the slowest waves follow from the opposite arrangement (80% ablator drive into

$62\,\mathrm{mg\,cm^{-3}}$).

5.4.1 Shock radiography

To calibrate the laser powers requred to drive the ablatively-driven shock we compare the shock positions obtained from experimental radiography to our simulations. An example comparison is shown in Figure 5.12. We use both ablator only and interaction shots to identify the shock front (solid lines) and interaction fronts (dashed lines) as shown in the top subplot. The bottom plot shows the simulated positions, with the inner darker range obtained from simulations with laser powers of $90\% \pm 10\%$ at nominal density. The outer, lighter colored ranges show the laser power extremes with the densities at $57\,\mathrm{mg\,cm^{-3}} \pm 5\,\mathrm{mg\,cm^{-3}}$. These inner and outer ranges enables positional variation of roughly $\pm\,25\,\mu\mathrm{m}$ and $\pm\,50\,\mu\mathrm{m}$, respectively.

The nominal simulation with $57\,\mathrm{mg\,cm^{-3}}$ at 90% ablator-laser power accurately reproduces the experimental shock positions; shots 94795 at $4.6\,\mathrm{n\,s}$ and 96990 at $4.6\,\mathrm{n\,s}$, for example, are within the simulated shock positions $\pm 25\,\mu\mathrm{m}$ and the simulated ranges reflect the variability in the shots around those times. In fact, including shot 94793 at 4.7 ns shows a range of approximately $50\,\mu\mathrm{m}$, encompassing the entire range expected by full simulation suite. This is despite having minimal expected density variation in the target ($57.5\,\mathrm{mg\,cm^{-3}}$ to $58.6\,\mathrm{mg\,cm^{-3}}$) and power variations of less than 6%. Thus our ablator drive expectations are well-captured by the simulation suite. All shots show evidence of spatial variation of the shock front, but after axially symmetrizing the shock fronts we find variation typically within $\pm\,25\,\mu\mathrm{m}$ for the inner $400\,\mu\mathrm{m}$ of material, as similarly found for the COAX experiment [47].

There are potential issues with the simulated shock at later times, in both the shape of the shock for simulations at high powers (e.g. 100%) and the deceleration of the shock for all powers (80% to 100%). Limited data available at late times, specifically shots 96990 at $8.2\,\mathrm{n\,s}$ and particularly 94789 at $8.3\,\mathrm{n\,s}$, suggest that the curvature may increase slightly and be further than expected whereas simulations suggest flatter or even depressed shock fronts near axial center with increasing laser power – we suspect that laser powers much above 90% may be developing erroneous flows at late times. The green curve in the bottom subplot of Figure 5.12 shows this – for a simulation at nominal density but with 100% ablator laser power, there is both deformation of the shock front and slight lag behind expected experimental shots. However, we argue that at the more critical detection times occurring

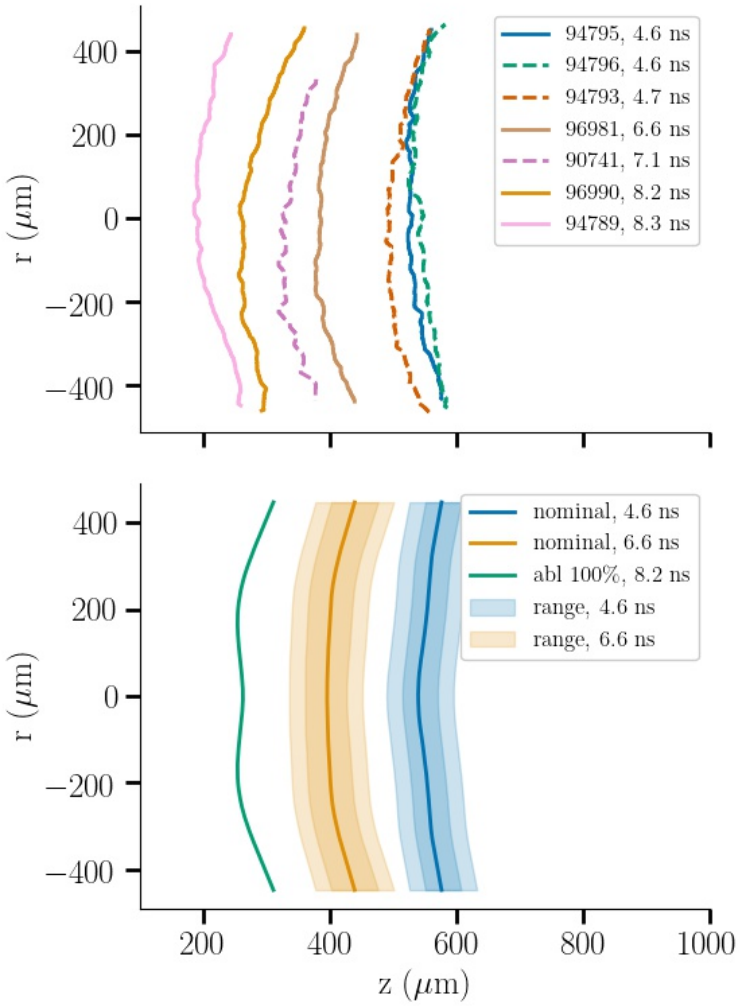

Figure 5.12: Shock fronts from ablator only shots (solid) and interaction feature fronts (dashed) as extracted from experimental radiography (top plot). Simulated ranges of the shock front position shown in the bottom plot very accurately match the positions and shapes of the shock front. For reeference, shot 94795 at 4.6 ms and 96981 at 6.6 ns, match well. The darker shaded regions reflect positions over the range of ablator powers used, 90% $\pm$ 10%, and the lighter ranges approximate the ranges with the density variation of $57\,\mu\mathrm{m} \pm 5\,\mu\mathrm{m}$.

less than $8.2\,\mathrm{n\,s}$, the ablator power ranges used are very satisfactory. In general we deem beyond $8\,\mathrm{n\,s}$ potentially difficult to diagnose for this and for spectral difficulties.

Once the ablator laser drive powers are calibrated, we can use the sparse, radiation wave front data to determine the approximate hohlraum drive powers (as discussed in the beginning of Section 5.4 with Figure 5.11), and we can also the use radiography of the in-

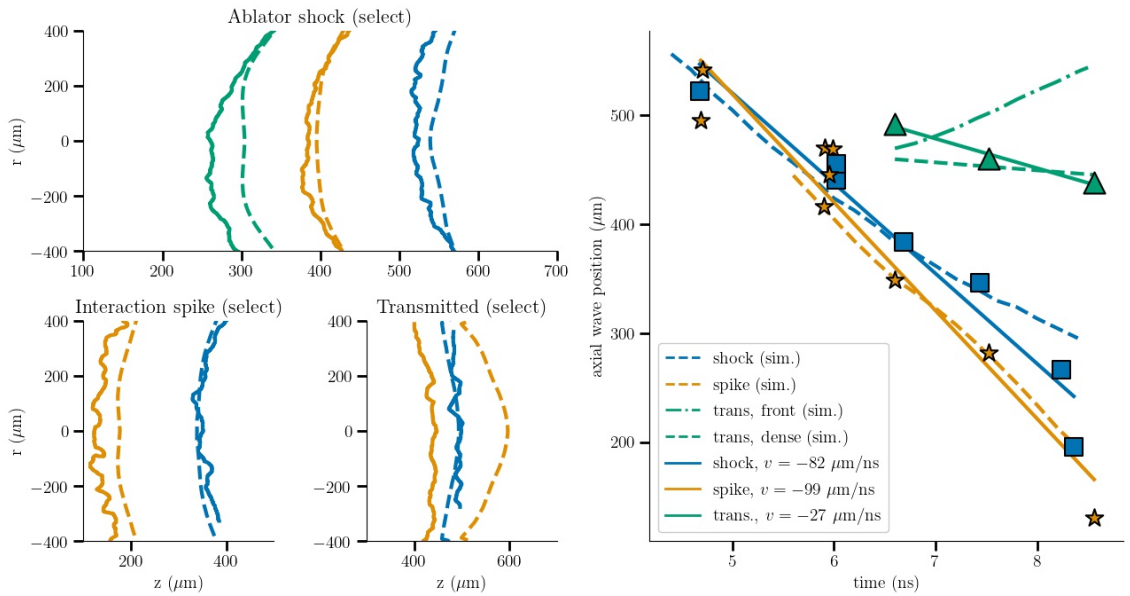

Figure 5.13: Summary of comparisons between synthetic and experimental radiograhy. The three subplots on the left-hand side show selected curves for the ablator shock, the interaction spike, and the interaction transmitted wave fronts. The right plot shows the trends of the axial wave position with ablator data points as squares, interaction spikes as stars, and the transmitted wave as triangles. In all plots solid lines are from experimental analysis, dashed are from synthetic.

teraction shots, in both detection of the front and the transmitted subsonic wave described in Section 5.3.3. Figure 5.13 summarizes the efforts of comparing these remaining radiography features.

In the left half of the plot are select, direct comparisons of simulated shock fronts to the experimental fronts. Each color in these plots is a different shot, where solid lines represent experimental fronts and the dashed lines of the same color represent the simulated fronts (nominal). The right plot shows the trends of the axial position of the wave fronts as a function of time, showing the shock, spike, and transmitted wave evolution in a similar fashion as Figure 5.11.

The simulations show a slight lead at early times and considerable lag at late times in the shock position, but comparing well (within 10%) of the experimentally determined velocity of $82\,\mu\mathrm{m\ ns}^{-1}$. We reiterate that the ablator drive is finished by $4\,\mathrm{ns}$ into the experiment, so that the shock is well formed by the earliest diagnostic timings. Simulated shocks show that the shock front is still very sharp and that gradient detection has at most

an error of $9\,\mu\mathrm{m}$ and is therefore negligible. While there may be radiography difficulties in the experiment at late time, we have insufficient evidence and require more late time data. Furthermore, despite not having a cylindrical sleeve around the target, it is unlikely that radial expansion losses are a significant factor as simulations reproduce the curvature to an acceptable degree. Likeliest is that the furthest data point, shot 94789 may have foam quality issues or is otherwise an outlier. If this shot is removed, the predicted experimental shock velocity becomes approximately $70\,\mu\mathrm{m\,n^{-1}\,s}$, agreeing better with simulated predictions.

Comparisons between the velocity trends in the simulated, interaction spike position versus the experimental spike position also show favorable agreement. Where we do have repeat data, around $5.9\,\mathrm{n\,s}$, we do witness considerable variation around the experimental spike position, observing a mean in axial position of $450\,\mu\mathrm{m} \pm 22\,\mu\mathrm{m}$, but this is well within either our density parameter variation. Including laser powers, we require less than a 10% adjustment in laser power to explain this discrepancy (estimated at 4-5%). Pre-interaction, i.e. points at $4.8\,\mathrm{ns}$ share the trend with the ablator-only shots.

Finally, comparisons of the transmitted subsonic radiation flow reveal our largest discrepancy. In analysis of experimental radiography, the inferred position of the transmitted flow shows net velocity towards the hohlraum, whereas simulations predict velocity flows towards the ablator. Earlier radiography at 6.6 for shot 96974 and 7.7 for shot 92550 suggest reasonable agreement if we accept an error range of approximately $32\,\mu\mathrm{m}$, however, again the late time points (e.g. shot 90739 at 8.5 ns) provide indication that our comparisons are tenuous at late times. Figure 5.14 shows the excellent agreement between simulations at 6.6 ns and shot 96974.

A likely explanation for the discrepancy in transmitted wave comparisons is that the contour of the transmitted wave front is too faint or saturated out at late times. The dense region just preceding the transmitted wave front is typically visible where the wave front may not be, but it may be unclear which edge of this region (more towards or away from the ablator) we may be able to capture in analysis. This is arguably the case for 92550 as shown in Figure 5.15. While the interaction fronts compare well, the experimentally determined, partial contour is unlikely to represent the transmitted wave front and may actually represent the innermost edge of the dense region (shown as the darker region near the transmitted wave front in the Figure). Two other shots (90741 at 8.5 ns, included; 96991 at 8.2 ns, excluded due to potential mis-timing) confirm similar behavior of the transmitted

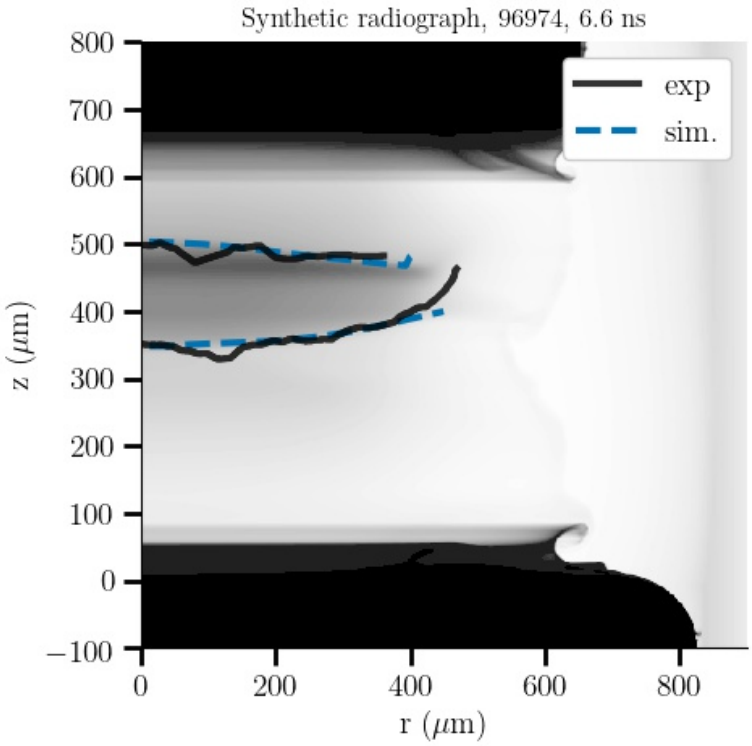

Figure 5.14: Synthetic radiography showing excellent agreement with experimentally determined radiography for shot 96974.

wave shock, verifying a density structure consistent with the simulated structure as shown in Figure 5.7.

With shots 96974 and 92550, arguing that the contour represents the dense feature and not the transmitted wave front in the latter, we observe at least two time points that show reasonable agreement where we have successfully imaged the interaction. In future analysis and experiments we will need to improve the radiography and make imaging the transmitted wave a high-priority.

5.4.2 Spectra

In this section, we do perform some basic temperature inference, but more importantly, attempt detection with the spectral diagnostic.By comparing synthetic transmission data from our simulations to the experimental spectra, we can infer the temperature profile in the same manner discussed in our COAX analysis [47]. We begin with a discussion of comparison methodology, then show some select comparisons between experiment and simulation.

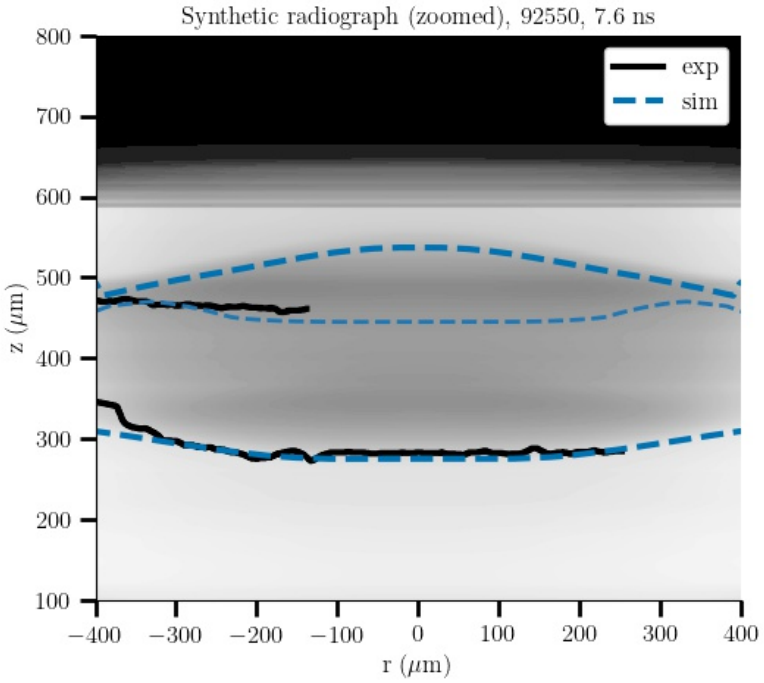

Figure 5.15: Analysis of late-time radiography shows the difficulty of comparing contours. Shown for shot 92550 are the interaction fronts comparing well ($\sim 300\,\mu$m) but potentially conflicting contours for the transmitted wave ($\sim 500\,\mu$m). The partial contour obtainable from experimental radiographs may actually represent the contour of the dense feature just prior to the transmitted wave. At late time the transmitted wave front may be too saturated to image.

When estimating best fits for spectra, the parameter space is extremely large. Each of the lineout positions can have shape, scaling, and offset parameters in addition to opacity mixing, tilt, spatial shifting, and temporal shifting parameters. Each profile parameter can be affected, namely T and ρ , e.g. $T(ar) = bT(ar) + T_0$, where a is a radial scaling parameter, b scales the value of T, and T_0 is an offset. Due to the presence of the interaction feature, we have also looked at scaling the temperature and width of the spike, although this is more difficult to do through entire integrated windows, so where discussed in Subsection 5.5.2 we assume that the spike is the local peak and has maxmimal width of $200\,\mu$m. We reiterate that the spike is likely hotter and much narrower, as indicated in the discussion of Section 5.3.2. We can neglect any significant deviation in angular or spatial distribution of the backlighter. In the comparisons shown in this section, we focus on profile scaling, continuum fitting, and opacity mixing parameters. The reference synthetic transmission shown are produced for the closest labeled simulation with unmodified settings (assume no

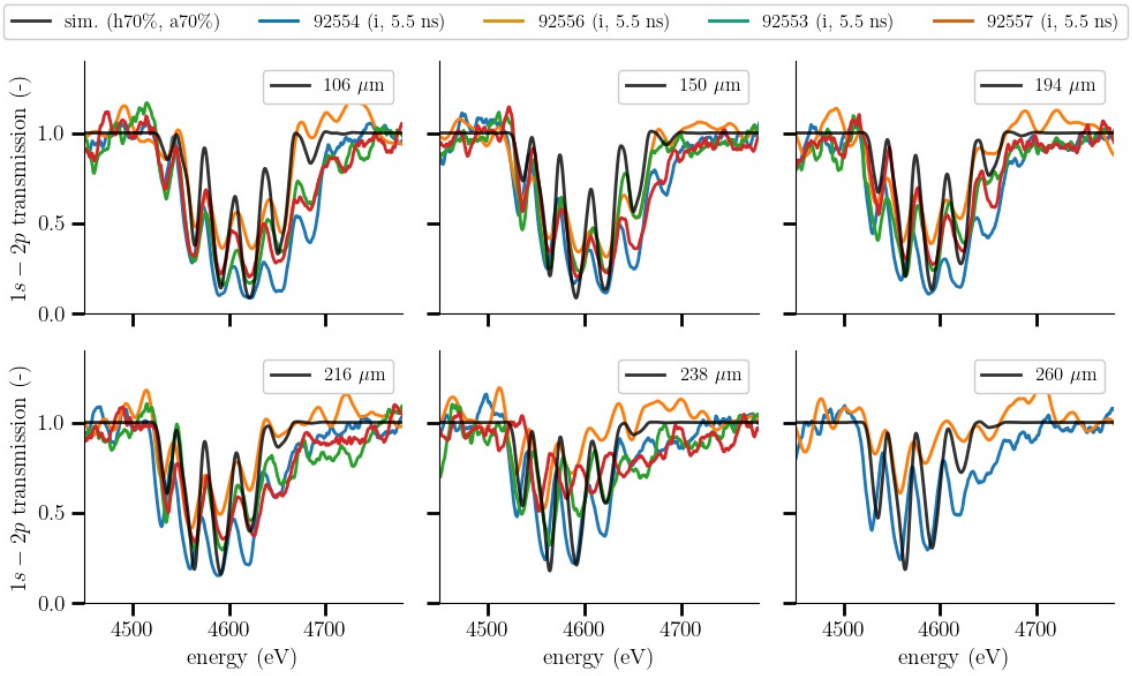

Figure 5.16: $1s - 2p$ transmission spectra at 4800 ps for selected shots.

scaling, default continuum fit, and the opacity is mixed at a 1:5 ratio).

Figure 5.16 shows a sample of lineout positions closest to the wave front (approximately $300\,\mu\mathrm{m}$) for shots 92554, 92556, 92553, and 92557. Also plotted is the synthetic spectra for the simulation having the fastest, hottest radiation wave, with $\rho = 52\,\mathrm{mg\,cm^{-3}}$, a hohlraum laser power of 70%, and an ablator laser power of 100%, and advanced in time at $5.2\,\mathrm{ns}$. Because interaction has assertively not occured, this required advance in time likely reflects the same finding in COAX [47], where simulations systematically predicted a slightly slower wave, with lower temperature near the wave front.

In early time evolution of the radiation wave, our simulations under-predict the front position, in addition to more rapidly decaying in temperature towards the front. This is also evidenced by the nominal simulations having lower temperatures towards the hohlraum (approximately $5\,\mathrm{eV}$ to $10\,\mathrm{eV}$), indicating that the hohlraum model produces slightly less powerful fluxes needed to drive the wave. This was also systematically observed in the temperature inference of the radiation wave in COAX experiment, but found that after $2\,\mathrm{ns}$ into the drive that the simulated temperatures achieved better comparisons to the experimental data [47]. Here it is still only $0.8\,\mathrm{ns}$ after the drive has begun.

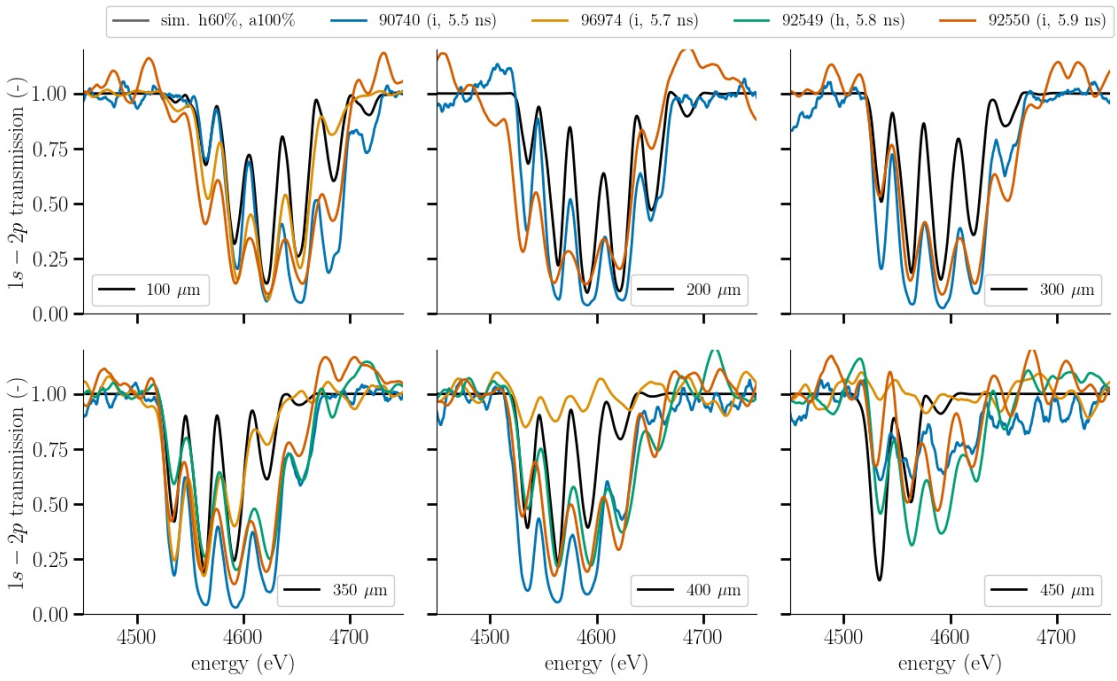

Figure 5.17: $1s - 2p$ transmission spectra at 5500 ps for selected shots.

While three of the shots are interaction shots, a time of $4.8\,\mathrm{ns}$ is too early for interaction as the waves have to travel another $150\,\mu\mathrm{m}$ approximately before meeting. We can therefore use these shots in conjunction with the hohlraum-only shot, 92554. The experimental spectra do show a wide range in transmission values and variation even comparing line positions, however, the trend clearly indicates the expected behavior of the radiation wave.

Figure 5.17 compares transmission for available interaction shots at $5.5\,\mathrm{ns}$, 90740 and 90741, in addition to shots at $5.7\,\mathrm{ns}$ to $5.9\,\mathrm{ns}$, 96974, 92549, and 92550. While $400\,\mathrm{ps}$ may seem like too large of a range, here it shows clearly evolving evolution of the wave front until the point of interaction. The hohlraum shot 92548 ends in the expected vicinity of first interaction, roughly after $401\,\mu\mathrm{m}$ as in the figure. This interaction region is apparent in Figure 5.11 as well.

The transmissions at $5.5\,\mathrm{ns}$ to $5.9\,\mathrm{ns}$ provide the earliest opportunity to attempt detection of the interaction feature and indeed shot 92550 at $5.9\,\mathrm{ns}$ may indicate a successful detection. This shot has both usable and quality $1s-2p$ and $1s-3p$ transmission data, both of which indicate a strong trend in rising temperature in the lineout positions at $398\,\mu\mathrm{m}$ to $421\,\mu\mathrm{m}$, very nearly where predicted by simulation. This is shown in Figure 5.18.

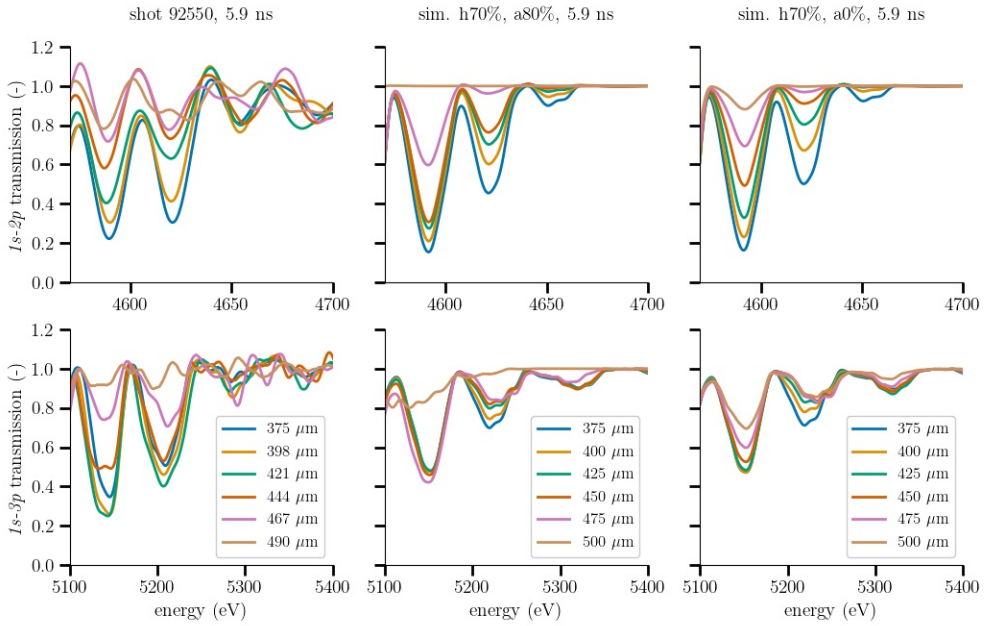

Figure 5.18: Zoomed-in comparison of the higher energy features in the transmissions of shot 92550, a simulation with hohlraum drive at 70% and an ablator drive at 80%, and a hohlraum-only drive at 70%. The synthetic interaction spectra shows more prominent lines at 4591 eV and 4621 eV at the lineout position of 450 um (red line).

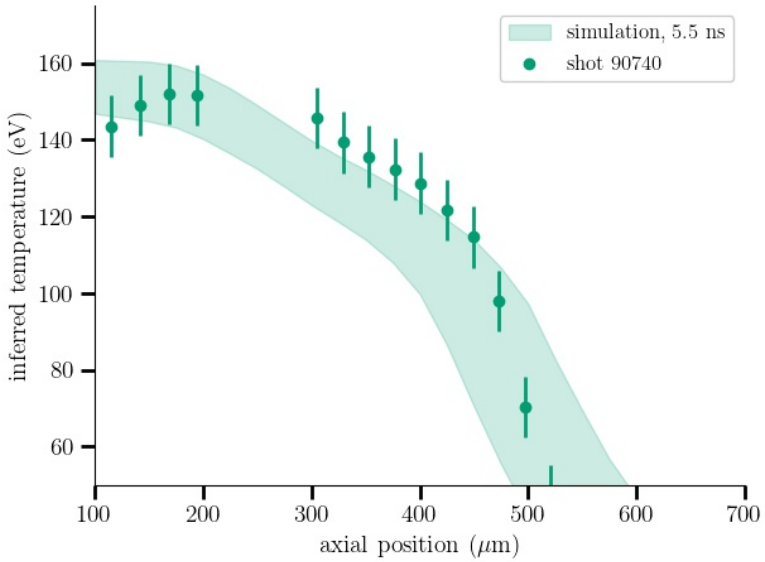

Figure 5.19: Inferred temperature profile for shots 90740 and the full simulated temperature range at 5.5 ps.

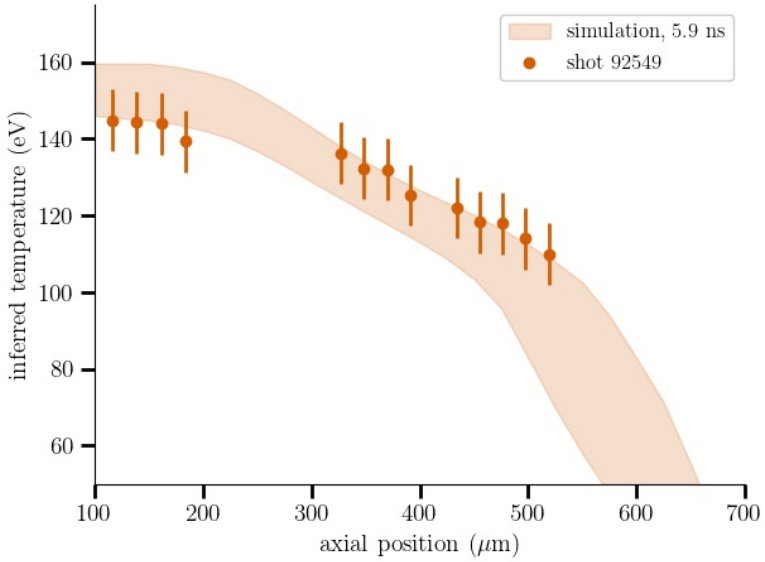

Figure 5.20: Inferred temperature profile for shots 92549 and the full simulated temperature range at 5.9 ps.

The experimental, 1s2p transmission of lineouts above 444 um is the result of a inferring a continuum fit on the noisy spectral data. This issue has been discussed in cite COAX. However, even when applying different continuum fits (by changing fitting parameters in the asymmetric least squares method) the presence of transmission at lines 4591 eV and 4621 eV is consistent across the fits suggesting that these lines do show absorption (despite an indiscernible transmission value). Fortunately, the 1s3p data shows higher quality fits, allowing a clearer interpretation of the transmission at these lineouts.

In these simulations, the shock is located at approximately 447 um, which means that during the integration window (5.9 ns +/- 0.1 ns), lineouts in the region from 427 um to 467 will have integrated through the spike. Comparing between the synthetic interaction and hohlraum transmissions, three pieces of evidence may indicate a successful detection of the interaction. First, the synthetic interaction spectra shows more prominent lines at 4591 eV and 4621 eV at the lineout position of 450 um (red line). These lines are much stronger than hohlraum only positions.

Second, despite a difficult continuum fit in the 1s-3p synthetic spectra for the line at $500\,\mu\mathrm{m}$, comparing to the experimental position at $490\,\mu\mathrm{m}$, it seems clear that the higher energy lines become less apparent, as the spectral diagnostic must integrate through the dense shock. The hohlraum-only transmission further suggest this is the case.

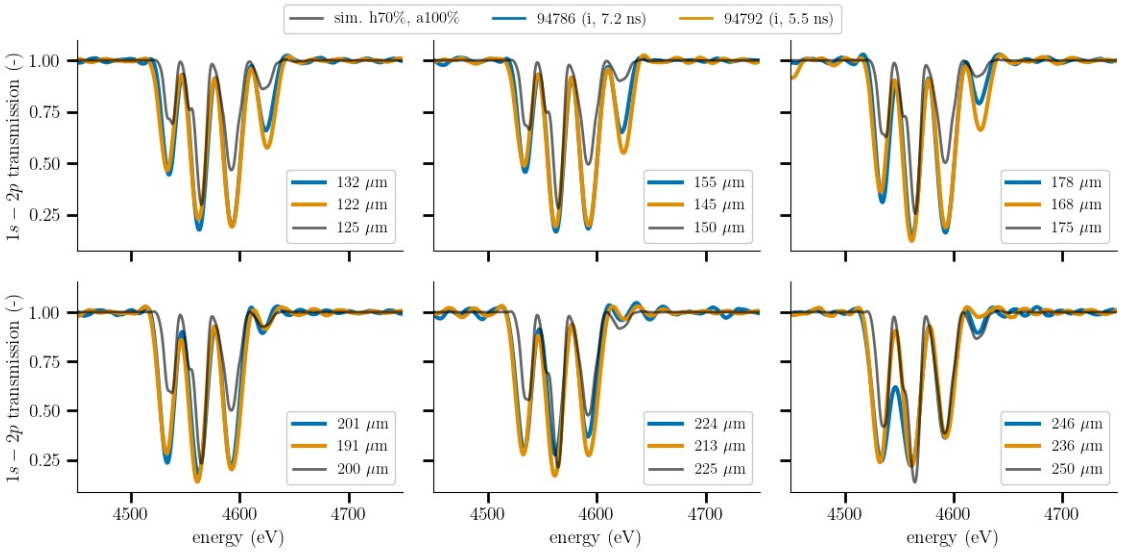

Figure 5.21: Simulations with the highest laser drives compare best to the transmission at $7.2\,\mathrm{ns}$ for the two interaction shots 94786 and 94792. In this simulation, the spike is at approximately $246\,\mu\mathrm{g}$, shown in the bottom left frame, however, there is a gap in the spetra (no lineouts between $246\,\mu\mathrm{g}$ to $343\,\mu\mathrm{g}$ Both of these shots suggest remarkably similar evolution.

We have oversmoothed and readjusted the synthetic 1s-3p data, to compare more clearly to the experimental data in this case. The lineout positions preceding the interaction feature strongly demonstrate the expected behavior with a high degree of accuracy.

In Figure 5.20, we infer pre-interaction temperatures of the radiation wave, using the methods assessed in our previous work [46, 47]. In summary, for each lineout position in any experimental data, we select the desired features for scoring a best-of-fit by minimizing the L^2 norm. As in prior work, we use the three highest energy features for a combined minimization– by using these features, we attempt to evaluate the peak temperatures that give rise to the highest energy absorption features. For each of these lineouts, the nearest spatiotemporal lineouts from synthetic spectra are evaluated, including all lineouts with the large range of scaling parameters. The best fits determine the inferred temperature.

Due to noise, baseline thresholds, and potential continuum removal errors in the experimental spectra, peaks and troughs may be shortened or deepened. Performing best-of-fit tests may require hundreds of iterations over these large and in most cases fairly unknown ranges of parameters. For temperature inference, as shown in our previous analysis [47],

we may reliably infer bounds by firstly assuming our simulation range producing correct front positions reasonably models the experiment and secondly, that density variation does not play a dominant role in the transmission. Thus the minimum temperature inferred is ultimately the least-energetic simulation, producing the coldest temperature profiles and likewise, the highest temperature inferred is the most-energetic.

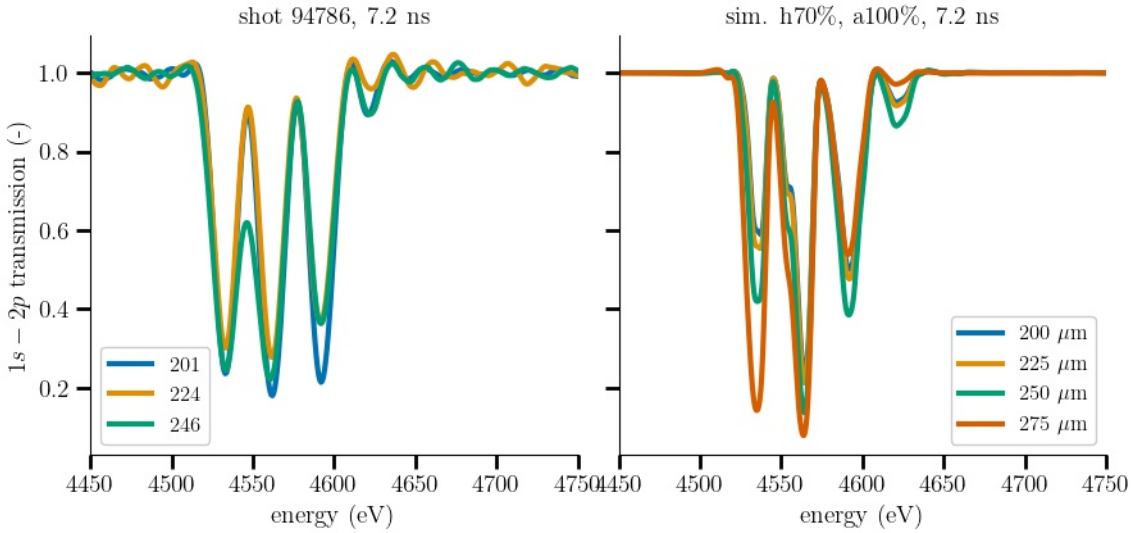

Figure 5.22: While there are no transmission lineouts available for 246 µg to 343 µg due to a gap in the MCP strips, stacking the lineouts for the spike whose predicted location is at 250 µg show evidence of an increased temperature in the experiment as we look from 224 µg to 246 µg. An extra line in the simulated transmission is included, 275 μm to illustrate the expected continuation in the experimental spectra. The colors in each subplot represent the same approximate position.

The remaining likely detection occurs at 7.2 ns. Two interaction shots, 94788 and 94792 provide transmission data that suggest very similar evolution. Figure 5.21 shows a comparison between these two shots and a simulation having the highest analyzed laser drives, with 70% for the hohlraum and 100% for the ablator. At all lineout positions it is clear that transmission peaks in the synthetic spectra underpredict the experimental peaks, but also that nearest the hohlraum the experiment may again show consistently hotter temperature profiles. However, both simulation and experiment show slowly varying temperature profiles, which is nearly flat for the simulation up to the interaction spike.

Here the simulation predicts the spike position at 246 μm. Unfortunately, due to a gap in the MCP strips, no spectra is available from 246 µg to 343 µg, beyond which the sig-

nal rapidly decays due to integration through the denser features. Nonetheless, if we look closely at the transmission of shot 97486 near the end of this gap, we can see behavior that suggests integration through an elevated temperature. This is shown at the lineout position of $246\,\mu\mathrm{m}$ in the left plot of Figure 5.22. The right plot shows the stacked lineouts at similar positions for the simulation having a hohlraum drive of 70% for the hohlraum and an ablator drive of 100%. Because the $1s - 2p$ transmission data here is of very high quality, despite the unavailability of subsequent lines we argue . A caveat is that the $1s - 3p$ data here is of poor quality and unusable to bolster this argument.

Currently, no times in between the early shots at $5.9\,\mathrm{ns}$ and $7.2\,\mathrm{ns}$ are available. Shot attempts between these times have been attempted, however, co-timing issues make the data unreliable.

5.5 Discussion

5.5.1 Value of current measurements

The presented measurements and comparisons suggest early success in detection, however, they highlight the difficulty of detection of a theoretically demonstrated phenomenon, and detail needs for improvement to the platform to improve confidence in our modeling methodology. The three types of shots, hohlraum-only, ablator-only, and interaction shots each provide unique signatures for diagnosing the flow, but do experimentally confirm a wide variability in initial conditions. The two interaction shots that show some evidence of spectral detection of the interaction are useful starting points for this research.

The temperature inference of hohlraum-only shots suggest large variation in the temperature conditions of the radiation wave, in addition to some wave front positions (e.g. shot 92554). As in the COAX experiment, we are systematically likely to slightly under-predict the temperature profile of the radiation flow. Additionally, comparison with interaction shots is useful to infer pre- or early-interaction conditions, indicating the need for more co-timed spectra in these shots.

More readily constrained are the shock positions from ablator-only runs. Radiography analysis has highlighted two key difficulties: late-time measurement and corroboration of the shock front positions as well as detection of the dense, transmitted wave feature.

5.5.2 Future improvements to the platform

Certainly increasing the spatial or temporal resolution will improve detection. If more finely, spatio-temporally resolved lineouts are achievable, an additional improvement in the detection with more amplified differences between higher energy peaks may be found by improving the planarity of the shock-wave interaction. Consider the brief example of Figure 5.23 in which we have produced synthetic spectra for the nominal simulation at $6.6\,\mathrm{ps}$ in the top plot and for the same lineouts with artificially broadened features by scaling the radial profile of the lineouts by 5 (e.g. $T = T(5r)$). In this example, with improvements to the planarity we can potentially detect even earlier interaction evolution.

If we can achieve even 10 micron resolution in both imaging and post-processing, we may be able to improve finer detection. The result may be drastic, particularly for late-time evolution of the interaction feature. This is similarly observed for more finer temporal measurements as well (in this case $100\,\mathrm{ps}$). We note that without the increase in spatial or temporal resolution, improvements in detection resulting from a more planar interaction are marginal, yielding at best a 5% relative increase in the ratio of the interaction peaks compared to neighboring lineout peaks. However, as shown in the example Figure 5.23, with the spectral improvements, the relative increase may be as much as 10-20%.

Another large improvement to the platform is to increase the temperature of the interaction. In the previous plot, we show a dramatic increase in spectral detection of the spike by increasing the temperature of the spike by 10%. We will investigate using more refined theoretical models to best increase the planarity and temperature.

Without changing the current experimental configuration, additional modifications that may improve detection include using different or multiple dopants such as Scandium or Vanadium oxides. Such inclusions may enable sensitive absorption peaks of atomic transitions in multiple discrete energy ranges, enhancing the certainty of a detection. Consider the synthetic spectra of the nominal simulation at $7.2\,\mathrm{ns}$ in Figure 5.24. In order from top to bottom we show the integrated spectra through Titanium Oxide (TiSi5O12), Vanadium Oxide (V2O5), and Scandium Oxide (Sc2Si4O11) doped foams.

We are currently extending our capabilities with using multiple materials (as in XFOL,

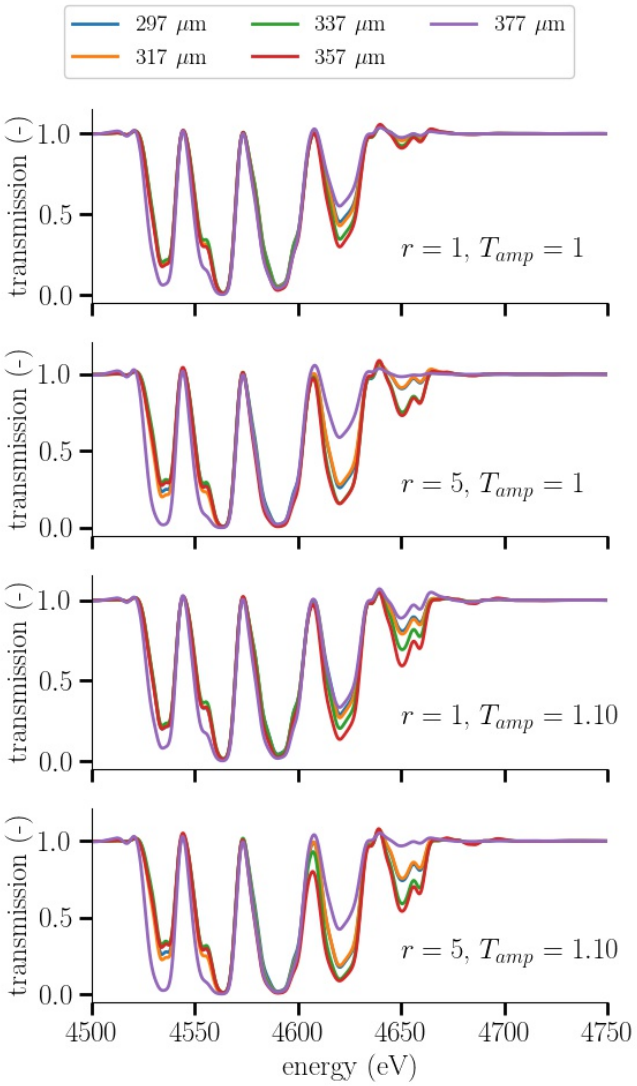

Figure 5.23: Increasing the planarity with finer spatial resolution in the spectral measurement can drastically improve both earlier and later detection. Here in the example of synthetic spectra for the nominal simulation at $6.6\,\mathrm{ns}$ with artificially scaled profiles having $5r$, all peaks show widened relative amplitudes with now prominent higher energy features.

future COAX, etc), which will greatly increase our constraining power using previously analyzed temperature reconstruction techniques. We will assess this possibility in detail in a future design iteration.

Finally, in each iteration of our work, we improve our modeling of the radiography and spectra processes – we will continue to push our modeling capabilities to fully physically-informed reproduction of the diagnostic process. In radiography, we are attempting to

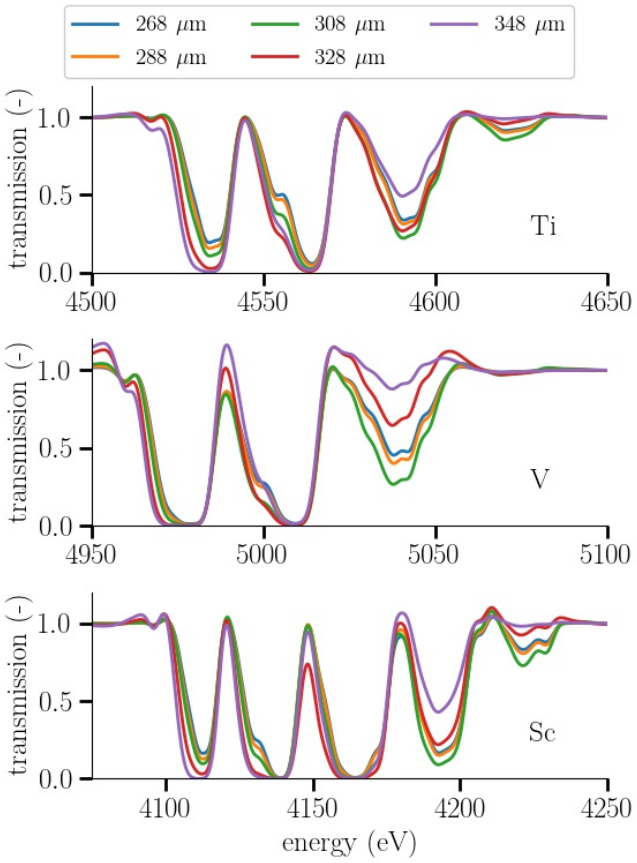

Figure 5.24: Using multiple dopants will provide three measurements of $1s - 2p$ transition spectra and three $1s - 3p$ spectra for a single shot. Here we compare the same simulation for three different dopants with Ti, V, and Sc all at the same concentration, for the nominal simulation at 7.2 ns.

constrain full spatial inference of the density field. In spectra, due to the simulation variability, large parameter ranges present in the comparison methods, and the uncertainties in the experimental spectra, there is likely a high degree of degeneracy in the acceptable fits of the synthetic spectra. Our next iteration of the spectral platform and analysis pipeline will improve our fits, reduce degeneracies, and seek state solutions via physics-informed machine learning. In an ongoing effort, we will assess the roles of asymmetry and target uncertainty as we push our code efforts into fully 3D simulations modeling stochastic foams and drives.

5.6 Conclusion

Detecting a shock interacting with a radiation wave in a high-energy density experiment will prove a powerful capability in high precision science. We have provided the analysis of multiple shots that help constrain drive powers and foam densities via shock radiography and spectra of the radiation waves. Furthermore we provide four shots that show early evidence of successful detection of the interaction feature.

CHAPTER 6

Conclusion

6.1 Summary

In this thesis, I have presented three original works of research on the design, simulation, and analysis of HEDP experiments. While each experiment was different, they are united by the required techniques and toolkits of a computational researcher studying at the intersection of HEDP, astrophysics, radiation flow, and laser laboratory experiment. For concluding remarks, I will briefly summarize each experiment and the achieved goals of the presented research, finally providing broader impact of this body of work.

The first experiment was a platform for investigating the role of KHI on galactic filaments in galaxy formation. Not only did the design and analysis demonstrate that our platform probes the best-case scenario for KHI growth in the astrophysical setting, but our early experimental runs compared well to the theory developed. This work established a clear Ryutov scaling, linking the experiment to the astrophysical case, and outlined suggestions to the theoretical limit of the role of KH growth.

The second experiment is the COAX experiment, a radiation tube experiment using a hohlraum to drive a supersonic-to-subsonic transitioning radiation wave. In my research I showed that the novel spectroscopy platform could be used to infer the temperature profile of the wave, using detailed synthetic spectroscopy. The research also constrained the parameters of the radiation hydrodynamics simulations of the experiment, by simultaneous comparison of the spectroscopy, radiography, and Dante hohlraum flux measurements, across the suite of successful, analyzed experiments.

The third experiment is the Radishock experiment, which aims to detect the unique signatures of a radiation wave interacting with a counter-propagating shock. My work on

this platform partially extends the work of the COAX research, as it is built from that platform. Similarly, I analyze a large set of shots, detailing shock only, radiation wave only, and interaction shots, focusing on spectroscopic and radiographic characterization of each shot. I systematically assembled the trends of the wave fronts, inferred temperature profiles, identified key difficulties and needed improvements in future shots, and outlined the few successful indications of detection of the interaction.

Foremost, the impact of this work is the useful contribution to the growing, relatively new field of high-energy density physics experiments. From the KHI experiment, astrophysics aside, this platform provides a unique setting for studying the various modes of KHI (surface and body modes) on cylindrical surfaces. Developing the radiation flow platforms of COAX and Radishock as well as their analysis techniques benefits UQ efforts as a whole, as significant research is needed to understand how best to compare simulation and experiment.

6.2 Future work

The KHI platform marks a necessary beginning to studies of cylindrical KHI growth. The platform can be modified to investigate the KHI growth with a number of initial perturbations and shock velocities to assess a wider range of applicability to the incompressible KHI theory and the different modes of growth. The platform can also be made radiative, by moving to both lower density configurations and using stronger drive power for the shear-flow generating shock.

The COAX and Radishock experiment represent initial successful designs of a new generation of radiation flow experiments, serving as the base for a number of platforms at LANL in active research. The COAX experiment, owing to its underrepresented space in radiation wave experiments as a supersonic-to-subsonic wave experiment, can necessarily be improved and repeated. With recent modern analytical theory, this experiment can become a new validation and verification test. Similarly the Radishock experiment must be repeated with some suggested refinements presented in that work, such as the use of a multi-dopant embedded foam. Detection of the shock and wave interaction pushes our current diagnostic capabilities to their limit.

However, based on the validation and UQ efforts of both the COAX and Radishock experiment, a significant new endeavor of research is needed. Often the result of these efforts

is the parameter range allowing acceptable solutions. But remains is the epistemological question of what is actually being learned, how to make improvements in the code and modeling physics, and what the quality of comparison between experiment and simulation is. New error metrics for successful comparison must be defined, data maximization needs to become a priority, synthetic diagnostics must accurately account for all sources of error and noise, and a new propagation framework is needed for testing and isolating pieces of the multi-physics puzzle to make improvements in the validation and UQ process of modeling experiments. Among the number of new techniques and methods are the integration of deep-learning based solvers and physics-informed machine learning into UQ process. Such ideas will become a key focus of my anticipated post-doctoral thesis.

BIBLIOGRAPHY

[1] Drake, R. P., "Introduction to high-energy-density physics," *High-Energy-Density Physics*, Springer, 2018, pp. 1–20.

[2] Philippi, P. C., Mattila, K. K., Hegele Júnior, L. A., and Siebert, D. N., "Kinetic projection and stability in lattice-boltzmann schemes," 2015.

[3] Malka, E. and Heizler, S. I., "Supersonic–subsonic transition region in radiative heat flow via self-similar solutions," *Physics of Fluids*, Vol. 34, No. 6, 2022, pp. 066105.

[4] Sutherland, R., Dopita, M., Binette, L., and Groves, B., "MAPPINGS V: Astrophysical Plasma Modeling Code," *Astrophys. Source Code Libr.*, July 2018, pp. ascl:1807.005.

[5] Johns, H. M., Fryer, C. L., Wood, S., Fontes, C. J., Kozlowski, P. M., Lanier, N. E., Liao, A., Perry, T. S., Morton, J. W., Brown, C. R., et al., "A temperature profile diagnostic for radiation waves on OMEGA-60," *High Energy Density Physics*, Vol. 39, 2021, pp. 100939.

[6] Saumon, D. and Guillot, T., "Shock compression of deuterium and the interiors of Jupiter and Saturn," *The Astrophysical Journal*, Vol. 609, No. 2, 2004, pp. 1170.

[7] Saumon, D., Chabrier, G., and van Horn, H. M., "An equation of state for low-mass stars and giant planets," *The astrophysical journal supplement series*, Vol. 99, 1995, pp. 713.

[8] Tolstov, A., Blinnikov, S., and Nadyozhin, D., "Coupling of matter and radiation at supernova shock breakout," *Monthly Notices of the Royal Astronomical Society*, Vol. 429, No. 4, 2013, pp. 3181–3199.

[9] Kifonidis, K., Plewa, T., Janka, H.-T., and Müller, E., "Non-spherical core collapse supernovae-I. Neutrino-driven convection, Rayleigh-Taylor instabilities, and the formation and propagation of metal clumps," *Astronomy & Astrophysics*, Vol. 408, No. 2, 2003, pp. 621–649.

[10] Hartigan, P., "Shock waves in outflows from young stars," *Jets in Young Stellar Objects*, 2003, pp. 111–122.

[11] Bellan, P., Livio, M., Kato, Y., Lebedev, S., Ray, T., Ferrari, A., Hartigan, P., Frank, A., Foster, J., and Nicolai, P., "Astrophysical jets: Observations, numerical simulations, and laboratory experiments," *Physics of Plasmas*, Vol. 16, No. 4, 2009, pp. 041005.

[12] Balbus, S. A. and Hawley, J. F., "A powerful local shear instability in weakly magnetized disks. I-Linear analysis. II-Nonlinear evolution," *The Astrophysical Journal*, Vol. 376, 1991, pp. 214–233.

[13] Remington, B. A., "High energy density laboratory astrophysics," *Plasma Physics and Controlled Fusion*, Vol. 47, No. 5A, 2005, pp. A191.

[14] Gatu Johnson, M., Zylstra, A., Bacher, A., Brune, C., Casey, D., Forrest, C., Herrmann, H., Hohenberger, M., Sayre, D., Bionta, R., et al., "Development of an inertial confinement fusion platform to study charged-particle-producing nuclear reactions relevant to nuclear astrophysics," *Physics of Plasmas*, Vol. 24, No. 4, 2017, pp. 041407.

[15] Remington, B. and MacKinnon, A., "White paper on NIF Discovery Science and frontier regimes of HEDP," Tech. rep., Lawrence Livermore National Lab.(LLNL), Livermore, CA (United States), 2021.

[16] Lindl, J., "Development of the indirect-drive approach to inertial confinement fusion and the target physics basis for ignition and gain," *Physics of plasmas*, Vol. 2, No. 11, 1995, pp. 3933–4024.

[17] Abu-Shawareb, H., Acree, R., Adams, P., Adams, J., Addis, B., Aden, R., Adrian, P., Afeyan, B., Aggleton, M., Aghaian, L., et al., "Lawson criterion for ignition exceeded in an inertial fusion experiment," *Physical Review Letters*, Vol. 129, No. 7, 2022, pp. 075001.

[18] Ryutov, D., Drake, R. P., Kane, J., Liang, E., Remington, B. A., and Wood-Vasey, W. M., "Similarity Criteria for the Laboratory Simulation of Supernova Hydrodynamics," *The Astrophysical Journal*, Vol. 518, No. 2, jun 1999, pp. 821–832.

[19] Kuranz, C. C., Park, H.-S., Huntington, C. M., Miles, A. R., Remington, B. A., Plewa, T., Trantham, M. R., Robey, H. F., Shvarts, D., Shimony, A., Raman, K., MacLaren, S., Wan, W. C., Doss, F. W., Kline, J., Flippo, K. A., Malamud, G., Handy, T. A., Prisbrey, S., Krauland, C. M., Klein, S. R., Harding, E. C., Wallace, R., Grosskopf, M. J., Marion, D. C., Kalantar, D., Giraldez, E., and Drake, R. P., "How high energy fluxes may affect Rayleigh–Taylor instability growth in young supernova remnants," *Nature Communications*, Vol. 9, No. 1, 2018, pp. 1564.

[20] Coffing, S. X., Angulo, A. A., Trantham, M. R., Birnboim, Y., Kuranz, C. C., Drake, R. P., and Malamud, G., "Design and scaling of an Omega-EP experiment to study cold streams feeding early galaxies," *The Astrophysical Journal Supplement Series*, Vol. 245, No. 2, 2019, pp. 27.

[21] Falize, E., Michaut, C., and Bouquet, S., "Similarity properties and scaling laws of radiation hydrodynamic flows in laboratory astrophysics," *The Astrophysical Journal*, Vol. 730, No. 2, 2011, pp. 96.

[22] Ripin, B. H., Manka, C., Peyser, T., McLean, E., Stamper, J., Mostovych, A., Grun, J., Kearney, K., Crawford, J., and Huba, J., "Laboratory laser-produced astrophysical-like plasmas," *Laser and Particle Beams*, Vol. 8, No. 1-2, 1990, pp. 183–190.

[23] Takabe, H., "Inertial confinement fusion and supernova explosion," *Purazuma, Kaku Yugo Gakkai-Shi*, Vol. 69, No. 11, 1993, pp. 1285–1300.

[24] Remington, B. A., Arnett, D., Paul, R., Drake, and Takabe, H., "Modeling astrophysical phenomena in the laboratory with intense lasers," *Science*, Vol. 284, No. 5419, 1999, pp. 1488–1493.

[25] Springer, P., Fields, D., Wilson, B., Nash, J., Goldstein, W., Iglesias, C., Rogers, F., Swenson, J., Chen, M., Bar-Shalom, A., et al., "Spectroscopic absorption measurements of an iron plasma," *Physical review letters*, Vol. 69, No. 26, 1992, pp. 3735.

[26] Hartigan, P., Foster, J., Wilde, B., Coker, R., Rosen, P., Hansen, J., Blue, B., Williams, R., Carver, R., and Frank, A., "Laboratory experiments, numerical simulations, and astronomical observations of deflected supersonic jets: Application to HH 110," *The Astrophysical Journal*, Vol. 705, No. 1, 2009, pp. 1073.

[27] Li, C., Tzeferacos, P., Lamb, D., Gregori, G., Norreys, P., Rosenberg, M., Follett, R., Froula, D., Koenig, M., Seguin, F., et al., "Scaled laboratory experiments explain the kink behaviour of the Crab Nebula jet," *Nature communications*, Vol. 7, No. 1, 2016, pp. 1–8.

[28] Kuranz, C. C., Park, H.-S., Huntington, C. M., Miles, A. R., Remington, B. A., Plewa, T., Trantham, M., Robey, H., Shvarts, D., Shimony, A., et al., "How high energy fluxes may affect Rayleigh–Taylor instability growth in young supernova remnants," *Nature communications*, Vol. 9, No. 1, 2018, pp. 1–6.

[29] Tzeferacos, P., Rigby, A., Bott, A., Bell, A., Bingham, R., Casner, A., Cattaneo, F., Churazov, E., Emig, J., Flocke, N., et al., "Numerical modeling of laser-driven experiments aiming to demonstrate magnetic field amplification via turbulent dynamo," *Physics of Plasmas*, Vol. 24, No. 4, 2017, pp. 041404.

[30] Bailey, J. E., Nagayama, T., Loisel, G. P., Rochau, G. A., Blancard, C., Colgan, J., Cosse, P., Faussurier, G., Fontes, C., Gilleron, F., et al., "A higher-than-predicted measurement of iron opacity at solar interior temperatures," *Nature*, Vol. 517, No. 7532, 2015, pp. 56–59.

[31] Millot, M., Coppari, F., Rygg, J. R., Correa Barrios, A., Hamel, S., Swift, D. C., and Eggert, J. H., "Nanosecond X-ray diffraction of shock-compressed superionic water ice," *Nature*, Vol. 569, No. 7755, 2019, pp. 251–255.

[32] Rybicki, G. B. and Lightman, A. P., *Radiative processes in astrophysics*, John Wiley & Sons, 1991.

[33] Mihalas, D. and Mihalas, B. W., *Foundations of radiation hydrodynamics*, Courier Corporation, 2013.

[34] Marshak, R., "Effect of radiation on shock wave behavior," *The Physics of Fluids*, Vol. 1, No. 1, 1958, pp. 24–29.

[35] Massen, J., Tsakiris, G., Eidmann, K., Földes, I., Löwer, T., Sigel, R., Witkowski, S., Nishimura, H., Endo, T., Shiraga, H., et al., "Supersonic radiative heat waves in low-density high-Z material," *Physical Review E*, Vol. 50, No. 6, 1994, pp. 5130.

[36] Back, C., Bauer, J., Landen, O., Turner, R., Lasinski, B., Hammer, J., Rosen, M., Suter, L., and Hsing, W., "Detailed measurements of a diffusive supersonic wave in a radiatively heated foam," *Physical review letters*, Vol. 84, No. 2, 2000, pp. 274.

[37] Back, C., Bauer, J., Hammer, J., Lasinski, B., Turner, R., Rambo, P., Landen, O., Suter, L., Rosen, M., and Hsing, W., "Diffusive, supersonic x-ray transport in radiatively heated foam cylinders," *Physics of plasmas*, Vol. 7, No. 5, 2000, pp. 2126–2134.

[38] Lan, K., Feng, T., Lai, D., Xu, Y., and Meng, X., "Study on two-dimensional transfer of radiative heating wave," *Laser and Particle Beams*, Vol. 23, No. 3, 2005, pp. 275–282.

[39] Shaoen, J., Yan, X., Yongkun, D., Dongxian, L., Zhijian, Z., Yixiang, H., Jinghong, L., Kexu, S., Xin, H., Wenhai, Z., et al., "Supersonic propagation of heat waves in low density heavy material," *Plasma Science and Technology*, Vol. 7, No. 4, 2005, pp. 2965.

[40] Xu, Y., Jiang, S., Lai, D., Pei, W., Ding, Y., Chang, T., Lan, K., Li, S., and Feng, T., "Two-photon group radiation transfer study in low-density foam cylinder," *Laser and Particle Beams*, Vol. 24, No. 4, 2006, pp. 495–501.

[41] Ji-Yan, Z., Jia-Min, Y., Shao-En, J., Yong-Sheng, L., Guo-Hong, Y., Yao-Nan, D., Yi-Xiang, H., and Xin, H., "Experimental observation of ionization and shock fronts in foam targets driven by thermal radiation," *Chinese Physics B*, Vol. 19, No. 2, 2010, pp. 025201.

[42] Rosen, P., Foster, J., Taylor, M., Keiter, P., Smith, C., Finke, J., Gunderson, M., and Perry, T., "Experiments to study radiation transport in clumpy media," *High Energy Density Laboratory Astrophysics*, Springer, 2006, pp. 213–217.

[43] Keiter, P., Gunderson, M., Foster, J., Rosen, P., Comley, A., Taylor, M., and Perry, T., "Radiation transport in inhomogeneous media," *Physics of Plasmas*, Vol. 15, No. 5, 2008, pp. 056901.

[44] Moore, A. S., Guymer, T. M., Morton, J., Williams, B., Kline, J. L., Bazin, N., Bentley, C., Allan, S., Brent, K., Comley, A. J., et al., "Characterization of supersonic radiation diffusion waves," *Journal of Quantitative Spectroscopy and Radiative Transfer*, Vol. 159, 2015, pp. 19–28.

[45] Guymer, T., Moore, A., Morton, J., Kline, J., Allan, S., Bazin, N., Benstead, J., Bentley, C., Comley, A., Cowan, J., et al., "Quantifying equation-of-state and opacity errors using integrated supersonic diffusive radiation flow experiments on the National Ignition Facility," *Physics of Plasmas*, Vol. 22, No. 4, 2015, pp. 043303.

[46] Fryer, C., Dodd, E., Even, W., Fontes, C., Greeff, C., Hungerford, A., Kline, J., Mussack, K., Tregillis, I., Workman, J., et al., "Uncertainties in radiation flow experiments," *High energy density physics*, Vol. 18, 2016, pp. 45–54.

[47] Coffing, S. X., Fryer, C. L., Robey, H. F., Fontes, C. J., Wood, S. R., Kozlowski, P. M., Johns, H. M., Meyerhofer, D., Byvank, T., Liao, A., et al., "Inferring the temperature profile of the radiative shock in the COAX experiment with shock radiography, Dante, and spectral temperature diagnostics," *Physics of Plasmas*, Vol. 29, No. 8, 2022, pp. 083302.

[48] Cohen, A. P., Malamud, G., and Heizler, S. I., "Key to understanding supersonic radiative Marshak waves using simple models and advanced simulations," *Physical Review Research*, Vol. 2, No. 2, 2020, pp. 023007.

[49] Drake, R. P., "Radiative shocks in astrophysics and the laboratory," *High Energy Density Laboratory Astrophysics*, Springer, 2005, pp. 49–59.

[50] Wan, W., Malamud, G., Shimony, A., Di Stefano, C., Trantham, M., Klein, S., Shvarts, D., Kuranz, C., and Drake, R., "Observation of single-mode, Kelvin-Helmholtz instability in a supersonic flow," *Physical review letters*, Vol. 115, No. 14, 2015, pp. 145001.

[51] Van der Holst, B., Tóth, G., Sokolov, I. V., Powell, K. G., Holloway, J. P., Myra, E., Stout, Q., Adams, M., Morel, J., Karni, S., et al., "CRASH: A block-adaptive-mesh code for radiative shock hydrodynamics—implementation and verification," *The Astrophysical Journal Supplement Series*, Vol. 194, No. 2, 2011, pp. 23.

[52] Fryxell, B., Olson, K., Ricker, P., Timmes, F., Zingale, M., Lamb, D., MacNeice, P., Rosner, R., Truran, J., and Tufo, H., "FLASH: An adaptive mesh hydrodynamics code for modeling astrophysical thermonuclear flashes," *The Astrophysical Journal Supplement Series*, Vol. 131, No. 1, 2000, pp. 273.

[53] Gittings, M., Weaver, R., Clover, M., Betlach, T., Byrne, N., Coker, R., Dendy, E., Hueckstaedt, R., New, K., Oakes, W. R., et al., "The RAGE radiation-hydrodynamic code," *Computational Science & Discovery*, Vol. 1, No. 1, 2008, pp. 015005.

[54] Kamm, J. R. and Timmes, F., "On efficient generation of numerically robust Sedov solutions," Tech. rep., Technical Report LA-UR-07-2849, Los Alamos National Laboratory, 2007.

[55] Chen, F. F. et al., *Introduction to plasma physics and controlled fusion*, Vol. 1, Springer, 1984.

[56] Lyon, S. P., "Sesame: the Los Alamos National Laboratory equation of state database," *Los Alamos National Laboratory report LA-UR-92-3407*, 1992.

[57] Toro, E. F., *Riemann solvers and numerical methods for fluid dynamics: a practical introduction*, Springer Science & Business Media, 2013.

[58] Castor, J. I., *Radiation hydrodynamics*, 2004.

[59] Zingale, M., "Introduction to Computational Astrophysical Hydrodynamics," 2017.

[60] Godunov, S. K. and Bohachevsky, I., "Finite difference method for numerical computation of discontinuous solutions of the equations of fluid dynamics," *Matematičeskij sbornik*, Vol. 47, No. 3, 1959, pp. 271–306.

[61] Roe, P. L., "Approximate Riemann solvers, parameter vectors, and difference schemes," *Journal of computational physics*, Vol. 43, No. 2, 1981, pp. 357–372.

[62] Harten, A., Lax, P. D., and Leer, B. v., "On upstream differencing and Godunov-type schemes for hyperbolic conservation laws," *SIAM review*, Vol. 25, No. 1, 1983, pp. 35–61.

[63] Sedov, L. I. and Volkovets, A., *Similarity and dimensional methods in mechanics*, CRC press, 2018.

[64] Fryer, C. L., Fontes, C. J., Warsa, J. S., Roming, P. W., Coffing, S. X., and Wood, S. R., "The Role of Inhomogeneities in Supernova Shock Breakout Emission," *The Astrophysical Journal*, Vol. 898, No. 2, 2020, pp. 123.

[65] Chandrasekhar, S., "Hydrodynamic and hydromagnetic stability, 652 pp., clarendon," 1961.

[66] Kundu, P. K., Cohen, I. M., and Dowling, D. R., *Fluid mechanics*, Academic press, 2015.

[67] Malamud, G., Shimony, A., Wan, W., Di Stefano, C., Elbaz, Y., Kuranz, C., Keiter, P., Drake, R., and Shvarts, D., "A design of a two-dimensional, supersonic KH experiment on OMEGA-EP," *High Energy Density Physics*, Vol. 9, No. 4, 2013, pp. 672–686.

[68] Chandrasekhar, S., *Radiative transfer*, Courier Corporation, 2013.

[69] Buglia, J. J., "Introduction to the theory of atmospheric radiative transfer," Tech. rep., 1986.

[70] Colgan, J., Kilcrease, D. P., Magee, N., Sherrill, M. E., Abdallah Jr, J., Hakel, P., Fontes, C. J., Guzik, J. A., and Mussack, K., "A new generation of Los Alamos opacity tables," *The Astrophysical Journal*, Vol. 817, No. 2, 2016, pp. 116.

[71] Grevesse, N. and Sauval, A., "Standard solar composition," *Space Science Reviews*, Vol. 85, No. 1, 1998, pp. 161–174.

[72] Carroll, B. W. and Ostlie, D. A., *An introduction to modern astrophysics*, Cambridge University Press, 2017.

[73] Mihalas, D., "Stellar atmospheres," *San Francisco: WH Freeman*, 1978.

[74] Levermore, C. and Pomraning, G., "A flux-limited diffusion theory," *The Astrophysical Journal*, Vol. 248, 1981, pp. 321–334.

[75] Graziani, F., *Computational methods in transport: verification and validation*, Vol. 62, Springer, 2008.

[76] Hurricane, O. and Hammer, J., "Bent marshak waves," *Physics of plasmas*, Vol. 13, No. 11, 2006, pp. 113303.

[77] Shussman, T. and Heizler, S. I., "Full self-similar solutions of the subsonic radiative heat equations," *Physics of Plasmas*, Vol. 22, No. 8, 2015, pp. 082109.

[78] Frey, L. H., Even, W., Whalen, D. J., Fryer, C. L., Hungerford, A. L., Fontes, C. J., and Colgan, J., "The Los Alamos supernova light-curve project: computational methods," *The Astrophysical Journal Supplement Series*, Vol. 204, No. 2, 2013, pp. 16.

[79] Silk, J., "On the Fragmentation of Cosmic Gas Clouds. I - The Formation of Galaxies and the First Generation of Stars," *Astrophys. J.*, Vol. 211, 1977, pp. 638–648.

[80] Rees, M. J. and Ostriker, J. P., "Cooling, Dynamics and Fragmentation of Massive Gas Clouds - Clues to the Masses and Radii of Galaxies and Clusters," *Mon. Not. R. Astron. Soc.*, Vol. 179, June 1977, pp. 541–559.

[81] White, S. D. M. and Rees, M. J., "Core condensation in heavy halos: a two-stage theory for galaxy formation and clustering," *Monthly Notices of the Royal Astronomical Society*, Vol. 183, No. 3, jul 1978, pp. 341–358.

[82] Birnboim, Y. and Dekel, A., "Virial shocks in galactic haloes?" *Monthly Notices of the Royal Astronomical Society*, Vol. 345, No. 1, oct 2003, pp. 349–364.

[83] Baldry, I. K., Glazebrook, K., Brinkmann, J., Ivezí c, Ž., Lupton, R. H., Nichol, R. C., and Szalay, A. S., "Quantifying the Bimodal Color-Magnitude Distribution of Galaxies," *Astrophys. J.*, Vol. 600, Jan. 2004, pp. 681–694.

[84] Cattaneo, A., Dekel, A., Devriendt, J., Guiderdoni, B., and Blaizot, J., "Modelling the Galaxy Bimodality: Shutdown above a Critical Halo Mass," *mnras*, Vol. 370, Aug. 2006, pp. 1651–1665.

[85] Zel'dovich, Y. B., "Gravitational Instability: An Approximate Theory for Large Density Perturbations." *Astron. Astrophys.*, Vol. 500, March 1970, pp. 13.

[86] Kereš, D., Katz, N., Weinberg, D. H., and Davé, R., "How do galaxies get their gas?" *Monthly Notices of the Royal Astronomical Society*, Vol. 363, No. 1, 2005, pp. 2–28.

[87] Springel, V., White, S. D., Jenkins, A., Frenk, C. S., Yoshida, N., Gao, L., Navarro, J., Thacker, R., Croton, D., Helly, J., Peacock, J. A., Cole, S., Thomas, P., Couchman, H., Evrard, A., Colberg, J., and Pearce, F., "Simulations of the formation, evolution and clustering of galaxies and quasars," *Nature*, Vol. 435, No. 7042, 2005, pp. 629–636.

[88] Dekel, A., Birnboim, Y., Engel, G., Freundlich, J., Goerdt, T., Mumcuoglu, M., Neistein, E., Pichon, C., Teyssier, R., and Zinger, E., "Cold streams in early massive hot haloes as the main mode of galaxy formation," *Nature*, Vol. 457, No. 7228, 2009, pp. 451–454.

[89] Bouché, N., Finley, H., Schroetter, I., Murphy, M. T., Richter, P., Bacon, R., Contini, T., Richard, J., Wendt, M., Kamann, S., Epinat, B., Cantalupo, S., Straka, L. A., Schaye, J., Martin, C. L., Péroux, C., Wisotzki, L., Soto, K., Lilly, S., Carollo, C. M., Brinchmann, J., and Kollatschny, W., "Possible Signatures of a Cold-flow Disk from MUSE Using a z? 1 Galaxy-Quasar Pair toward SDSS J1422-0001," *ApJ*, Vol. 820, No. 2, Apr 2016, pp. 121.

[90] Martin, D. C., O'Sullivan, D., Matuszewski, M., Hamden, E., Dekel, A., Lapiner, S., Morrissey, P., Neill, J. D., Cantalupo, S., Prochaska, J. X., et al., "Multi-filament gas inflows fuelling young star-forming galaxies," *Nature Astronomy*, 2019, pp. 1.

[91] Dekel, A. and Birnboim, Y., "Galaxy bimodality due to cold flows and shock heating," *Monthly Notices of the Royal Astronomical Society*, Vol. 368, No. 1, 2006, pp. 2–20.

[92] Birnboim, Y., Padnos, D., and Zinger, E., "the Hydrodynamic Stability of Gaseous Cosmic Filaments," *The Astrophysical Journal*, Vol. 832, No. 1, 2016, pp. L4.

[93] Goerdt, T. and Ceverino, D., "Inflow velocities of cold flows streaming into massive galaxies at high redshifts," *Monthly Notices of the Royal Astronomical Society*, Vol. 450, No. 4, jul 2015, pp. 3359–3370.

[94] Kereš, D. and Hernquist, L., "Seeding the Formation of Cold Gaseous Clouds in Milky Way-Size Halos," *Astrophys. J.*, Vol. 700, July 2009, pp. L1–L5.

[95] Ceverino, D., Dekel, A., and Bournaud, F., "High-redshift clumpy discs and bulges in cosmological simulations," *Monthly Notices of the Royal Astronomical Society*, Vol. 404, No. 4, mar 2010, pp. 2151–2169.

[96] Danovich, M., Dekel, A., Hahn, O., Ceverino, D., and Primack, J., "Four phases of angular-momentum buildup in high-z galaxies: from cosmic-web streams through an extended ring to disc and bulge," *Monthly Notices of the Royal Astronomical Society*, Vol. 449, No. 2, may 2015, pp. 2087–2111.

[97] Nelson, D., Vogelsberger, M., Genel, S., Sijacki, D., Kereš, D., Springel, V., and Hernquist, L., "Moving mesh cosmology: tracing cosmological gas accretion," *Monthly Notices of the Royal Astronomical Society*, Vol. 429, No. 4, mar 2013, pp. 3353–3370.

[98] Mandelker, N., Padnos, D., Dekel, A., Birnboim, Y., Burkert, A., Krumholz, M. R., and Steinberg, E., "Instability of supersonic cold streams feeding galaxies - I. Linear Kelvin-Helmholtz instability with body modes," *Monthly Notices of the Royal Astronomical Society*, Vol. 463, No. 4, 2016, pp. 3921–3947.

[99] Padnos, D., Mandelker, N., Birnboim, Y., Dekel, A., Krumholz, M. R., and Steinberg, E., "Instability of supersonic cold streams feeding galaxies-II. Non-linear evolution of surface and body modes of Kelvin-Helmholtz instability," *Monthly Notices of the Royal Astronomical Society*, Vol. 477, No. 3, 2018, pp. 3293–3328.

[100] Mandelker, N., Nagai, D., Aung, H., Dekel, A., Padnos, D., and Birnboim, Y., "Instability of supersonic cold streams feeding Galaxies ? III. Kelvin?Helmholtz instability in three dimensions," *Monthly Notices of the Royal Astronomical Society*, Vol. 484, No. 1, 01 2019, pp. 1100–1132.

[101] Cornuault, N., Lehnert, M. D., Boulanger, F., and Guillard, P., "Are Cosmological Gas Accretion Streams Multiphase and Turbulent?" *Astron. Astrophys.*, Vol. 610, March 2018, pp. A75.

[102] Malamud, G., Shimony, A., Wan, W. C., Di Stefano, C. A., Elbaz, Y., Kuranz, C. C., Keiter, P. A., Drake, R. P., and Shvarts, D., "A design of a two-dimensional, supersonic KH experiment on OMEGA-EP," *High Energy Density Physics*, Vol. 9, No. 4, 2013, pp. 672–686.

[103] Hammel, B., Kilkenny, J., Munro, D., Remington, B., Kornblum, H., Perry, T., Phillion, D., and Wallace, R., "X-ray radiographic imaging of hydrodynamic phenomena in radiation-driven materials—Shock propagation, material compression, and shear flow," *Physics of plasmas*, Vol. 1, No. 5, 1994, pp. 1662–1668.

[104] Harding, E. C., Hansen, J. F., Hurricane, O. A., Drake, R. P., Robey, H. F., Kuranz, C. C., Remington, B. A., Bono, M. J., Grosskopf, M. J., and Gillespie, R. S., "Observation of a Kelvin-Helmholtz Instability in a High-Energy-Density Plasma on the Omega Laser," *Physical Review Letters*, Vol. 103, No. 4, July 2009, pp. 045005.

[105] Hurricane, O., "Design for a high energy density Kelvin–Helmholtz experiment," *High Energy Density Physics*, Vol. 4, No. 3-4, 2008, pp. 97–102.

[106] Hurricane, O. A., Smalyuk, V. A., Raman, K., Schilling, O., Hansen, J. F., Langstaff, G., Martinez, D., Park, H.-S., Remington, B. A., Robey, H. F., Greenough, J. A., Wallace, R., Di Stefano, C. A., Drake, R. P., Marion, D., Krauland, C. M., and Kuranz, C. C., "Validation of a Turbulent Kelvin-Helmholtz Shear Layer Model Using a High-Energy-Density OMEGA Laser Experiment," *Physical Review Letters*, Vol. 109, No. 15, Oct. 2012, pp. 155004.

[107] Smalyuk, V. A., Hurricane, O. A., Hansen, J. F., Langstaff, G., Martinez, D., Park, H.-S., Raman, K., Remington, B. A., Robey, H. F., Schilling, O., Wallace, R., Elbaz, Y., Shimony, A., Shvarts, D., Di Stefano, C., Drake, R. P., Marion, D., Krauland, C. M., and Kuranz, C. C., "Measurements of turbulent mixing due to Kelvin-Helmholtz instability in high-energy-density plasmas," *High Energy Density Physics*, Vol. 9, March 2013, pp. 47–51.

[108] Rutter, E. M., Grosskopf, M. J., Malamud, G., Kuranz, C. C., Harding, E. C., Keiter, P. A., and Drake, R. P., "Comparison between Kelvin-Helmholtz instability experiments on OMEGA and simulation results using the CRASH code," *High Energy Density Physics*, Vol. 9, March 2013, pp. 148–151.

[109] MacFarlane, J., Golovkin, I., and Woodruff, P., "HELIOS-CR – A 1-D radiation-magnetohydrodynamics code with inline atomic kinetics modeling," *Journal of Quantitative Spectroscopy and Radiative Transfer*, Vol. 99, No. 1-3, may 2006, pp. 381–397.

[110] Choudhury, S. R., "Nonlinear Evolution of the Kelvin -Helmholtz Instability of Supersonic Tangential Velocity Discontinuities," *Journal of Mathematical Analysis and Applications*, Vol. 214, 1997, pp. 561–586.

[111] Dimotakis, P. E., "Two-dimensional shear-layer entrainment," *AIAA Journal*, Vol. 24, No. 11, 1986, pp. 1791–1796.

[112] Dimotakis, P. E., "The mixing transition in turbulent flows," *Journal of Fluid Mechanics*, Vol. 409, 2000, pp. 69–98.

[113] Sutherland, R. S. and Dopita, M. A., "Cooling functions for low-density astrophysical plasmas," *The Astrophysical Journal Supplement Series*, Vol. 88, sep 1993, pp. 253–327.

[114] Aung, H., Mandelker, N., Nagai, D., Dekel, A., and Birnboim, Y., "Kelvin-Helmholtz Instability in Self-Gravitating Streams," *arXiv preprint arXiv:1903.09666*, 2019.

[115] Berlok, T. and Pfrommer, C., "The impact of magnetic fields on cold streams feeding galaxies," *arXiv preprint arXiv:1904.02167*, 2019.

[116] Afshar-Rad, T., Desselberger, M., Dunne, M., Edwards, J., Foster, J., Hoarty, D., Jones, M., Rose, S., Rosen, P., Taylor, R., et al., "Supersonic propagation of an ionization front in low density foam targets driven by thermal radiation," *Physical review letters*, Vol. 73, No. 1, 1994, pp. 74.

[117] Hoarty, D., Willi, O., Barringer, L., Vickers, C., Watt, R., and Nazarov, W., "Observation of ionization fronts in low density foam targets," *Physics of Plasmas*, Vol. 6, No. 5, 1999, pp. 2171–2177.

[118] Boehly, T., Brown, D., Craxton, R., Keck, R., Knauer, J., Kelly, J., Kessler, T., Kumpan, S., Loucks, S., Letzring, S., et al., "Initial performance results of the OMEGA laser system," *Optics communications*, Vol. 133, No. 1-6, 1997, pp. 495–506.

[119] Campbell, K., Weber, F., Dewald, E., Glenzer, S., Landen, O., Turner, R., and Waide, P., "Omega Dante soft x-ray power diagnostic component calibration at the National Synchrotron Light Source," *Review of scientific instruments*, Vol. 75, No. 10, 2004, pp. 3768–3771.

[120] Sorce, C., Schein, J., Weber, F., Widmann, K., Campbell, K., Dewald, E., Turner, R., Landen, O., Jacoby, K., Torres, P., et al., "Soft X-ray power diagnostic improvements at the Omega Laser Facility," *Review of scientific instruments*, Vol. 77, No. 10, 2006, pp. 10E518.

[121] Fryer, C. L., Diaw, A., Fontes, C. J., Hungerford, A. L., Kline, J., Johns, H., Lanier, N., Wood, S., and Urbatsch, T., "Designing radiation transport tests: Simulation-driven uncertainty-quantification of the COAX temperature diagnostic," *High Energy Density Physics*, Vol. 35, 2020, pp. 100738.

[122] Haines, B. M., Sauppe, J. P., Keiter, P. A., Loomis, E. N., Morrow, T., Montgomery, D., Kuettner, L., Patterson, B. M., Quintana, T. E., Field, J., et al., "Constraining computational modeling of indirect drive double shell capsule implosions using experiments," *Physics of Plasmas*, Vol. 28, No. 3, 2021, pp. 032709.

[123] Hansen, J., Edwards, M., Froula, D., Gregori, G., Edens, A., and Ditmire, T., "Laboratory observation of secondary shock formation ahead of a strongly radiative blast wave," *Physics of plasmas*, Vol. 13, No. 2, 2006, pp. 022105.

[124] Cohen, A. P. and Heizler, S. I., "Modeling of supersonic radiative Marshak waves using simple models and advanced simulations," *Journal of Computational and Theoretical Transport*, Vol. 47, No. 4-6, 2018, pp. 378–399.

[125] Urbatsch, T. J. and Evans, T. M., "Milagro Version 2, An Implicit Monte Carlo Code for Thermal Radiative Transfer: Capabilities, Development, and Usage," Vol. Los Alamos National Laboratory report LA-14195-MS (osti.gov), 2005.

[126] Budge, K. G., "Physics of the Serrano Sn Transport Package," *LANL Technical report*, 2021.

[127] Fryer, C. L., Fontes, C. J., Warsa, J. S., Roming, P. W. A., Coffing, S. X., and Wood, S. R., "The Role of Inhomogeneities in Supernova Shock Breakout Emission," *ApJ*, Vol. 898, No. 2, Aug. 2020, pp. 123.

[128] Marozas, J., Marshall, F., Craxton, R., Igumenshchev, I., Skupsky, S., Bonino, M., Collins, T., Epstein, R., Glebov, V. Y., Jacobs-Perkins, D., et al., "Polar-direct-drive simulations and experiments," *Physics of plasmas*, Vol. 13, No. 5, 2006, pp. 056311.

[129] Marozas, J., Hohenberger, M., Rosenberg, M., Turnbull, D., Collins, T., Radha, P., McKenty, P., Zuegel, J., Marshall, F., Regan, S., et al., "First observation of cross-beam energy transfer mitigation for direct-drive inertial confinement fusion implosions using wavelength detuning at the National Ignition Facility," *Physical review letters*, Vol. 120, No. 8, 2018, pp. 085001.

[130] Urbatsch, T. J. and Evans, T. M., "Milagro version 2 an implicit Monte Carlo code for thermal radiative transfer: Capabilities, development, and usage," Tech. rep., Los Alamos National Lab.(LANL), Los Alamos, NM (United States), 2006.

[131] Fatenejad, M., Fryxell, B., Wohlbier, J., Myra, E., Lamb, D., Fryer, C., and Graziani, C., "Collaborative comparison of simulation codes for high-energy-density physics applications," *High Energy Density Physics*, Vol. 9, No. 1, 2013, pp. 63–66.

[132] Wollaber, A. B., Park, H., Lowrie, R. B., Rauenzahn, R. M., and Cleveland, M. A., "Radiation-hydrodynamics with a high-order, low-order method," Tech. rep., Los Alamos National Lab.(LANL), Los Alamos, NM (United States), 2015.

[133] Fontes, C. J., Colgan, J., and Abdallah, J., "Self-consistent large-scale collisional-radiative modeling," *Modern Methods in Collisional-Radiative Modeling of Plasmas*, Springer, 2016, pp. 17–50.

[134] Sherlock, M., Brodrick, J. P., and Ridgers, C. P., "A comparison of non-local electron transport models for laser-plasmas relevant to inertial confinement fusion," *Physics of Plasmas*, Vol. 24, No. 8, 2017, pp. 082706.

[135] Scott, H. and Harte, J., "Hohlraum Simulations with Tabulated Non-LTE Data," *APS Division of Plasma Physics Meeting Abstracts*, Vol. 2018, 2018, pp. JO4–008.

[136] Fryer, C. L., Wood, S., Coffing, S. X., Robey, H., Fontes, C. J., Johns, H., Kozlowski, P., Urbatsch, T., Lanier, N. E., Meyerhofer, D. D., et al., "Detailed temperature diagnostic studies for Radishock and COAX experiments," *High Energy Density Physics*, Vol. 46, 2023, pp. 101023.

[137] Hurricane, O., Glendinning, S. G., Remington, B. A., Drake, R. P., and Dannenberg, K., "Late-time hohlraum pressure dynamics in supernova remnant experiments," *Physics of Plasmas*, Vol. 8, No. 6, 2001, pp. 2609–2612.

[138] Canny, J., "A computational approach to edge detection," *IEEE Transactions on pattern analysis and machine intelligence*, , No. 6, 1986, pp. 679–698.

[139] Kozlowski, P. M., Kim, Y., Haines, B. M., Robey, H., Murphy, T. J., Johns, H. M., and Perry, T. S., "Use of computer vision for analysis of image datasets from high temperature plasma experiments," *Review of Scientific Instruments*, Vol. 92, No. 3, 2021, pp. 033532.

[140] Barnak, D., Davies, J., Knauer, J., and Kozlowski, P. M., "Soft x-ray spectrum unfold of K-edge filtered x-ray diode arrays using cubic splines," *Review of Scientific Instruments*, Vol. 91, No. 7, 2020, pp. 073102.

[141] Kowzlowski, P., "FIDUCIA," https://github.com/lanl/fiducia, 2020, accessed on 2021-11-01.

[142] Eilers, P. H. and Boelens, H. F., "Baseline correction with asymmetric least squares smoothing," *Leiden University Medical Centre Report*, Vol. 1, No. 1, 2005, pp. 5.

[143] Moore, A., Cooper, A., Schneider, M., MacLaren, S., Graham, P., Lu, K., Seugling, R., Satcher, J., Klingmann, J., Comley, A., et al., "Radiation transport and energetics of laser-driven half-hohlraums at the National Ignition Facility," *Physics of Plasmas*, Vol. 21, No. 6, 2014, pp. 063303.

[144] Remington, B. A., Drake, R. P., Takabe, H., and Arnett, D., "A review of astrophysics experiments on intense lasers," *Physics of Plasmas*, Vol. 7, No. 5, 2000, pp. 1641–1652.

[145] Strömgren, B., "The Physical State of Interstellar Hydrogen." *ApJ*, Vol. 89, May 1939, pp. 526.

[146] Abbott, D. C., *Radiatively-driven stellar winds*, Ph.D. thesis, University of Colorado, Boulder, Jan. 1977.

[147] Rybicki, G. B. and Lightman, A. P., "Book-Review - Radiative Processes in Astrophysics," *Astronomy Quarterly*, Vol. 3, Jan. 1979, pp. 199.

[148] McClarren, R. G., Drake, R. P., Morel, J., and Holloway, J. P., "Theory of radiative shocks in the mixed, optically thick-thin case," *Physics of Plasmas*, Vol. 17, No. 9, 2010, pp. 093301.

[149] Thompson, K. G., Wollaeger, R. T., and Budge, K. G., "Jayenne Physics Manual, Revision 1.0 - An Implicit Monte Carlo Code for Thermal Radiative Transfer," 2021.

[150] Haines, B. M., Keller, D., Long, K., McKay Jr, M., Medin, Z., Park, H., Rauenzahn, R., Scott, H., Anderson, K., Collins, T., et al., "The development of a high-resolution Eulerian radiation-hydrodynamics simulation capability for laser-driven Hohlraums," *Physics of Plasmas*, Vol. 29, No. 8, 2022, pp. 083901.

[151] Bentley, J. L., "Multidimensional binary search trees used for associative searching," *Communications of the ACM*, Vol. 18, No. 9, 1975, pp. 509–517.

[152] King, M. J., "Immiscible two-phase flow in a porous medium: Utilization of a Laplace transform boost," *Journal of Mathematical Physics*, Vol. 26, 1985, pp. 870.

[153] Doss, F. W., "Exact results on intrinsic gradients in the compression of heat," *Proceedings of the International Conference on Mathematics and Computational Methods Applied to Nuclear Science and Engineering*, ANS M&C 2021, 2021, p. 1134.

[154] Masser, T., Wohlbier, J., and Lowrie, R., "Shock wave structure for a fully ionized plasma," *Shock waves*, Vol. 21, No. 4, 2011, pp. 367–381.

[155] Lowrie, R. B. and Rauenzahn, R. M., "Radiative shock solutions in the equilibrium diffusion limit," *Shock waves*, Vol. 16, No. 6, 2007, pp. 445–453.